Doctor Thesis

Search for a Lepton Flavor Violating Muon Decay Mediated by a New Light Neutral Particle with the MEG Detector

by

Hiroaki Natori

Department of Physics, School of Science,
the Univeristy of Tokyo

Abstract

A discovery of a new particle, which mediates flavor violating decay of charged leptons, would unambiguously establish existence of new physics beyond the Standard Model (SM) of particle physics, because charged lepton flavor violation (cLFV) is extremely suppressed in the SM. A first dedicated search for a lepton flavor violating muon decay, $\mu^+ \to e^+\phi$, mediated by a new light neutral particle, ϕ, which decays into two photons, $\phi \to \gamma\gamma$, was performed by the MEG experiment. The new particle ϕ is expected to have a long lifetime and its decay into e^+e^- may possibly be strongly suppressed. Although the experiment is optimized to detect another cLFV decay, $\mu^+ \to e^+\gamma$, it also has a good sensitivity to the ϕ-mediated cLFV decay, $\mu^+ \to e^+\phi, \phi \to \gamma\gamma$. The liquid xenon photon detector has a capability of reconstructing multiple photon with precise measurements of their energies, positions and timings within its large acceptance. By analyzing the data taken in 2009 and 2010, which corresponds to 1.8×10^{14} muon decays in the target, no evidence was found for the ϕ-mediated decays. Upper bounds on the branching ratio were obtained for various mass values 10–45 MeV and lifetimes ≤ 10 ns. In particular, for the lower mass region M_ϕ, this result exceeds the bound set by the generic search for $\mu^+ \to e^+\gamma\gamma$ by the Crystal Box experiment, and thus established the most stringent limits on the ϕ-mediated cLFV decays.

Contents

Part I

Introduction

Chapter 1

Introduction

The aim of science is to understand and reveal the law of nature. With many experiments and theoretical investigations, physicists have constructed the Standard Model (SM) of elementary particle physics. It can describe the elementary particles and forces, the most fundamental components of the nature. The SM is a great success. Its predictions are so powerful that no experiment finds fatal flaws in it so far. Nevertheless, scientists do not believe that the SM is the ultimate goal we have been aiming at, because its many elements are determined arbitrarily without any theoretical justifications, just to fit the experimental observations.

Many extended models from the SM have been proposed, and experimental physicists are now trying to find a clue to physics beyond the SM. Finding deviations from the SM prediction is the key. Lepton flavor violation (LFV) of charged lepton (cLFV) is thought to be a clear deviation from the SM. In this thesis, we searched for a new light neutral particle, ϕ, which causes cLFV in the muon decay. ϕ is a light neutral particle, which is expected to have a large lifetime and to decay into two photons. Searching the decay mode, $\mu^+ \to e^+\phi, \phi \to \gamma\gamma$, was performed using data taken by the MEG experiment in 2009 and 2010, which corresponds to 1.8×10^{14} muon stop in the target.

The experiment is dedicated to the search for another cLFV decay, $\mu^+ \to e^+\gamma$. A huge number of muon decays with gamma-ray and positron signals are recorded in the experiment. As the MEG is designed to search for $\mu^+ \to e^+\gamma$ decays, it is not optimized to detect other decay modes. For example, we have very small efficiency for generic three body decays such as $\mu^+ \to e^+\gamma\gamma$, because the momentum of positron from this mode is expected to have a peak around 30 MeV which is out of the range of geometrical acceptance of the positron spectrometer, and the limited solid angle of the gamma-ray detector gives very small acceptance to detect both gamma-rays from generic $\mu^+ \to e^+\gamma\gamma$ decays.

However, we have good detection efficiency for $\mu^+ \to e^+\phi, \phi \to \gamma\gamma$ decay mode when the mass of ϕ is about a few tens of MeV. Positron momentum becomes approximately the same as that of $\mu^+ \to e^+\gamma$ decay when the mass of ϕ is small, which leads to good detection efficiency by the positron spectrometer. Small mass of ϕ makes generated ϕ to travel nearly with relativistic speed. It makes opening angle of two gamma-rays in the experimental frame to be small by the effect of Lorentz boost. This enables to detect both two gamma-rays within gamma-ray detector acceptance. It also makes the opening angle between the positron and the gamma-ray approximately back-to-back, which helps us to trigger $\mu^+ \to e^+\phi, \phi \to \gamma\gamma$ decay with the same trigger setting for $\mu^+ \to e^+\gamma$ search.

In the following sections, theoretical background of such a particle is discussed.

1.1 Theoretical background of light (pseudo-)scalar particle

There are well-motivated theoretical arguments that favor the existence of a very light scalar or pseudo-scalar particle, which remains undetected because it interacts very weakly with ordinary matter [1, 2].

It is known that when a global symmetry is spontaneously broken, a massless Nambu-Goldstone boson appears. But if the symmetry is not exact but only approximate, a massive state arises, which is naturally light [3]. A famous example is pions. They are relatively light compared to the other hadrons, because they are thought to be pseudo-Nambu-Goldstone bosons generated by spontaneous breakdown of approximate $SU(2)_L \times SU(2)_R$ chiral symmetry. In many extensions of the SM, the electroweak symmetry breaking sector includes additional weak doublets or singlets. New CP-even, CP-odd or charged scalar states may be present in the physical spectrum. If the theory possesses an approximate global symmetry, a CP-odd scalar may acquire light mass.

Examples of such light particles are axion [4], Familons [5], and Majorons [6], which are associated with spontaneously broken Peccei-Quinn [7], family and lepton number symmetries, respectively. Another candidate is a pseudoscalar boson "A" in the two-Higgs doublet model (THDM) which acquires a mass proportional to the small parameter: $m_A^2 = -\lambda_5 v^2$, with $v = 246$GeV the electroweak scale, and $\lambda_5 \to 0$ corresponds to exact global $U(1) \times U(1)$ symmetry. Phenomenology of "A" with mass below 200 MeV is described in Ref. [1, 2, 8, 9]. According to Ref. [9], the muon anomalous magnetic moment and other low energy processes give a tight constraint on the parameter space of this class of models, but the existence of a very light scalar with a mass at the MeV level is still possible by fine-tuning the model parameters. According to Ref. [10], a light pseudoscalar is allowed also in the minimal composite Higgs model. In the framework of the next-to-minimal supersymmetric Standard Model (NMSSM), Ref. [11] shows a CP-odd Higgs should either be heavier than 210 MeV or have couplings to fermions 4 orders of magnitude below those of the SM.

A possible additional scalar that introduces cLFV at the tree level and its implications on the $l_i \to l_j \gamma\gamma$ and $l_i \to l_j e^+e^-$ transitions are investigated in Ref. [1], where l_i is a charged lepton of i-th generation. Suppose that a very light pseudoscalar boson ϕ mediate cLFV. When it is lighter than the muon, the only kinematically allowed tree-level decay mode is $\phi \to e^+e^-$, and a one-loop induced mode $\phi \to \gamma\gamma$ can also be competitive since the ϕ e^+e^- vertex is expected to be highly suppressed in general. Figure 1.1 shows the Feynman diagram for the muon decay through this particle, $\mu^+ \to e^+\phi, \phi \to \gamma\gamma$.

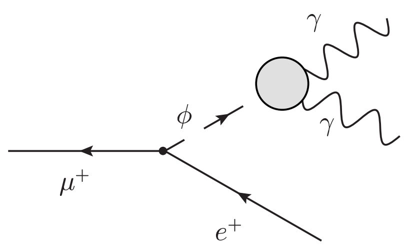

Figure 1.1: Feynman diagram for $\mu^+ \to e^+\phi, \phi \to \gamma\gamma$ decay. Large circle represents a fermion loop.

The decay width of ϕ is calculated in Ref. [1]. We assume that the couplings of ϕ to the leptons are naturally suppressed by introducing the Cheng-Sher ansatz [12] , and Yukawa coupling $\phi l_i l_j$ is written as:

$$\lambda_{ij} \frac{\sqrt{M_i M_j}}{v} \gamma_5 \tag{1.1}$$

where λ is a dimensionless nondiagonal matrix defined in the flavor space and γ_5 is the fifth gamma matrix [2]. The decay width into an electron pair is given by

$$\Gamma(\phi \to e^+ e^-) = \frac{\alpha |\lambda_{ee}|^2 M_\phi}{2 s_{2W}^2} \left(\frac{M_e}{M_Z}\right)^2 \left(1 - \frac{4M_e^2}{M_\phi^2}\right)^{\frac{3}{2}}, \tag{1.2}$$

with $s_{2W} = 2 \sin\theta_W \cos\theta_W$ and θ_W is the weak angle. The decay width for the two photon mode is given by

$$\Gamma(\phi \to \gamma\gamma) = \frac{\alpha^3 M_\phi}{16\pi^2 s_{2W}^2} \left(\frac{M_\phi}{M_Z}\right)^2 |F|^2, \tag{1.3}$$

with

$$F = \sum_{f=l,q} N_C^f Q_f^2 \lambda_{ff} x f(x), \tag{1.4}$$

and

$$f(x) = \begin{cases} \left(\arcsin \frac{1}{\sqrt{x}}\right)^2 & x \geq 1, \\ -\left(\text{arccosh} \frac{1}{\sqrt{x}} - \frac{i\pi}{x}\right)^2 & x < 1, \end{cases} \tag{1.5}$$

where $x = 4M_f^2/M_\phi^2$, N_C^f is the color index, and Q_f is the electric charge in units of the positron charge [13]. The result of numerical calculation of the decay width for the case that $\lambda_{ff} = 1$ is shown in Figure 1.2. We observe that Γ_ϕ is of the order of 10^{-14} GeV at most, and $\Gamma_\phi \ll M_\phi$ holds. This means that ϕ is a long-lived particle, and the narrow-width approximation can be used. The process in Figure 1.1 thus goes through on-shell ϕ. Branching ratio of $\mu^+ \to e^+\phi, \phi \to \gamma\gamma$ is then,

$$\begin{aligned} \mathcal{B}(\mu \to e\phi, \phi \to \gamma\gamma) &\simeq \mathcal{B}(\mu \to e\phi)\mathcal{B}(\phi \to \gamma\gamma) \\ &\simeq \frac{\alpha|\lambda_{\mu e}|^2}{4s_{2W}^2} \left(\frac{M_e}{\Gamma_\mu}\right) \left(\frac{M_\mu}{M_Z}\right)^2 (1 - y_\mu^2)^2 \cdot \mathcal{B}(\phi \to \gamma\gamma) \end{aligned} \tag{1.6}$$

with $y_\mu = M_\phi/M_\mu$. Because $\gamma\gamma$ mode is a loop effect, ee mode is usually more favored than $\gamma\gamma$ mode. But this does not hold if λ_{ee} is strongly suppressed; it would only decay into $\gamma\gamma$ in this case.

Possibility to have a "leptophobic" pseudoscalar is discussed in Ref. [2]. The pattern of the pseudoscalar couplings to the SM fermions is quite model-dependent. One can employ simple discrete symmetries to construct three-doublet models in which two doublets couple to quarks while the third doublet couples to leptons and does not mix with the other doublets. In this case, the pseudoscalar in the first two-doublet sector is entirely leptophobic. The leptophobic pseudoscalar decays entirely into photon pairs and its lifetime generally becomes 2–3 times larger than the usual case. It is noted that off-diagonal leptonic couplings must exist for cLFV processes such as shown in Figure 1.1.

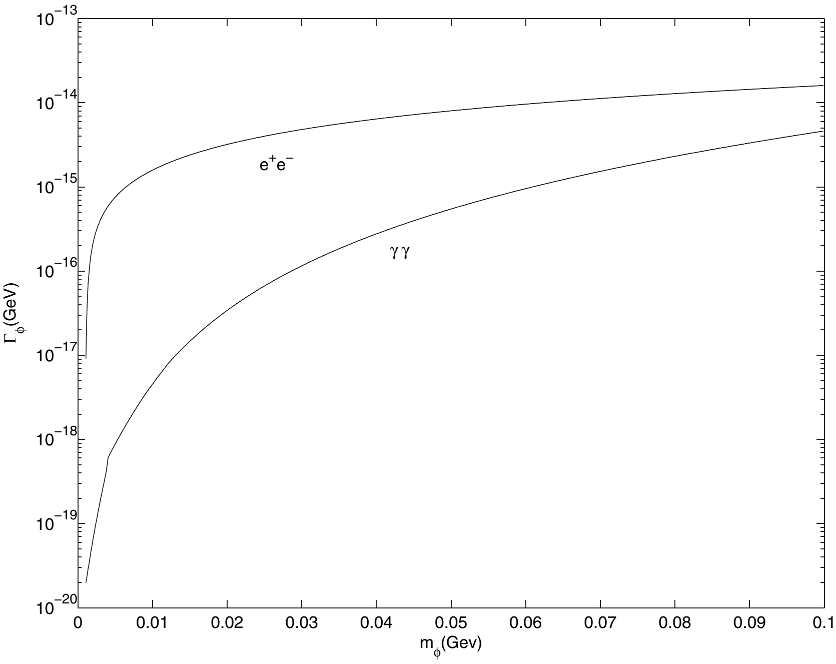

Figure 1.2: Decay widths for the modes $\phi \to ee$ and $\phi \to \gamma\gamma$ when $\lambda_{ff} = 1$ [1]

1.2 Muon decay experiments

1.2.1 Muon decay modes

Table 1.1: Decay modes and branching fraction of muon

Decay mode	Branching ratio
$\mu^+ \to e^+\nu_e\overline{\nu}_\mu$	$\sim 100\%$
$\mu^+ \to e^+\nu_e\overline{\nu}_\mu\gamma$	$(1.4 \pm 0.4)\ \times 10^{-2}$[14]
$\mu^+ \to e^+\nu_e\overline{\nu}_\mu e^+e^-$	$(3.4 \pm 0.4)\ \times 10^{-5}$[15]
Decay mode	Upper Limit (90% C.L.)
$\mu^- \to e^-\nu_e\overline{\nu}_\mu$	$< 1.2 \times 10^{-2}$[16]
$\mu^+ \to e^+\gamma$	$< 2.4 \times 10^{-12}$[17]
$\mu^+ \to e^+e^+e^-$	$< 1.0 \times 10^{-12}$[18]
$\mu^+ \to e^+\gamma\gamma$	$< 7.2 \times 10^{-11}$[19]
$\mu^+ \to e^+\gamma X^0$	$< 1.1 \times 10^{-9}$[19][1]
$\mu^+ \to e^+X^0$	$< 3 \times 10^{-4}$[20][2]
$\mu^+ \to e^+X^0$	$< 2.6 \times 10^{-6}$[21][3]
$\mu^+ \to e^+X^0, X^0 \to e^+e^-$	$< 1 \times 10^{-10}$[22][4]

Leptons are elementary fermions that do not interact strongly. There are three types of charged leptons with different masses, electron, muon, and tau, and the corresponding

[1] $m_{X^0} < 2m_e$

[2] Valid when m_{X^0} = 0-93.4, 98.1-103.5 MeV.

[3] Limit for neutral massless Goldstone boson

[4] Limits on the branching fraction depend on the mass and and lifetime of X_0. The quoted limits are valid when $\tau_{X_0} \sim< 3. \times 10^{-10}$s if the decays are kinematically allowed.

neutral leptons are electron-, muon-, and tau-neutrino. Decays of charged leptons (muons and taus) have been extensively studied, which contributed to the establishment of the SM. The results of the past experimental studies on the muon decay modes are summarized in Table 1.1.

Upper three decay modes conserve lepton flavor and finite branching ratios are experimentally determined, but the other modes are cLFV phenomena and are not discovered yet. Lower four modes include a exotic particle X_0 which induces cLFV and whose mass is smaller than that of muon. There is no upper bound on the branching ratio for the decay mode $\mu^+ \to e^+\phi, \phi \to \gamma\gamma$ because no experiment has been performed to search for this decay mode.

The upper limit of $\mu^+ \to e^+X^0, X^0 \to e^+e^-$ strongly constrains existence of (pseudo-)scalar that couples to e^+e^-. But as mentioned in Section 1.1, depending on the model, branching fraction into $\gamma\gamma$ can be much higher than that of ee mode. In particular for leptophobic pseudoscalars it does not pose any constraint on $\mu^+ \to e^+\phi, \phi \to \gamma\gamma$. The bound on $\mu^+ \to e^+\gamma\gamma$ set by the Crystal Box experiment [19], however, constrain some kinematics region of the ϕ-mediated cascade decay. This topic is discussed in more details in the next section.

1.2.2 Constraints on $\mu^+ \to e^+\phi, \phi \to \gamma\gamma$ by Crystal Box result

Crystal Box experiment [19] gives an upper limit of the branching ratio of generic $\mu^+ \to e^+\gamma\gamma$ decay as 7.2×10^{-11}. The final state is the same for both decay modes $\mu^+ \to e^+\gamma\gamma$ and $\mu^+ \to e^+\phi, \phi \to \gamma\gamma$, but their kinematics are different. The result of Crystal Box experiment can be converted to the upper limit of the branching ratio of $\mu^+ \to e^+\phi, \phi \to \gamma\gamma$ decay mode by multiplying the relative efficiency of the Crystal Box experiment for generic $\mu^+ \to e^+\gamma\gamma$ and for $\mu^+ \to e^+\phi, \phi \to \gamma\gamma$ mode,

$$B(\mu \to e\phi, \phi \to \gamma\gamma) = B(\mu \to e\gamma\gamma) \times \frac{\epsilon_{\mu\to e\gamma\gamma}}{\epsilon_{\mu\to e\phi,\phi\to\gamma\gamma}}. \tag{1.7}$$

Figure 1.3 shows a schematic of the Crystal Box detector. Trajectories of positron were determined with the multilayer drift chamber. No magnetic field was applied. Energies of positron and gamma-ray were determined by 396 NaI(Tl) crystals. Crystals located at the four quadrants are stacked in 9 raws transverse to the beam axis, and in 10 columns along the beam axis. The size of the crystal is $2.5 \times 2.5 \times 12.0$ inch.

The relative efficiency was evaluated from the geometrical acceptance and the detection requirements of the Crystal Box experiment. The following criteria define the Crystal Box acceptance in this evaluation:

- $|z| < 10/2 \times 2.5$ inch when a particle reaches $|x| = 9/2 \times 2.5$ inch or $|y| = 9/2 \times 2.5$ inch,
- $E_\gamma > 20$ MeV for each gamma-ray,
- Reject events with two gamma-rays in the same quadrant,
- The (pseudo-)scalar ϕ decays before entering the crystal,
  - $|x_{\phi decay}| < 9/2 \times 2.5$ inch,

– $|y_{\phi decay}| < 9/2 \times 2.5$ inch,

where the z coordinate goes along the beam axis and y along vertical direction.

The result is shown in Figure 1.4. Note that this is just a rough and approximate evaluation and we did not try to simulate the detector performance. Estimation is performed using only true values of emission directions, vertex positions, and energies of particles. In the Crystal Box analysis, they also applied cuts for momentum conservation. If the lifetime of the (pseudo-)scalar ϕ is long, it travels long before it decays, thus the momentum conservation cuts could drop the event, lowering the efficiency. Therefore, the actual Crystal Box bounds would be worse than shown in Figure 1.4 for longer lifetime.

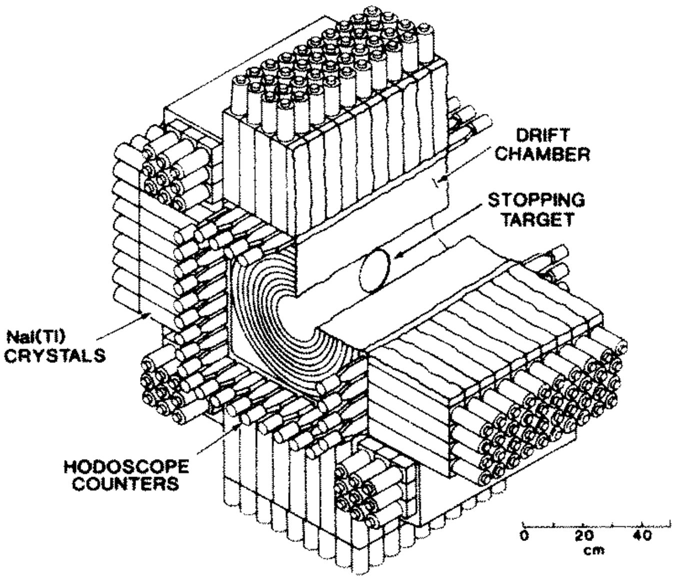

Figure 1.3: A schematic cutaway diagram of the Crystal Box detector [19]

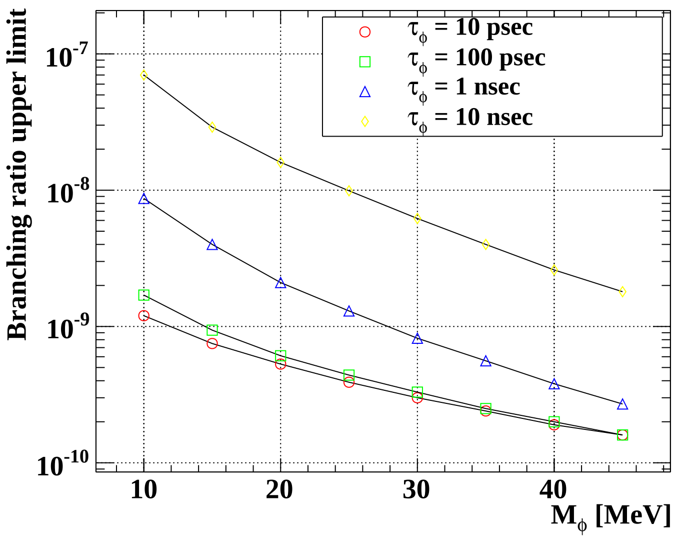

Figure 1.4: Crystal Box $\mu^+ \to e^+\gamma\gamma$ Branching ratio upper limit scaled to represent Branching ratio upper limit for $\mu^+ \to e^+\phi, \phi \to \gamma\gamma$ mode

1.3 Overview of this thesis

The theme of this thesis is searching for a new light neutral particle ϕ, which induces cLFV muon decay, $\mu \to e\phi$, and decays into photon pair, $\phi \to \gamma\gamma$, using the MEG data taken in 2009 and 2010. In the second Chapter, details about the MEG experiment and the MEG detectors are described. We describe event reconstruction and Monte Carlo event generation for $\mu^+ \to e^+\phi, \phi \to \gamma\gamma$ decay in Chapter 3. Chapter 4 describes detector performance and consistency between the experiment and Monte Carlo simulation. The analysis to search for the signal event is described in Chapter 6, and the conclusion is given in the last Chapter 6.

Part II

The MEG experiment

Chapter 2

Experimental installation

2.1 Detectors overview

The design of the MEG experiment is optimized to search for $\mu^+ \to e^+\gamma$. This is a clear two-body decay, and the event signature for a muon at rest is a positron and a γ-ray emitted back-to-back, coincident in time, and both with monochromatic energy of 52.8 MeV, which corresponds to approximately half the muon mass.

The key elements of the MEG experiment can be classified to the following three:

- Muon beam
- Positron spectrometer
- Gamma-ray detector

The experiment is performed at Paul Scherrer Institut (PSI) in Switzerland. The world's most intense positive DC muon beam is available in PSI. Transported muon is stopped at a thin target located at the center of a super conducting magnet called COBRA. a positron from a muon decay makes helical trajectory in the COBRA magnetic field and leaves hits in the drift chambers and reaches timing counters. Gamma rays are measured by a liquid Xenon (LXe) detector located outside of the COBRA. Geometrical acceptance of the positron spectrometer and the gamma-ray detector is $\Omega/4\pi \sim 0.1$ for the 52.8 MeV positron and gamma-ray. Schematic view of the detectors is shown in Figure 2.1.

2.1.1 MEG coordinate system

We define here the global and local coordinate system, which we use throughout this thesis.

The origin of the global coordinate system is at the center of the muon stopping target. The z-axis is in the same direction as the muon beam direction; the y-axis is vertical; and the x-axis is the remaining axis of right handed coordinate system. θ, and φ is the polar and azimuthal angle of spherical system with z-axis as polar axis and x-axis as azimuthal axis.

A special (u, v, w) coordinate system is used for the LXe detector. It is based on the inner face of the detector. The origin of (u, v, w) coordinate is (x, y, z) = (-67.85, 0, 0) [cm], which is the center of the inner face. Its definition is as follows:

$$R_{inner} = 67.85\,(\mathrm{cm}), \tag{2.1}$$
$$u = z, \tag{2.2}$$
$$v = R_{inner} \times \arctan(y/x), \tag{2.3}$$
$$w = \sqrt{x^2 + y^2} - R_{inner}. \tag{2.4}$$

The coordinate system is shown schematically together with the detector in Figure 2.1.

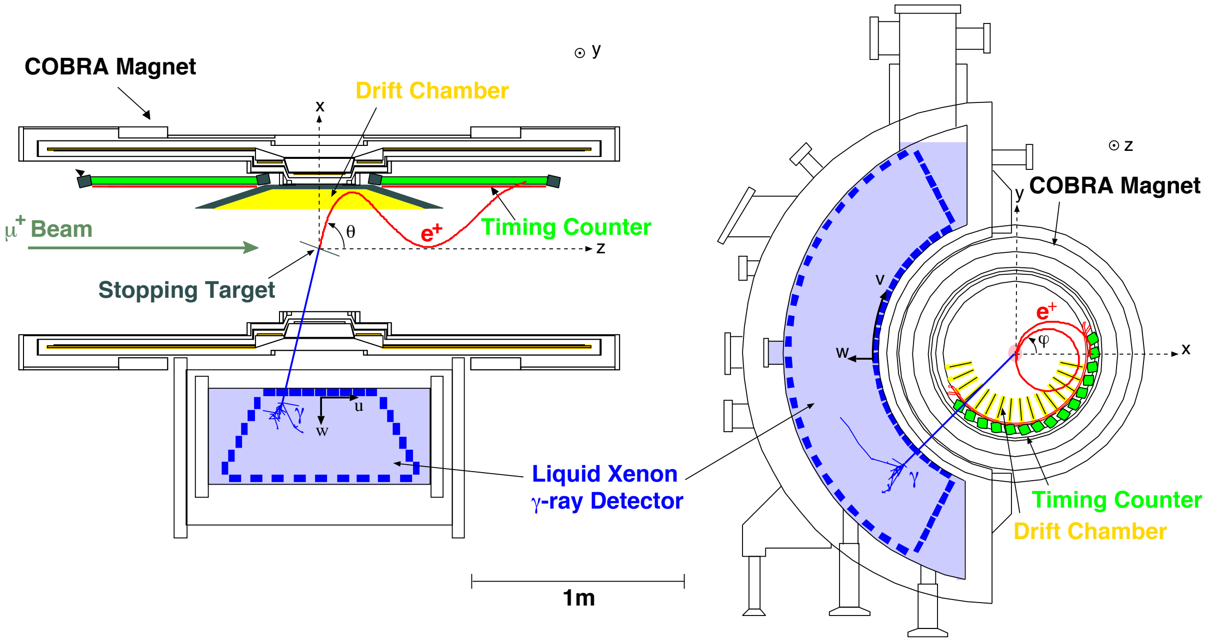

Figure 2.1: Schematic of the MEG detector and coordinate system

2.2 Beam

Requirement for the beam is

- High muon intensity,
- Low background.

To search for the rare muon decay, we need as many statistics as possible. In the same time, the instant intensity of the beam is preferred to be low, because the rate of the accidental background is positively correlated with it. So, a direct current (DC) muon beam is preferable to a pulsed beam.

MEG is conducted at the 590 MeV proton ring cyclotron facility of PSI in Switzerland, which provides the worlds most intense DC muon beam.

2.2.1 Proton ring cyclotron at PSI

The core of the PSI beam facility is 590 MeV proton ring cyclotron (Figure 2.2). The 870 keV proton beam from Cockcroft-Walton Pre-Injector (Figure 2.3(a)) is accelerated to 72 MeV by PSI Injector 2 cyclotron(Figure 2.3(b)) to feed into this ring cyclotron.

The accelerator delivers 2.0 or 2.2 mA protons, sometimes 1.8 mA, and it is planned to reach 2.6 mA in a few years, and 3.0 mA some years thereafter with some resonators' upgrade for the Injector 2 and cyclotron [23]. Characteristics of the 590 MeV proton ring cyclotron is summarized in Table 2.1.

Table 2.1: Characteristics of 590 MeV Proton Ring Cyclotron [24]

Characteristics	Value
Injection Energy	70-72 MeV
Extraction Energy	590 MeV
Extraction Momentum	1.2 GeV/c
Energy spread(FWHM)	ca. 0.2%
Beam Emittance	ca. 2π mm $\times$ mrad
Beam Current	2.2 mA DC
Accelerator Frequency	50.63 MHz
Time Between Pulses	19.75 ns
Bunch Width	ca. 0.3 ns
Extraction Losses	ca. 0.03 %
Mass of Sektormagnet	8 $\times$ 250.000 kg
Magneticfield (Stiffness T $\times$ m, middle)	0.9 T (4.0, 0.6 T)
Radius at injection	2100 mm
Radius at extraction	4460 mm
Mass of Resonator	4 $\times$ 25.000 kg

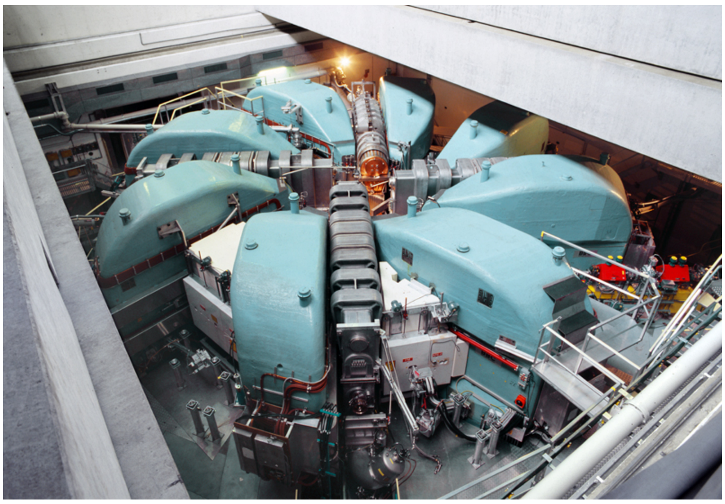

Figure 2.2: 590 MeV proton ring cyclotron at PSI

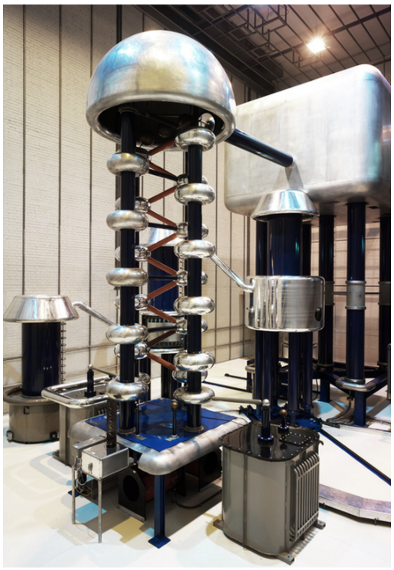

(a) 870keV Cockcroft-Walton Pre-Injector

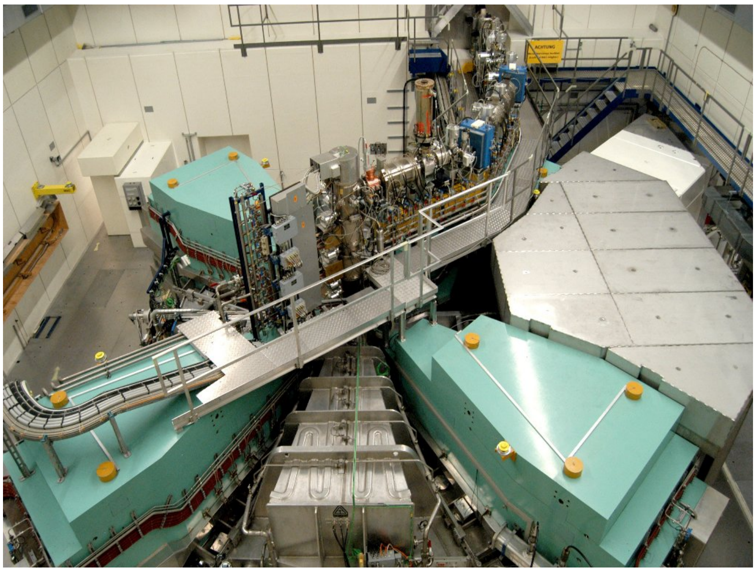

(b) 72 MeV Injector 2 cyclotron

Figure 2.3: Injection acceralators

2.2.2 πE5 beamline and surface muon beam

We use one of the secondary beamlines called πE5 (Figure 2.4) which provides low-energy (10 – 120 MeV/c) pions and muons as daughter particles of the pions at an angle of 175° with respect to the primary proton beam.

The production target (Target-E, Figure 2.5) is made of polycrystalline graphite. Its length along the proton beam direction is 40 mm, and it rotates to avoid overheat and to make the duration of replacement longer. The target cone is subdivided into 12 segments with gaps of 1 mm at an angle of 45° to the beam direction. This allows unconstrained dimensional changes of the irradiated part of the graphite. At the normal operating temperature, the gaps in the beam direction narrow down to about 0.5 mm.

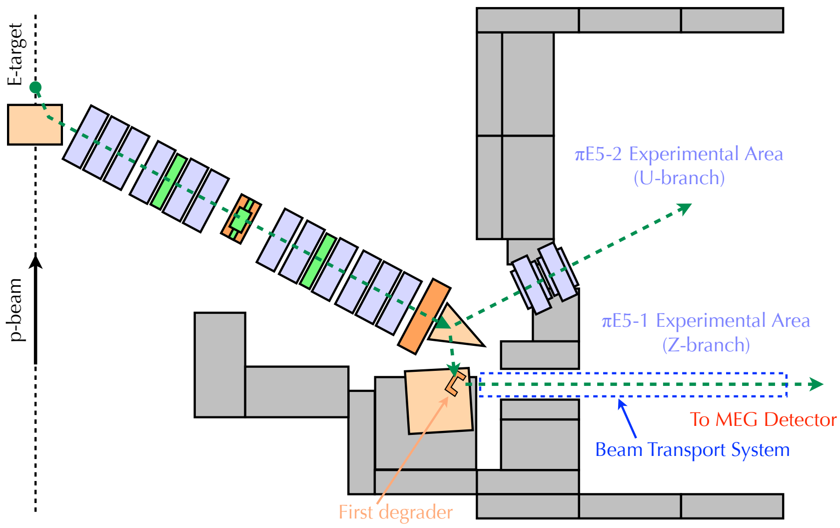

Figure 2.4: πE5 beamline

Figure 2.5: Target E

Charged pions produced inside the graphite target decays, $\pi^{\pm} \rightarrow \mu^{\pm}\nu_{\mu}$, with the lifetime about 26 ns, emitting polarized muons and neutrinos. This generates a quasi-continuous muon beam, by smearing the 19.75 ns cycle of the initial proton pulses. The momentum of muons from pion decay at rest is 29.8 MeV/c. Therefore, the muons from the pions stopped near the surface of the production target have a regulated momentum of approximately 29.8 MeV/c. This is called as surface muon [25]. Muon from a pion flying outside the target has higher momentum, and it is called as cloud muon. Figure 2.6 shows the pion and muon beam flux available at πE5 Beam line. Pion beam is used for calibration run. The intense surface muons are used for the $\mu^+ \rightarrow e^+\gamma$ search and also for calibration of detectors.

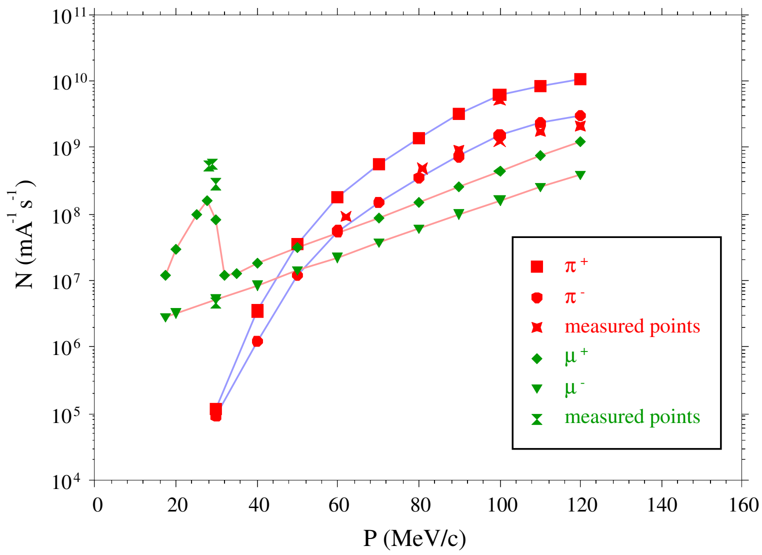

Figure 2.6: Pion and muon beam intensity at πE5 beamline

2.2.3 Beam transport system

The muon beam from the πE5 beam channel is transported to the stopping target through a beam transport system which is shown in Figure 2.7 schematically. It is composed of a quadrupole triplet (Triplet I), an electrostatic separator (Wien filter), a second quadrupole triplet (Triplet II), and a beam transport solenoid (BTS) with superconducting magnet.

In the original beam from the beam channel, the quantity of the positron contamination is eight times larger than that of positive muons. The Wien filter separates positron contamination spacially by 7.5 σ with its horizontal magnetic field of 133 Gauss and a vertical electric field of 195 kV. Triplet I, II refocus the beam after a bending magnet and the Wien filter. The BTS is used as a coupling element to the high magnetic field of the COBRA. A momentum degrader made of Mylar with a thickness of 200 or 300 μm is placed at the center of the BTS to increase stopping efficiency on the stopping target with less backgrounds. The beam spot size at the center of the target is $\sigma_x = 9.5$ mm and $\sigma_y = 10.2$ mm and the typical stopping rate was $3 \times 10^7 \mu^+ \mathrm{s}^{-1}$.

Note that we set the beam rate lower than the maximum capability of the channel ($\sim 1.5 \times 10^8$) by the limitation from the detector performance. From the beam point of view, there is a room for improvement.

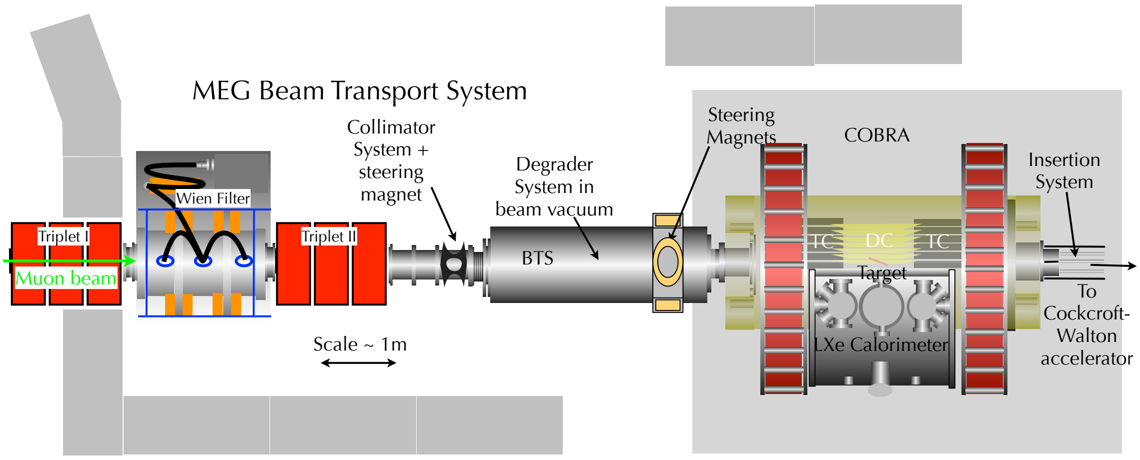

Figure 2.7: Schematic view of MEG beam transport system

2.2.4 Muon stopping target

The picture of the muon stopping target is shown in Figure 2.8. It is made of a sheet of polyethylene/polyester with a thickness of 205 μm (18 mg/cm^2). It has an ellipse shape with the length of 79.8 mm along the vertical axis and 200.5 mm for the major axis.

The target should be thick along the beam direction to increase the stopping efficiency and thin along the direction of the signal positron from the muon decay to minimize the scatter and the annihilation in flight (AIF) of positron. Slant angel is optimized to 20.5° relative to the beam axis. Stopping efficiency is estimated to be 82 % using MC simulation.

The target has six holes of 10 mm diameter, which is used to align the target and to estimate the resolution of the vertex position reconstruction. The support frame of the target is made of Rohacell whose density is 0.895 g/cm^3. It is filled with a mixture of helium gas and a few percent of air around the target to minimize scattering of positrons. The target can be removed from the center position to do the background study without target or the calibration runs using the different targets.

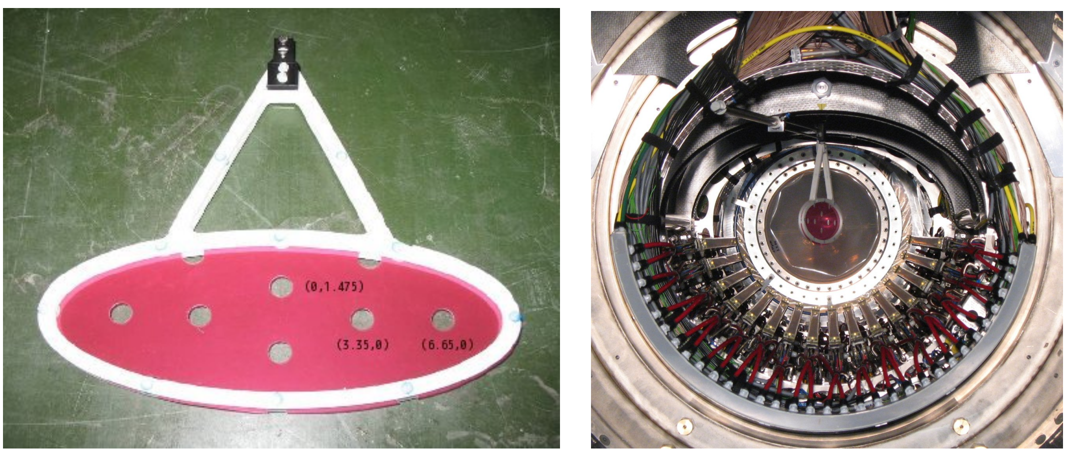

(a) Stopping target and hole position in cm

(b) Installed position viewed from downstream. 16 drift chamber modules are seen below the target.

Figure 2.8: Muon stopping target

2.3 Positron spectrometer

Positron spectrometer for the MEG experiment is designed to satisfy following requirements.

- Good momentum, direction and timing resolutions for the positrons with the energy around 50 MeV.
- Good performance under very high rate environment.
- Low material to suppress multiple scattering of positron and γ-ray background for the photon detector.

It is composed of a solenoidal magnet with graded magnetic field, 16 segmented drift chambers to track the positron trajectory to measure momentum, direction and time of flight of positron, and timing counter made of scintillation bars to measure the timing of positron hit.

2.3.1 COBRA magnet

We developed a thin-wall superconducting magnet with a gradient magnetic field for the positron spectrometer in the MEG experiment [26].

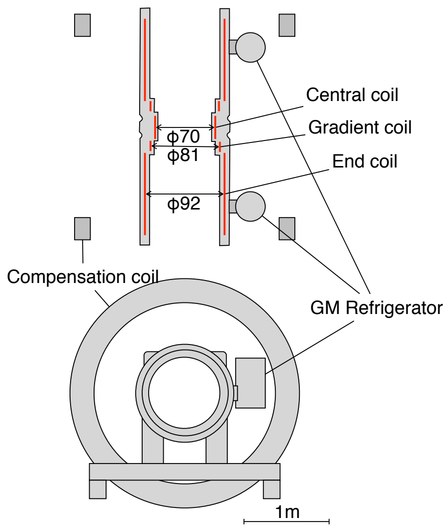

(a) Sectional drawings of the COBRA magnet

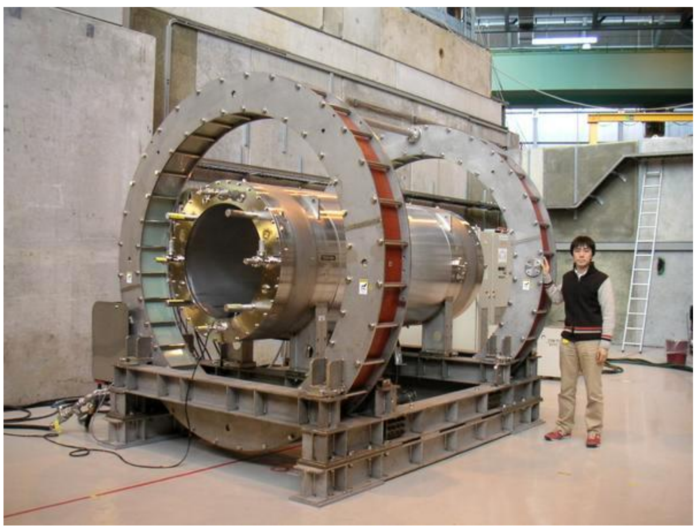

(b) Picture of the COBRA magnet

Figure 2.9: COBRA magnet

The main coil consists of five coils with three different radii as shown in the Figure 2.9(a). The gradient magnetic field produced by this step structure have two features. The first is much quicker sweep of positrons than in the conventional uniform solenoidal field as described schematically in the Figure 2.10(a, c), which allows a stable operation of the spectrometer in a high rate muon beam. The second is COnstant Bending RAdius (The name COBRA is named after this). As described in the Figure 2.10(b, d) tracks of positrons with the same momentum have the same radius and are independent of emission angles. Because of this feature, we do not loss efficiencies of the $\mu^+ \to e^+\gamma$ positron by not covering the small-radius region with the drift chambers. The profile of the magnetic field is shown in the Figure 2.11. In a normal operation at 360 A current, the central field is 1.27 T at z = 0, and 0.49 T at the edge.

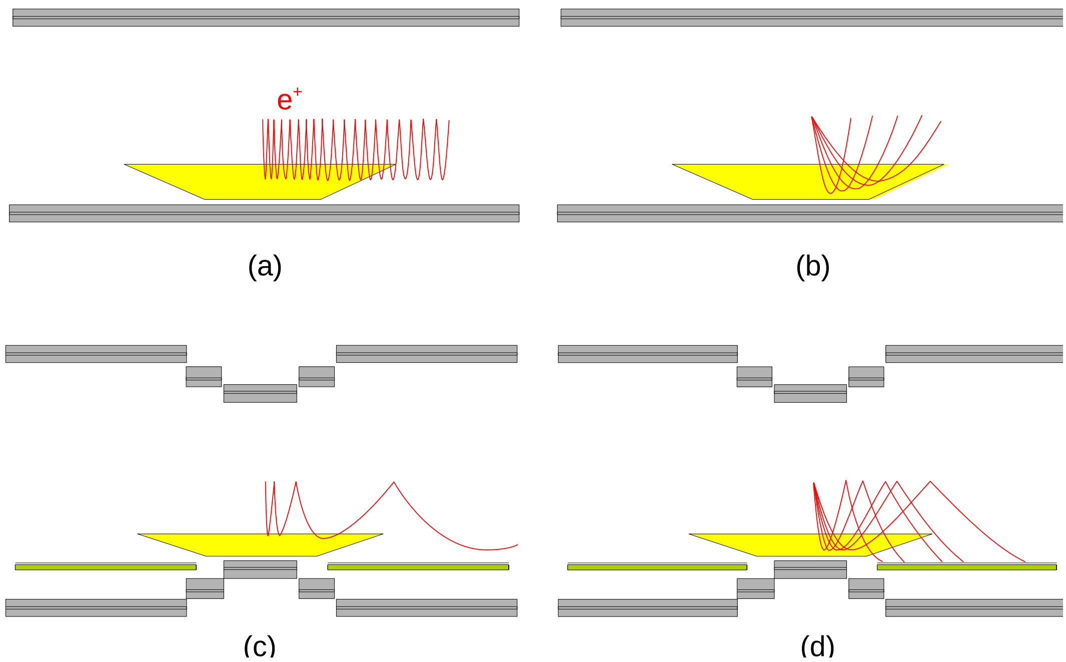

Figure 2.10: Positron trajectory in a uniform and the COBRA magnetic field

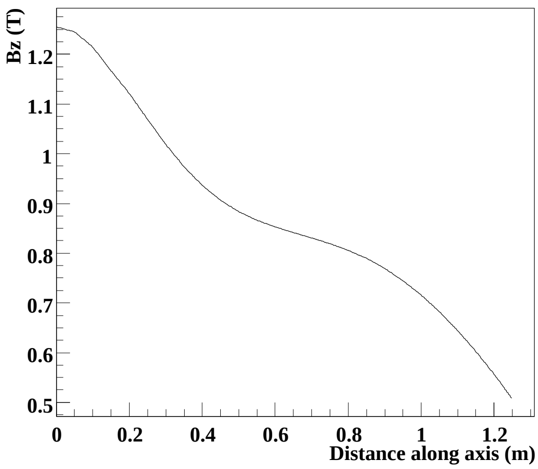

Figure 2.11: Profile of the magnetic field along the axis of the magnet

Gamma-ray from the muon decay passes through this magnet before entering the gamma-ray detector, so the magnet is desired to be thin. A high-strength conductor was developed so as to minimize the thickness of the coil between the target and photon detector. The superconducting cable is made from NbTi multifilament embedded in copper matrix with a 0.59 mm diameter and covered with high-strength aluminum stabilizer with a 0.8 × 1.1 mm^2 dimension, which is insulated with a Kapton plyimide [27]. Nickel of 5000 ppm is added into the aluminum stabilizer to reinforce it mechanically. The total thickness of the magnet including its cryostat is 0.197 X_0 and the transmission efficiency of gamma rays with the energy of 52.8 MeV is 85 %.

A pair of normal conducting compensation coils is implemented to cancel stray field around the photon detector which is placed close to the magnet. The Contour plot of the fringe field is shown in the Figure 2.12. The stray field is decreased with this compensation coil to be less than 50 Gauss , so that the PMT performance of the gamma-ray detector will not be worsened.

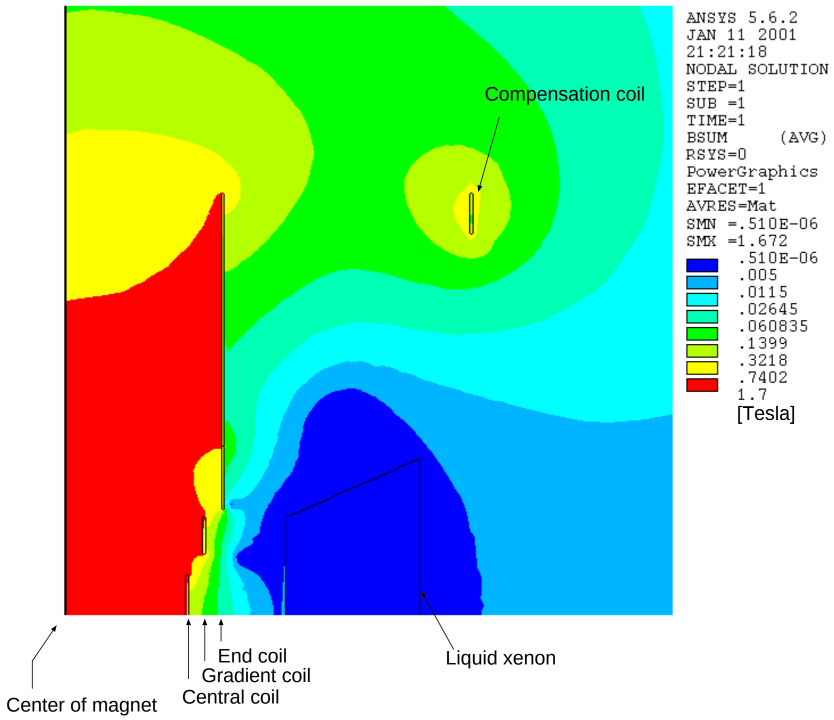

Figure 2.12: Contour map of fringe field around the gamma-ray detector

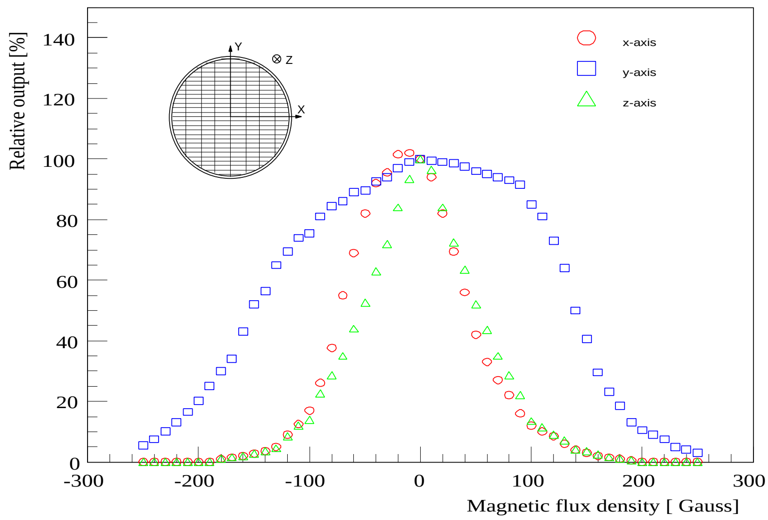

Figure 2.13: Responce of PMT used in the gamma-ray detector in magnetic field

2.3.2 Drift chamber

To suppress multiple scattering and annihilation in flight of positrons, we developed a very thin drift chamber system with approximately 2×10^{-3} X_0 in total along a positron trajectory.

Helical trajectories of positrons are measured with drift chambers, and the momentum, direction and time of flight of positron are reconstructed. It consists of 16 modules radially aligned with 10.5° intervals in φ direction. The radius from the beam axis which it covers is from 19.3 to 27.9 cm, and it measures only positrons with momentum larger than approximately 40 MeV. A picture of installed modules is shown in Figure 2.8(b).

Each module is composed of two layers, and each layer has nine drift cells; nine sense wires and ten potential wires (Figure 2.14(c)). The configuration of two types of wires is set inversely on each layer to resolve ambiguity along a radial direction. The two layers are separated by two inner cathode foils and enclosed by outer cathode foil. 3 mm gap between inner cathode foils is for cross talk suppression. They are supported by a carbon fiber frame with an open frame structure as illustrated in Figure 2.14(a) to decrease materials along positron path.

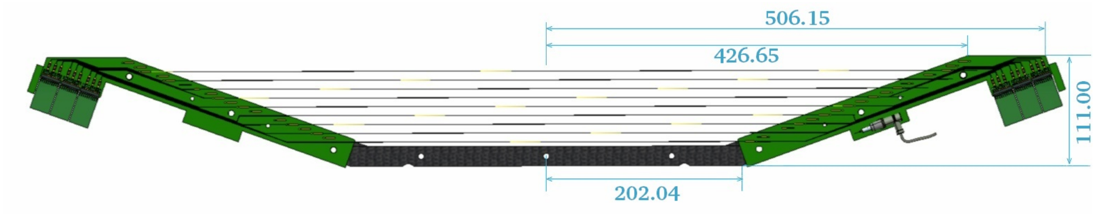

(a) Anode wire and Frame (unit: mm)

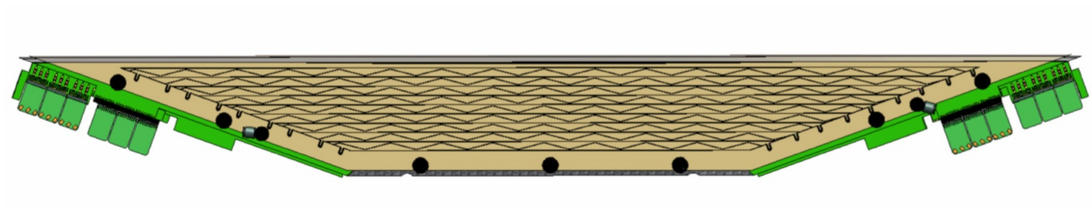

(b) A completed module

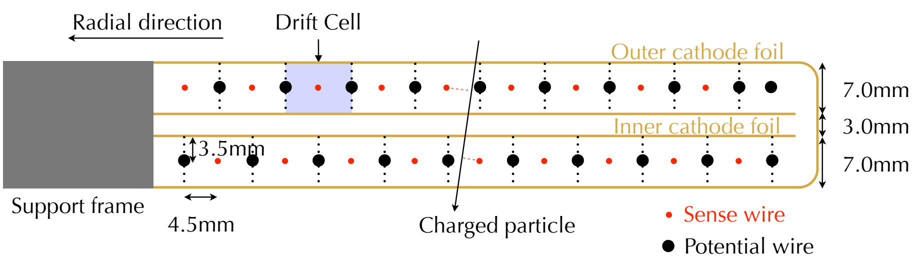

(c) Sectional drawing of drift chamber module

Figure 2.14: Schematics of a drift chamber module

The potential wires and cathode foils are grounded, and positive high voltage (∼1850 V) is applied to the sense wires. The sense wire and the potential wire are made of 25 μm diameter Ni/Cr (80:20) wire and 50 μm Be/Cu (2:98) wire respectively. Resistance of the sense wire is 2200 Ω/m. Cathode pads are made of thin 12.5 μm-thickness polyimide sheet with aluminum deposition. Because of the frame shape, drift chamber has only wires alined along z-axis and no crossing wires. To measure precise z position, cathode pads have 5 cm period zig-zag shape strip as shown in Figure 2.14(b). This is called vernier-pattern structure. A rough position is determined by signals at the both end of a sense wire, and a precise position by 2×2 cathode pad signals. A detailed explanation of vernier pad method is done in Section 3.5.1.

The active gas is He:C_2H_6 = 50:50. Outside of the module is flushed with a mixture of helium gas and a few percent of air. Pressure of the gas should be controlled better than 1 Pa to keep the shape of the chamber, and it is controlled within 0.005 Pa stability. Detailed description about the design, construction, and performance in 2007 engineering run are found in Ref. [28].

2.3.3 Timing counter

Timing counters (TIC) are installed at the both upstream and downstream side of the drift chamber system (Figure 2.1). TIC consists of two layers of plastic scintillators. The first layer is along z direction and detect hit time, rough z position and position in φ (TICP). The second layer is on the TICP along φ direction and detect z position (TICZ). They are inside a plastic bag flushed with nitrogen gas to protect PMTs of TICP from helium gas.

Figure 2.15 shows a picture and a design of TICP. It is made of 15 plastic scintillator bars ($4 \times 4 \times 80\,\mathrm{cm}^3$, Bicron BC-404 [29]) , each with 10.5° intervals in φ direction at a radius of 32 cm, and covers -150° $< \varphi <$ 10° in total. Only positrons with high momentum hit the bars. The scintillation bars are mounted with a slant angle at 20° to make the path lengths of positrons inside the bar uniform. Hexagonal shape of the bar is to avoid positron passing edge of these bars. 2-inch fine-mesh PMTs (R5294 by Hamamatsu Photonics [30]) are attached at the both sides of the bar with a slant angle at 10° with respect to the z-axis and $\sim$ 30° with respect to the magnetic field to recover their operation in a magnetic field.

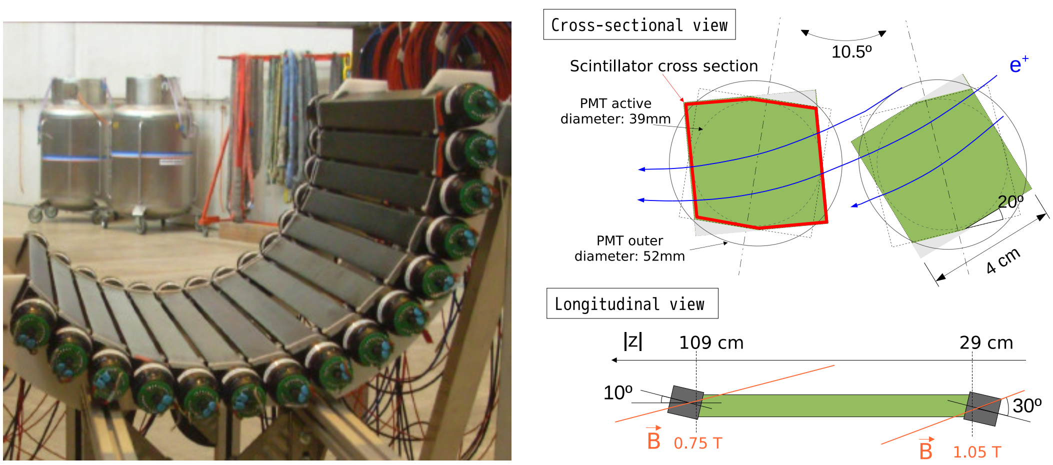

(a) (b)

Figure 2.15: Picture (a) and Design (b) of Timing φ-counter.

TICZ is mounted on the TICP as shown in Figure 2.16. It is made of bending 128 scintillating fibers ($6 \times 6\mathrm{mm}^2$ Saint-Goban BCF-20). Each fiber is separated optically at the center and read out independently at the both ends by a 5×5 mm^2 silicon avalanche photo-diode (APD) (Hamamatsu S8664-55). The z-counters are mounted on the -counters at a radius of 29 cm. The fiber is optically separated at a center. In the 2009, 2010 run TICZ was not used, because of some troubles with APDs. So, TICZ is not used in the analysis of this thesis.

Details of the design, construction, and performance in beam tests are described in Ref. [31, 32].

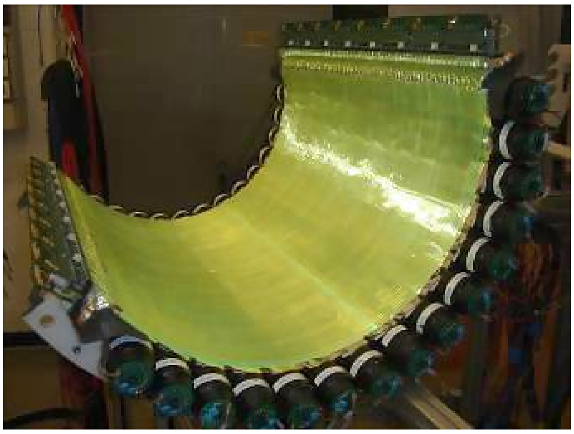

Figure 2.16: Exposed timing z counter mounted on timing φ bars.This picture is before light shielding.

2.4 Liquid xenon gamma-ray detector

For the $\mu^+ \to e^+\gamma$ search, gamma-ray detector is very important. We developed a novel detector using liquid Xenon (LXe) as a scintillator.

2.4.1 Property of liquid xenon

Property of LXe is summarized in Table 2.2. Liquid xenon has good property as scintillator as follows:

- Large light yield (80 % of NaI(Tl)),
- High density (2.95 g/cm^2), short radiation length $X_0 = 2.77$ cm,
- Fast decay time of scintillation light(45 ns for gamma-ray interaction),
- No self absorption of scintillation light,
- Uniform because it's liquid,
- Incident particle identification by decay time of scintillation light.

Large radiation length helps to detect gamma-ray efficiently. Large light yield (80 % of NaI(Tl)) and no self-absorption produce good energy resolution. Because it's liquid and has no self-absorption, we can construct a big and uniform detector whose response have small dependence to incident position. We can do purification of xenon to recover good response when it's needed. Fast decay time of scintillation light is helpful in high rate environment to minimize pile up events. It is also free from aging or damage by radiation.

Table 2.2: Properties of Liquid Xenon

Material Properties	Value & Unit
Atomic Number	54
Atomic Weight	131.293 [33]
Density at 161.4 K	2.978 g/cm^3 [34]
Boiling point	165.1 K [33]
Melting point	161.4 K [33]
Triple point	161.3 K 0.805 atm [35]
Radiation length	2.77 cm [33]
Critical Energy	14.5 MeV [36]
Mollier radius	4.2 cm [36]
Scinti. wavelength (peak $\pm$ FWHM)	(178 $\pm$ 14) nm [37]
Refractive index at 175 nm	1.57 to 1.72 [38, 39, 40]
W_{ph} for electron	21.6 eV [41]
W_{ph} for α particle	17.9 eV [41]
Decay time (recombination)	45 ns [42]
Decay time (fast component)	4.2 ns [42]
Decay time (slow component)	22 ns [42]
Absorption length	$>$ 100 cm
Scattering length	29 cm to 50 cm [40, 43, 44]

Because of its good property, there are many projects to utilize LXe, such as a dark matter search, a neutrinoless double beta decay search, a gamma ray astronomy, medical applications such as positron emission tomography (PET) and so on. However, there are difficulties as follows:

- Expensive,
- Stabilization of the temperature around 165 K (Phase diagram is shown in Figure 2.18),
- Decontamination of particles which absorb or decrease scintillation light (Section 2.4.4),
- Photon detector development which is sensitive to vacuum ultraviolet (VUV) scintillation light (Section 2.4.2).

Many studies were done with prototype detectors [45, 46], and we succeeded to construct and operate the MEG LXe detector [47].

Scintillation process [48, 49]

When a charged particle passes in LXe, it produces excited atoms (Xe^*) or ions (Xe^+).

In case of the excited atom, following scintillation process is known.

$$\begin{aligned} Xe^* + Xe &\rightarrow Xe_2^* \\ Xe_2^* &\rightarrow 2Xe + h\nu \end{aligned}$$

Excited atoms instantly form excimers and emit photons. The excimer has mainly two kinds of excited state; ${}^1\Sigma_u^+$ (decay time: 4.2 ns) and ${}^3\Sigma_u^+$ (decay time: 22 ns); and the intensity ratio of ${}^1\Sigma_u^+$ and ${}^3\Sigma_u^+$ depends on deposited energy density.

In case of the ions, scintillation process is as follows.

$$\begin{aligned} Xe^+ + Xe &\rightarrow Xe_2^+ \\ Xe_2^+ + e^- &\rightarrow Xe^{**} + Xe \\ Xe^{**} &\rightarrow Xe^* + \text{heat} \\ Xe^* + Xe + Xe &\rightarrow Xe_2^* + Xe \\ Xe_2^* &\rightarrow 2Xe + h\nu \end{aligned}$$

This process is slower because of the additional recombination process, and the decay time depends on the incident particles. The decay time of recombination process is 45 ns for electron. As shown in Figure 2.17, gamma-ray with energy > 10 MeV interact with LXe via electron pair production, so the time structure of scintillation light is the same as electron. When the incident particle is α or fission fragments, decay time is faster than the case of electron because of lager deposited energy density. This difference of the time structure of scintillation light is useful for particle identification.

In both of two processes, scintillation photon is emitted by a excimer Xe_2^*, not by a excited atoms Xe^*, thus there is no absorption by itself. This feature is very helpful to have good energy resolution and small dependence between reconstructed energy and incident position.

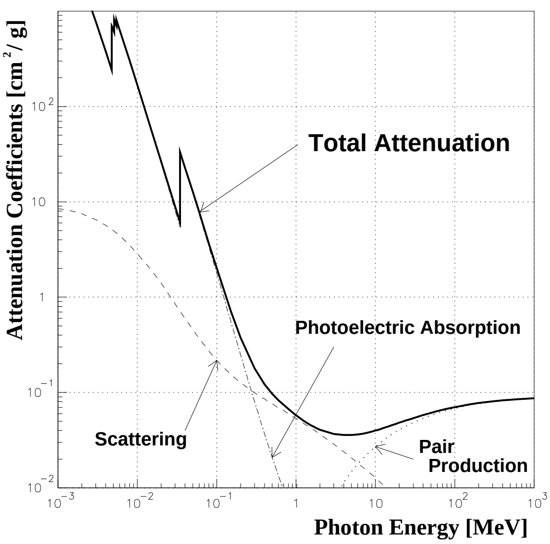

Figure 2.17: Photon interaction in LXe [50]

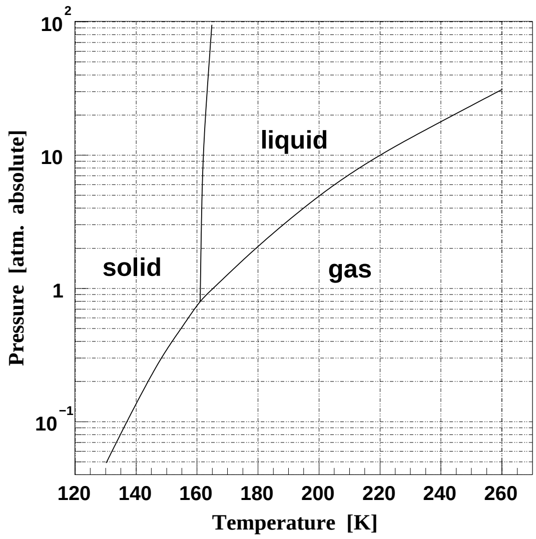

Figure 2.18: Xe phase diagram

2.4.2 Photomultiplier tube

Photomultiplier tubes (PMTs) of the MEG gamma-ray detector is used in LXe, so it is operated at low temperature and should sensitive to VUV. We developed a new model of PMT (R9869) with Hamamatsu Photonics.

A photo of the PMT is shown in Figure 2.19. The window of the PMT is made of synthetic quartz glass which is 80 % transparent to the scintillation light of liquid xenon. The photo-cathode material is bi-alkali (K-Cs-Sb). Aluminum strips are attached on the photo-cathode, because resistance of bi-alkali increase a lot at low temperature. This strip pattern covers 4 % of effective aria and supplies photo-cathode with electrons for the photoelectric effect. Quantum efficiency (Q.E.) is estimated to be approximately 15 % at 165 K. Metal channel dynode is adopted to make the PMT low material and tolerant to 50 Gauss stray field of the COBRA magnet. Figure 2.20 shows the voltage divider circuit of the PMT. To keep Xenon to be liquid stably, high resistance resistors are used to minimize heat generation. This unfortunately causes gain instability under high rate environment because the amplified electrons flying between dynodes make the ratio of the voltage division different. So zener diodes are inserted in parallel with the last two dynodes to make the voltage stable. Low noise zener diode RD-S series of NEC Co. is adopted. Selection is done taking the decrease of zener voltage due to low temperature into account. A resistor inserted in series with each zener diode makes low pass filter to prevent noise from the zener diode from having an effect on signal output.

Figure 2.19: Photo of R9869

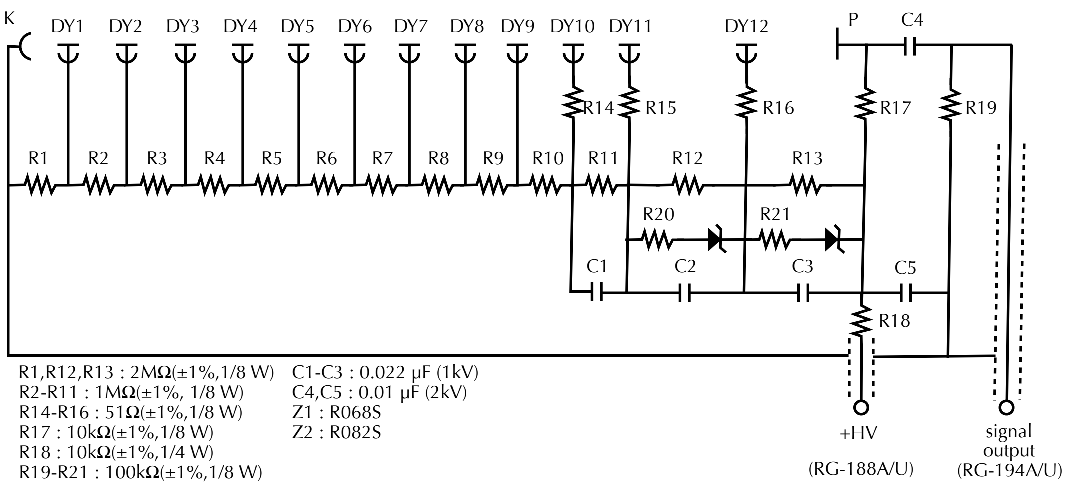

Figure 2.20: Voltage divider circuit of R9869

2.4.3 Design of the MEG liquid xenon gamma-ray detector

Design of MEG LXe detector is shown schematically in Figure 2.21, 2.22. Definition of each face and local coordinate system(see Section 2.1.1) are also shown. Liquid Xenon is used as scintillator. The active volume is approximately 800 liter and 900 liter liquid Xenon is used. The scintillation light is collected by 846 PMTs surrounding the active volume. The detector is C-shaped and covers the region approximately $30° < \theta < 120°$, $120° < \varphi < 240°$ and in total 11 % of the solid angle from the center of the stopping target. Outside the active volume, aluminum spacers are installed to save expensive xenon. The depth of the active volume is 38.5cm and it corresponds to approximately 14 X_0.

Gamma-ray from the target passes through a entrance window and inner face PMT. The entrance window for the gamma-ray should be thin and mechanically strong. The window is made of 0.7 mm thickness stainless steel plate reinforced with aluminum honeycomb covered with carbon fiber plates. The window corresponds to 0.075 X_0 in total.

The cryostat is made of non-magnetic materials. It has two layers of vacuum-tight vessels to apply vacuum thermal insulation. Xenon is cooled by A 200 W pulse-tube refrigerator, which is specially developed for this liquid xenon calorimeter [51]. Temperature of xenon is controled using this refrigerator with help of heater. Cooling pipes of liquid nitrogen are also available when a high cooling power is needed. A capacity level meter, several pressure sensors and Pt-100 temperature sensors are installed for monitoring the condition of xenon. We have two storages for xenon, 1000 liter LXe dewar [52] and high pressure gas tanks.

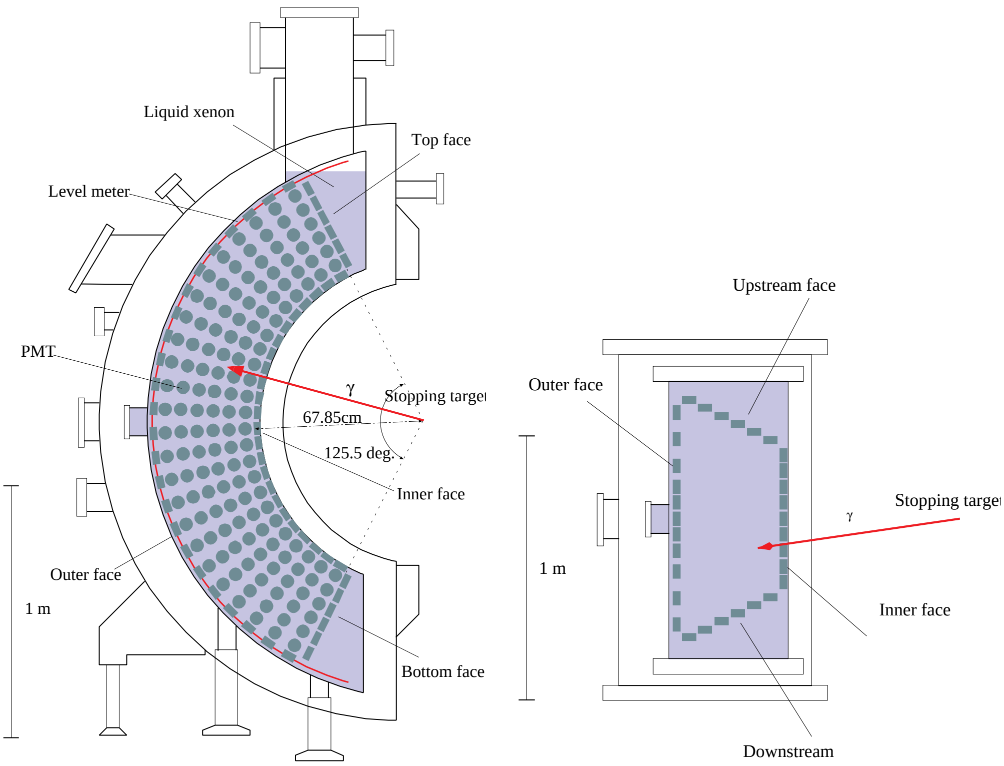

(a) side view (b) top view

Figure 2.21: Sectional drawings of the MEG LXe detector. Blue circle shows a PMT

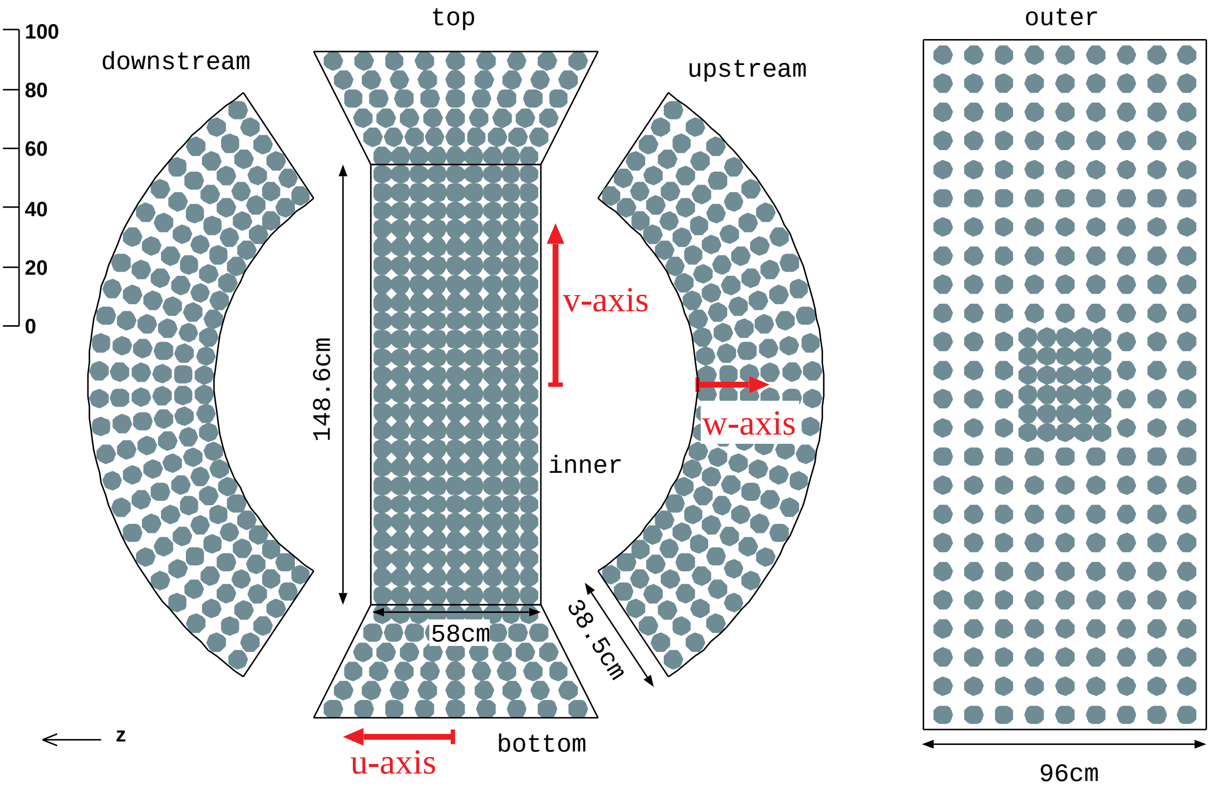

Figure 2.22: Development view of the MEG LXe detector

Figure 2.23: Picture of the LXe detector before closing outer and inner vessel covers.

2.4.4 Purification system

Scintillation light from LXe is vacuum ultra violet, which is easily absorbed and does not penetrate air as the name indicates. Fig. 2.24 shows absorption of the scintillation light by water vapor and oxygen. Water absorbs VUV light by the photo-dissociation process.

$$H_2O + h\nu \rightarrow H_2 + O^* \tag{2.5}$$

Air inside the detector is pumped out by a turbo-molecular pump before letting xenon in. Because some of the components inside the detector cannot be heated, we cannot perform baking procedure. Especially a small amount of water remains at the surface of the components inside and it causes scintillation light absorption.

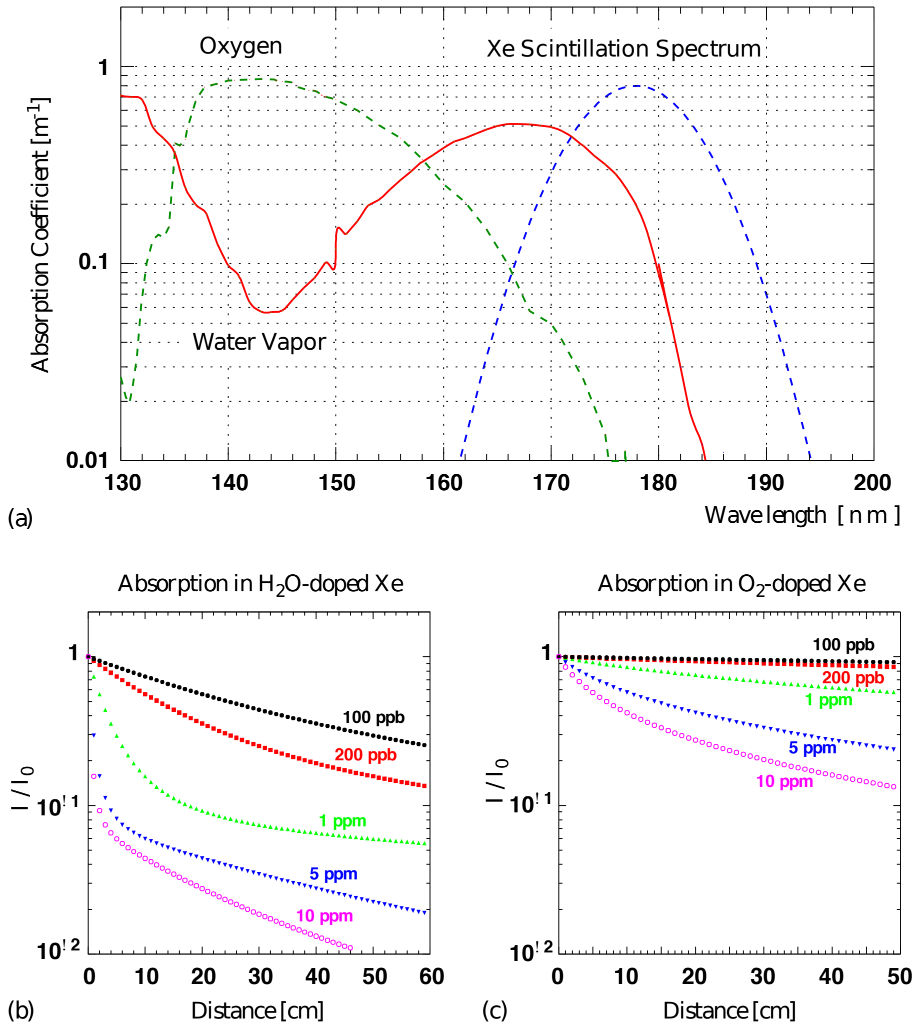

Figure 2.24: (a) Absorption coefficients for 1ppm water vapor and 1ppm oxygen. Xenon scintillation spectra is superimposed [53]. (b)(c) Scintillation light intensity and distance from a light source for different concentrations of water vapor and oxygen [46].

In addition to the absorption problem, there might exist contaminants which disturb scintillation process. For the case of liquid Argon, Nitrogen is considered to quench liquid argon by a following kinetic collision [54].

$$Ar_2^* + N_2 \rightarrow 2Ar + N_2 \tag{2.6}$$

This can change time structure of scintillation light, because excimer with longer life time is thought to be affected more. It is reported that suppression of slow component of the liquid argon scintillation light was observed when concentration of nitrogen increased [54]. This kind of quenching process is not well studied for LXe, but similar process can happen also in LXe.

To draw out LXe's high performance, several test was done using a prototype detector, and we developed two types of purification system [55, 56]. One is a gas-phase purification. Gas xenon is send to heated metal getter by a diaphragm pump. The speed of purification corresponds to be less than 0.1 liter/hour in liquid xenon. The purifier removes H_2O, O_2, CO, CO_2, H_2, N_2 and hydro carbon molecules from gas xenon down to 1.0 ppb level.

The other is a liquid-phase purification. Molecular sieves removes water contaminant and copper beads, which was developed for LAr TPC at CERN, removes oxygen by oxidization process. The speed of purification is 180 liter/hour.

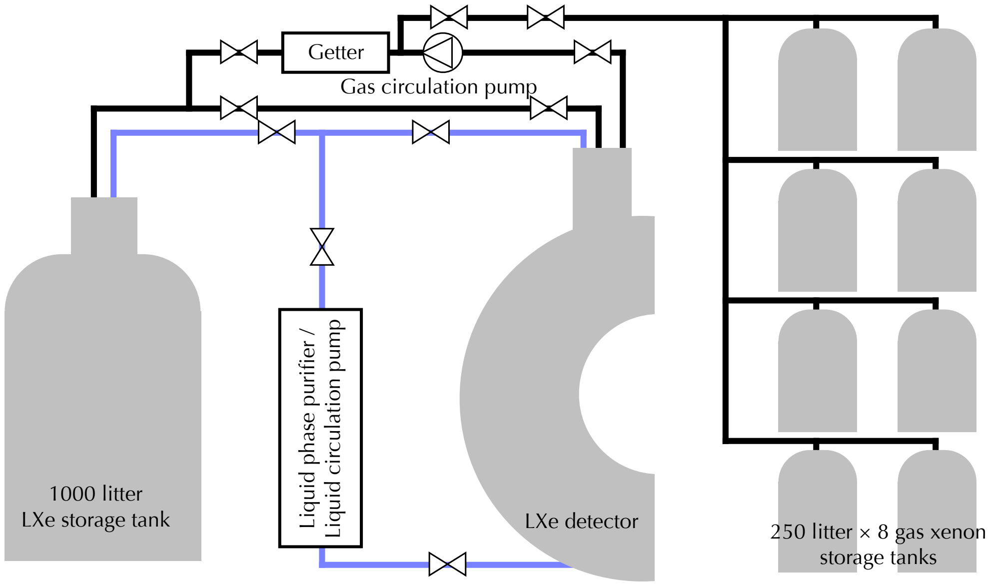

Figure 2.25: Schematics of purification line. Blue line shows pipe line for liquid xenon.

2.5 Calibration and monitoring

2.5.1 LED

PMT gain was measured by using LEDs installed in the LXe detector. The stability of gain was monitored daily by the calibration with LEDs. We applied attenuation of light to get stable light intensity. Principle of it is schematically shown schematically in Figure 2.27. Attenuated LED needs higher voltage to obtain the same amount of light. When the fluctuation of voltage is about the same, fluctuation of output light is smaller in case of the attenuated LED.

LED is covered with aluminum foil with small pinhole to attenuate its emission of light (Figure 2.26(a)). Teflon sheet is attached as a diffuser (Figure 2.26(b)). LEDs with three different attenuations are prepared. Picture of the installed LEDs are shown in Figure 2.28.

(a)

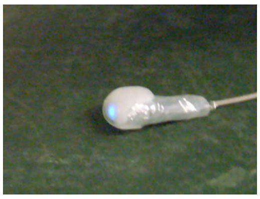

(b)

Figure 2.26: LED covered with aluminum foil with pinhole (2.26(a)), teflon sheet is attached for diffusion of light (2.26(b)). They are fixed by heat shrinkable tube

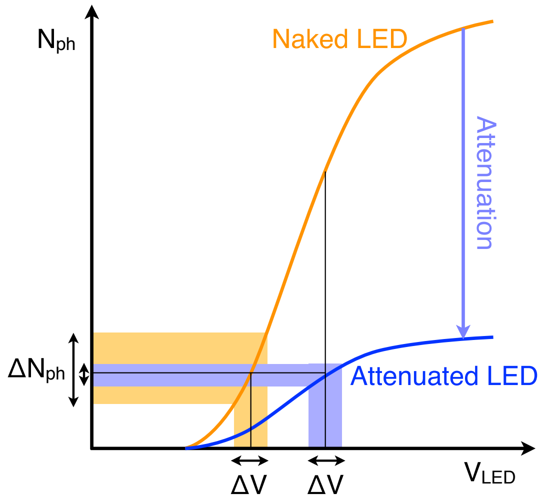

Figure 2.27: Schematics of how the attenuation of light works to make the fluctuation of the output light small. Curved line shows LED light intensity versus applied voltage, orange for naked and blue for attenuated LED.

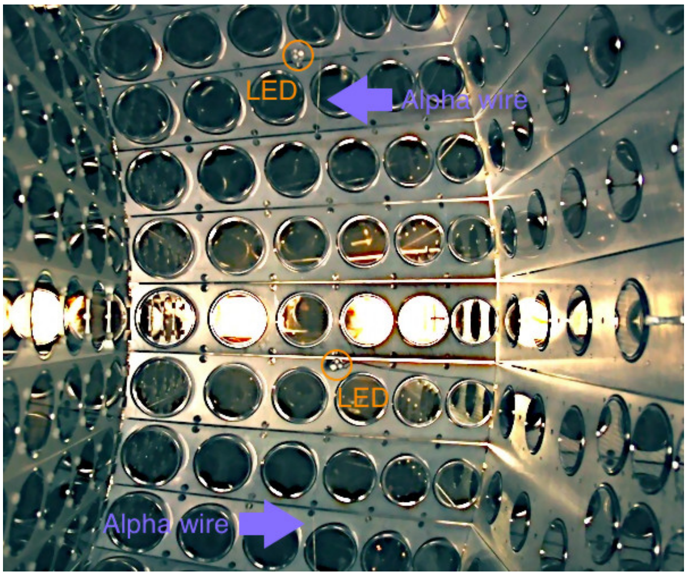

Figure 2.28: Alpha wires (blue arrow) and three LEDs with different attenuation (orange circle) installed between and on the lateral upstream and downstream face of the detector

2.5.2 ^{241}Am alpha source

We install ^{241}Am alpha source inside the LXe detector. It emits alpha-ray at 5.485 MeV (84.5%) and 5.443 MeV (13.0%), and its life time is 432 years. Since the rage of the alpha-ray is as short as 40 μm, it can be used as a point-like light source placed at a known position. We developed a thin tungsten wire of 100 μm diameter on which five alpha sources are deposited with interval of 12.4 cm. The source is protected by a thin gold layer ($\sim 1.5\mu$m) (Figure 2.29). Five wires are installed in the detector; a lattice of 25 alpha-source spots is formed in LXe detector. Figure 2.28 shows a photograph of alpha wires and LEDs installed in the detector. The activity of each source is about 200 Bq. Daily calibration with alpha source was used to measure and monitor Q.E. of PMTs.

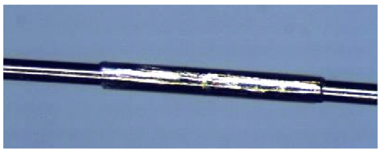

Figure 2.29: Microscope photograph of the ^{241}Am source on a wire. Diameter is 100 μm and longitudinal dimension is about 2 mm.

2.5.3 17.6 MeV gamma-line from $^{7}_{3}$Li(p, γ)$^{8}_{4}$Be reaction

A 17.6 MeV gamma-line is used to monitor and calibrate the LXe gamma-ray detector light yield. It is produced by a nuclear reaction; $^{7}_{3}\mathrm{Li}(\mathrm{p},\gamma)^{8}_{4}\mathrm{Be}$. The reaction is resonant at $T_p = 440$keV with resonance width $\Gamma_R \simeq 15$keV and cross section $\sigma_R \simeq 5$mb.

To produce proton-beam required to excite the reaction, we installed a Cockcroft-Walton (CW) proton accelerator at the downstream side of the experimental area (Figure 2.30(a), 2.30(b)). The properties of MEG CW accelerator is shown in Table 2.3. A part of the proton beamline is made of metallic bellows and the beam target can be moved at the center of the COBRA magnet. As the proton beamline does not interfere with the muon beamline and moving the muon stopping target and the CW beam target takes less than half an hour, taking data with CW proton beam can be performed frequently. The target is made of a thick lithium tetraborate ($Li_2B_4O_7$) crystal disk. We can select the reaction of $^{7}_{3}\mathrm{Li}(\mathrm{p},\gamma)^{8}_{4}\mathrm{Be}$ or $^{11}_{5}\mathrm{B}(\mathrm{p},\gamma)^{12}_{6}\mathrm{C}$ with the same target by changing the proton kinematic energy. The latter reaction gives coincident 11.7 MeV and 4.44 MeV gamma-rays, which can be used to calibrate timing between the gamma-ray detector and the timing counters. Energy spectrum of 17.6 MeV gamma-line seen by the LXe detector is shown in Figure 2.31. Also visible is the broad 14.3 + T_p MeV gamma-line, corresponding to the ^{8}Be transition to the first excited state of ^{8}Be(γ1).

Table 2.3: Properties of MEG CW accelerator

	Nominal	Measured at PSI
Terminal energy range (keV)	300 – 900	200 – 1100
Energy ripple (RMS eV)	< 500	< 500
Angular divergence (mrad $\times$ mrad)	5×5	$\sim 4 \times 4$
Spot size at 3 m (cm $\times$ cm)	$< 3 \times 3$	< 1
Energy setting reproducibility (%)	0.1	OK
Energy stability (FWHM %)	0.1	OK
Range of current (%)	1 – 100	0.1 – 135
Current stability (%)	3	OK
Current reproducibility (%)	10	OK
Duty cycle (%)	100	OK
Start-up time (min)	< 20	< 15

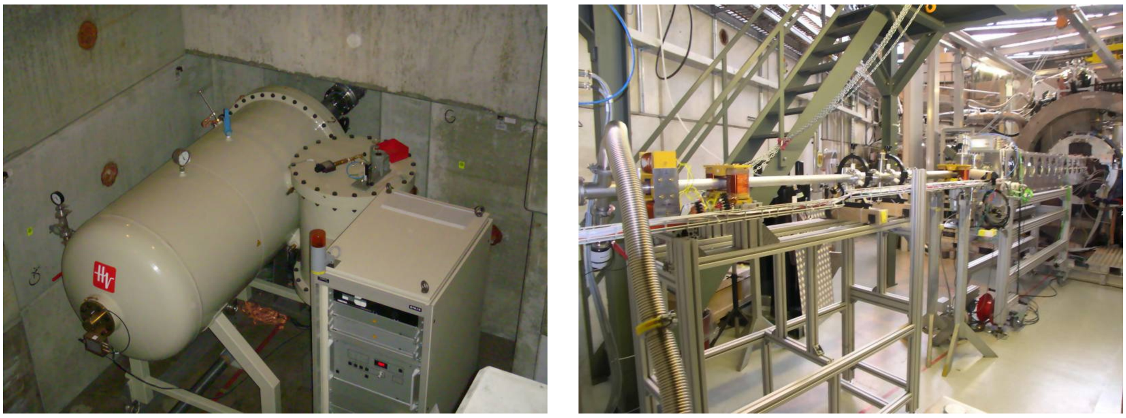

Figure 2.30: CW accelerator and its beam line at the downstream side of the MEG.

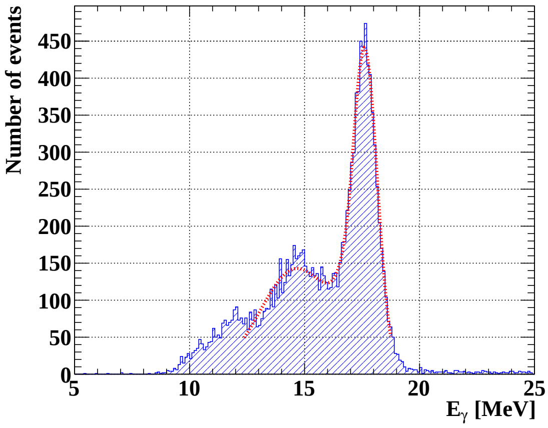

Figure 2.31: Energy spectrum of CW run

2.5.4 55 MeV gamma-ray from π^- Charge exchange reaction

π^- beam and hydrogen target

We perform dedicated calibration run of the LXe detector for a certain period once or twice per year. During this period, πE5 beamline is tuned to provide π^- beam to the center of the COBRA magnet, where we place liquid hydrogen as the target. The momentum of the pion beam is set to 70 MeV/c, which is optimal in our set up to remove electrons and muons. Expected pion rate at the center of COBRA magnet is 1.6MHz at 1.8mA primary proton current. Measured pion profiles in vertical and horizontal direction was 8mm in σ. Liquid hydrogen target is a cylindrical cell of 50mm diameter, 75 mm length, closed on the entrance side by a thin 135 μm mylar window. Hydrogen is liquified and maintained in a stable state with a liquid helium.

When a negative pion collide with hydrogen, following two kinds of process can occur. One is radiative capture reaction ($\pi^- p \to \gamma n$), which gives a gamma-ray of energy 129.4MeV. Anther is a charge exchange (CEX) reaction ($\pi^- p \to \pi^0 n$), which gives two gamma-rays by the decay of neutral pion. The ratio of the two channels is known as Panofsky ratio [57, 58],

$$P = \frac{\sigma(\pi^- p \to \pi^0 n)}{\sigma(\pi^- p \to \gamma n)} = 1.5. \tag{2.7}$$

The neutral pion produced by CEX has momentum of 28 MeV/c in laboratory frame, and 98.8% of that decays into two gamma-rays ($\pi^0 \to \gamma\gamma$) immediately with life time 8.4×10^{-17}. Because it's two body decay, both gamma-rays have half the π^0 mass (= 67.49MeV) in the rest frame of π^0, and because of the effect of Lorentz boost, the energy of a gamma-ray distribute flat between 54.9 MeV and 82.9 MeV in the laboratory frame. Relation between energy of a gamma-ray and opening angle between two gamma-rays in laboratory frame is shown in Figure 2.32. This plot shows that we can obtain quasi-monochromatic gamma-ray with energy 54.9 or 82.9 MeV when we select gamma-rays with opening angle near 180 degree.

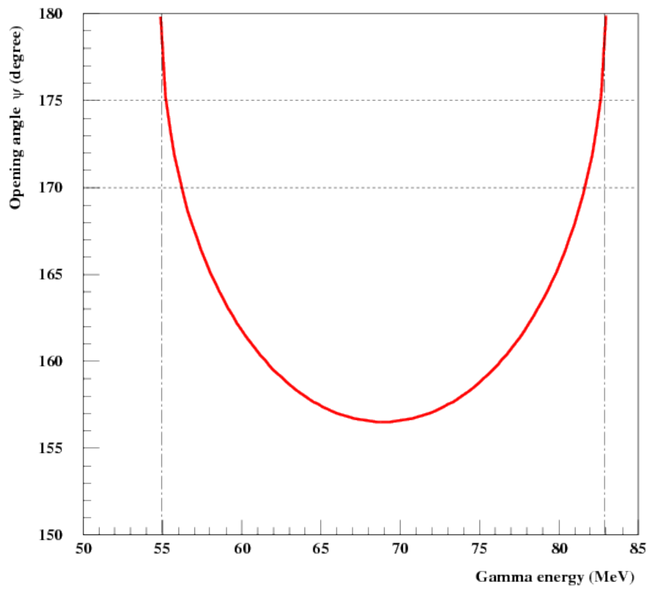

Figure 2.32: Energy and opening angle of gamma-ray from CEX π^0 decay.

Figure 2.33: NaI mover and housing box for the NaI.

NaI detector

By selecting events in which a gamma-ray with energy of 82.9 MeV is emitted at the opposite of the LXe detector, we can obtain quasi-monochromatic 54.9 MeV gamma-ray events with the LXe detector. At the opposite side of the LXe detector, NaI gamma-ray tagging detector is placed.

NaI detector is composed of 3×3 crystals of NaI ($62.5 \times 62.5 \times 300.5\text{mm}^3$) viewed by Avalanche Photo Diode (1cm $\times$ 1cm, S8664-1010 made by Hamamatsu) readout. When we perform timing calibration run, a lead converter ($50 \times 50 \times 5\text{mm}^3$) and two plastic scintillators ($60 \times 60 \times 7\text{mm}^3$) viewed by 2×2 fine-mesh PMTs (Hamamatsu H6152-70) are attached in front of the NaI detector.

NaI tagging detector is mounted on a mover (Figure 2.33) to cover the whole acceptance of the LXe detector.

2.6 Electronics and data acquisition

2.6.1 Data acquisition

In the MEG experiment, waveforms of each detector are recorded. We have two different waveform samplers. One is flash analog to digital converter (FADC) with 100 MHz sampling and 10 bits resolution, which is used for trigger system. The other is Domino Ring Sampler (DRS) [59] developed in PSI, which is a waveform digitizer with switched capacitor arrays (SCAs). DRS has 950 MHz bandwidth at a variable sampling rate up to 6 GHz with 1024 cells. The waveform stored in the sampling cells is read out by a shift resistor at lower frequency (33 MHz) and digitized externally by a 12-bits commercial FADC. We set the sampling frequency to 1.6 GHz for the outputs from the gamma-ray detector and the TICP and 800 MHz for the outputs of the drift chambers.

The data flow from detectors to digitizers is shown in Figure 2.34.

Output of LXe PMT is put in active splitters. Input signal is received by a differential amplifier, then the output of an amplifier with 1.9 GHz bandwidth goes to DRS and the output of an amplifier with 320 MHz bandwidth or analog sum of four waveform goes to trigger.

TICP PMT output is divided by a passive splitter at the ratio of 8 : 1 : 1. The largest signal is put into double-threshold discriminator (DTD), and NIM signal is obtained. The lower threshold of DTD makes a good timing performance with a less effect of a time walk, and the higher threshold ensures the signal to be a positron hit event, not a fake signal due to noise or delta-ray hits. One of smaller outputs of the passive splitter and DTD NIM output are put in the active splitter and goes to DRS and trigger. The other output of the passive splitter goes to current monitor to check the PMT lifetime.

DCH outputs are first amplified by a preamplifier attached at the chamber frame structure. Anode wire signal is then resistively divided at the ratio of 9 : 1. Larger output of anode wire and cathode pad go to DRS. Sum of several smaller output of anode wires goes to the trigger.

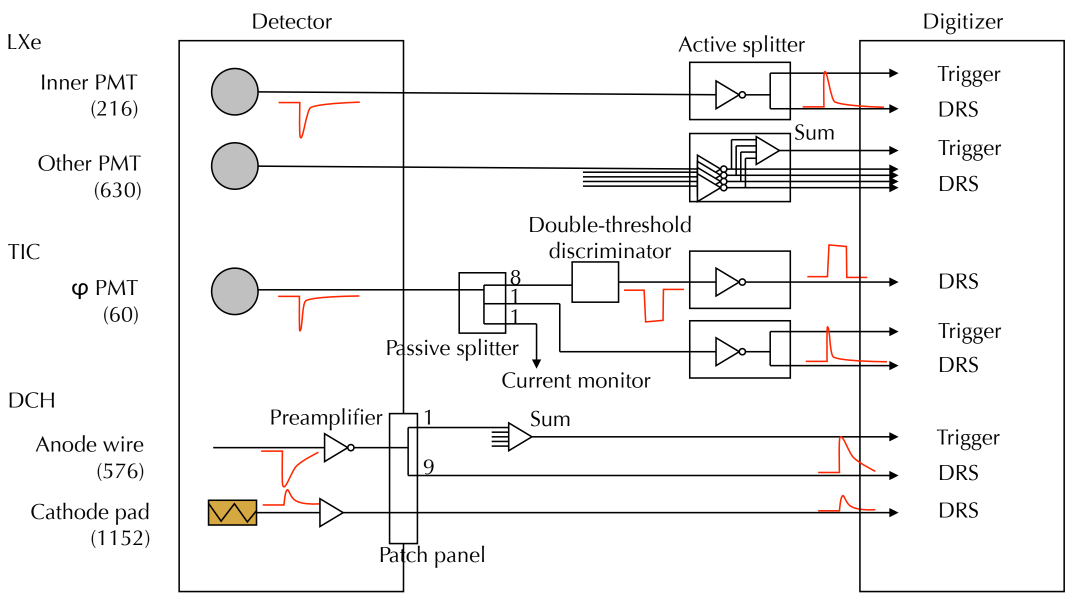

Figure 2.34: Schematics of data flow and electronics.

2.6.2 Trigger system

In the trigger system, the output of FADC is processed by field programmable gate arrays (FPGAs). Online reconstruction and trigger selection are programed on FPGA. Several trigger settings can be used simultaneously. Trigger rate is controlled by pre-scale factor. When pre-scale = 100, one per 100 triggered events is recorded. We count the number of triggered events and record live and dead time for each trigger type. For $\mu^+ \to e^+\gamma$ search trigger, DAQ live time is $\sim$ 84 % and the trigger rate is 5 Hz.

A example of trigger types and the selection criteria in the $\mu^+ \to e^+\gamma$ search run is listed in Table 2.4. $\mu^+ \to e^+\phi, \phi \to \gamma\gamma$ dedicated trigger is not prepared, and we use the $\mu^+ \to e^+\gamma$ search data to search for $\mu^+ \to e^+\phi, \phi \to \gamma\gamma$ decay mode. Direction match is the tightest trigger condition for $\mu^+ \to e^+\phi, \phi \to \gamma\gamma$ event. It is based on a comparison of the emission direction estimators of the positron and the gamma. For the $\mu^+ \to e^+\gamma$ event, positron and gamma-ray are back to back and have monochromatic energy, so the hit position in LXe and TICP are related. A look up table of the index number of inner face PMT with the highest output and z position of the TICP bar that positron hits first is made using $\mu^+ \to e^+\gamma$ MC simulation.

Because the sum of the energies of gamma-rays of $\mu^+ \to e^+\phi, \phi \to \gamma\gamma$ is larger than 52.8 MeV, E_γ threshold is justified, but if the mass of the ϕ is large enough, the sum of the energies of gamma-rays can become close to the cosmic veto threshold.

Detailed description about the trigger system is found in Ref. [60].

Table 2.4: Trigger setting for $\mu^+ \to e^+\gamma$ search run at one period of 2010. Pre-scale factor can be changed according to request. E_γ Threshold low $\sim$ 40 MeV, high $\sim$ 44 MeV, CR veto $\sim$ 62 MeV(2009), 75 MeV (2010), $\Delta T_{e\gamma}$ narrow $\sim$ 20 ns, wide $\sim$ 40 ns

Id	Trigger type	Pre-scale	E_γ THR	$\Delta T_{e\gamma}$	Direction match
0	MEG	1	high & CR veto	narrow	narrow
1	MEG Low E_γ	60	low & CR veto	narrow	narrow
2	MEG Wide DM	550	high & CR veto	narrow	wide
3	MEG Wide T	250	high & CR veto	wide	narrow
4	$\mu^+ \to e^+\nu_e\overline{\nu}_\mu\gamma$	1100	low & CR veto	narrow	–
9	LXe alone	20000	high & CR veto	–	–

Id	Trigger type	Pre-scale	Selection criteria
12	α	22000	Pulse shape discrimination
14	LEC	6	1 Hz pulse from LED driver module
18	DC alone	1.5×10^7	DC hit multiplicity
22	TIC alone	1×10^7	TIC multiplicity
27	LXe Cosmic	2500	Threshold on E_γ
31	Pedestal	20000	Random trigger

Part III

Reconstruction, simulation and the performance

Chapter 3

Analysis software and simulation

3.1 The MEG software

We developed three packages of softwares; MEGMC, MEGBartender and MEGAnalyzer. Relation of each software is shown in Figure 3.1.

MEGMC is GEANT3.21 [61] based Monte Carlo simulation program, which simulates kinematics of events, interaction of particles with materials of detectors, propagation of scintillation photons in the LXe detector, number of photons entering TIC PMTs, and drift of electrons and ions in the drift chambers. We change event types and the detector settings modifying parameters in the configuration file for the simulation. All parts of positron spectrometer and LXe detector are represented with actual dimensions, materials, and arrangement. Electrical field of drift chamber is calculated with GARFIELD [62].

MEGBartender simulates electronics and waveform. It can also simulate pileup events by mixing MEGMC data sets.

MEGAnalyzer does waveform analysis and event reconstruction for both MC simulation data and experimental data. MEGAnalyzer can also process output of itself. In the second process, we can skip time-consuming waveform analysis, or select events with rough reconstruction to perform precise reconstruction.

MEGAnalyzer and MEGBartender are are organized by the analysis framework toolkit, ROME [63]; ROOT [64] based Object Oriented Midas Extension.

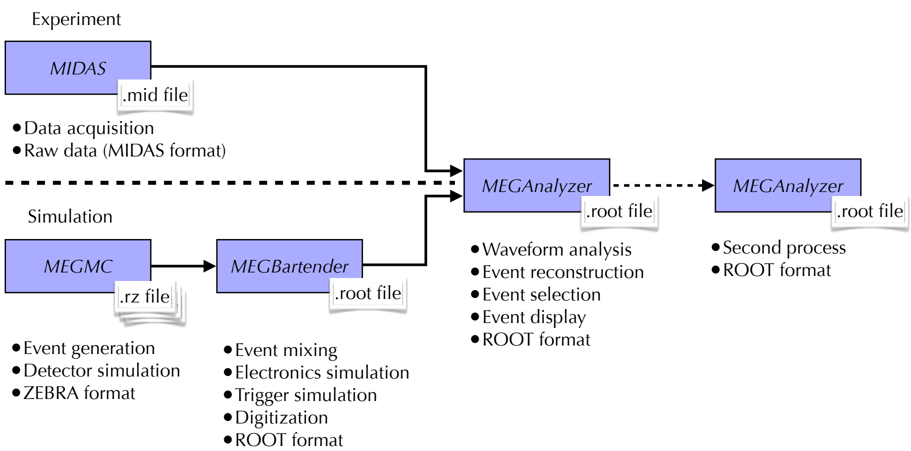

Figure 3.1: Structure of the MEG Software

3.2 $\mu^+ \to e^+\phi, \phi \to \gamma\gamma$ Monte Carlo event generation

In this section, event kinematics of $\mu^+ \to e^+\phi, \phi \to \gamma\gamma$ decay and its generation in Monte Carlo (MC) simulation are discussed. Rn represents a random number from 0 to 1.

MC event is generated assuming $\mu^+ \to e^+\phi, \phi \to \gamma\gamma$ to be two sets of clear two body decay and each particles are emitted isotropically in the center of mass system of decaying particle. One e$^+$ and two gamma-rays are generated in the program. Mass (M_ϕ) and lifetime (τ_ϕ) of ϕ are set as input parameters by a configuration file.

Extracted e^+ has a monochromatic momentum equal to that of ϕ;

$$P_\phi = P_{e^+} = \sqrt{((M_\mu^2 + M_e^2 - M_\phi^2)^2 - 4M_\mu^2 M_e^2)}/(2M_\mu). \tag{3.1}$$

e$^+$ is generated on the muon stopping target taking the beam spot size into account, and the direction is set isotropically within a region set by the configuration file. Then speed of ϕ is calculated by

$$\begin{aligned} \beta_\phi &= P_\phi / \sqrt{M_\phi^2 + P_\phi^2}, \\ \gamma_\phi &= 1/\sqrt{1-\beta_\phi^2}. \end{aligned} \tag{3.2}$$

By relativistic effect, effective lifetime of ϕ in the experimental system becomes $\gamma_\phi\tau_\phi$, so time and position differences between e$^+$ and gamma-ray generation are

$$\Delta t = -\gamma_\phi \tau_\phi \ln(\text{Rn}), \tag{3.3}$$
$$\Delta\text{position} = \beta_\phi c \Delta t. \tag{3.4}$$

Gamma-rays are generated at opposite side of e$^+$ direction with the distance Δposition apart from e$^+$ generation point with a time difference Δt later than e$^+$.

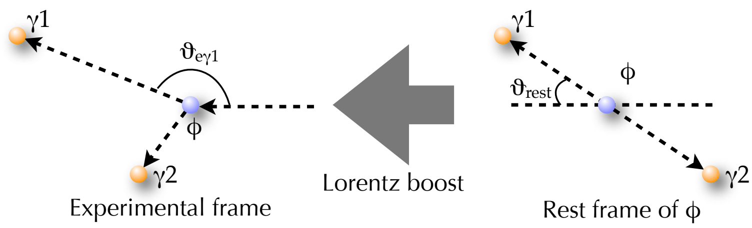

Figure 3.2: Kinematics of two gamma-rays

In the rest frame of ϕ, energy of gamma-rays are both $M_\phi/2$, and the direction of gamma-ray can be described as $\cos\vartheta_{\text{rest}}$ =Rn when gamma-rays are generated isotropically. Then, energy of gamma-rays in the experimental frame is calculated as

$$\begin{aligned} E_{\gamma 1} &= \gamma_\phi M_\phi/2 + \gamma_\phi\beta_\phi \cos\vartheta_{\text{rest}} M_\phi/2 \\ E_{\gamma 2} &= \gamma_\phi M_\phi/2 - \gamma_\phi\beta_\phi \cos\vartheta_{\text{rest}} M_\phi/2 \end{aligned} \tag{3.5}$$

And angles between e$^+$ and $\gamma 1$, $\gamma 2$ direction ($\vartheta_{e\gamma 1}$, $\vartheta_{e\gamma 2}$) in the experimental frame have following correlations from momentum conservation.

$$\begin{aligned} \cos\vartheta_{e\gamma 1} &= (E_{\gamma 2}^2 - E_{\gamma 1}^2 - P_{e^+}^2)/(2E_{\gamma 1}P_{e^+}) \\ \cos\vartheta_{e\gamma 2} &= (E_{\gamma 1}^2 - E_{\gamma 2}^2 - P_{e^+}^2)/(2E_{\gamma 2}P_{e^+}) \end{aligned} \tag{3.6}$$

Direction of each gamma-ray is determined by this relative angle, and is rotated isotropically around e^+ direction. Then, these directions are checked whether within a region set by the configuration file or not, and if they are, the event is generated.

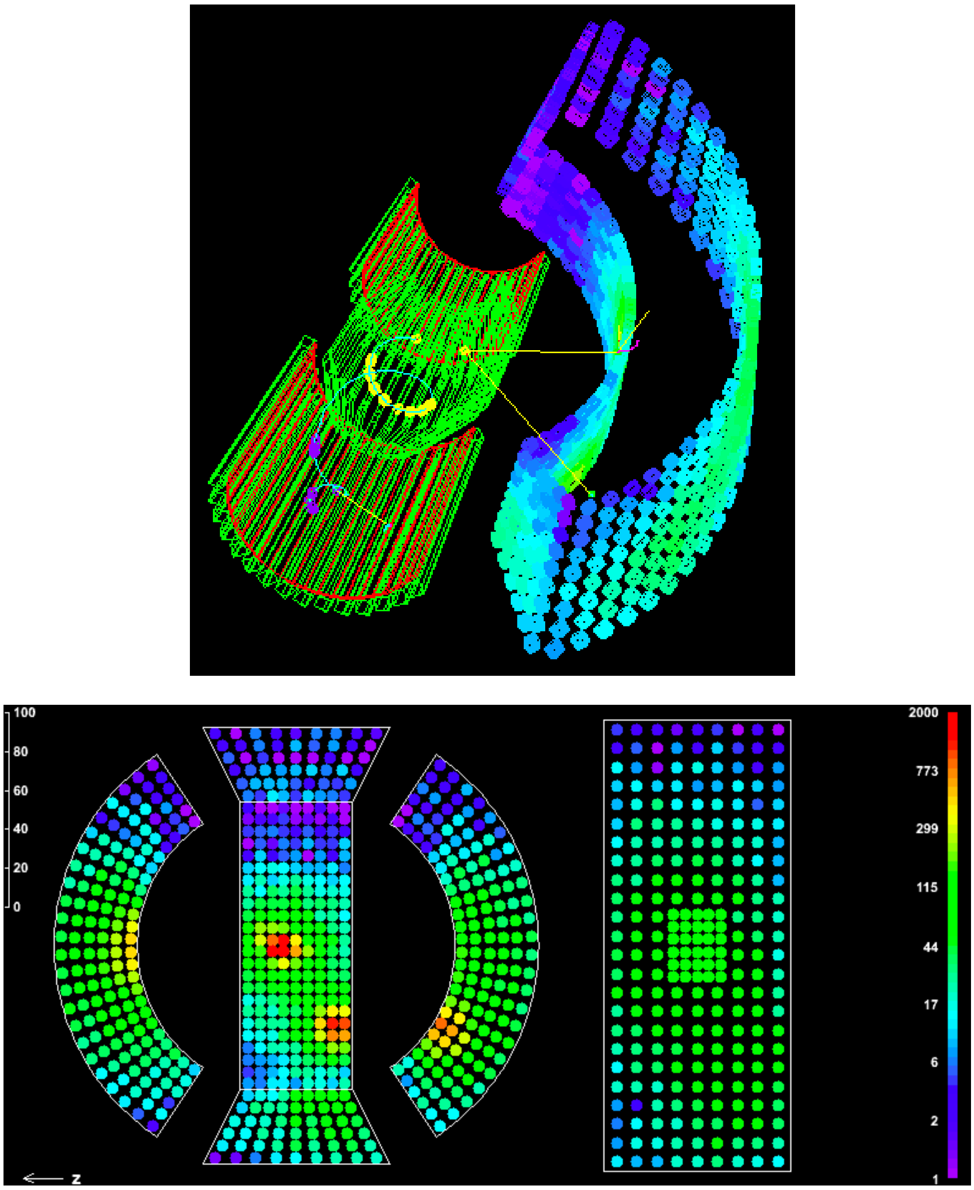

Figure 3.3: An example of generated $\mu^+ \to e^+\phi, \phi \to \gamma\gamma$ MC event ($M_\phi = 20$ MeV).

3.3 Reconstruction sequence

Reconstruction sequence for $\mu^+ \to e^+\phi, \phi \to \gamma\gamma$ search is shown in Figure 3.4.

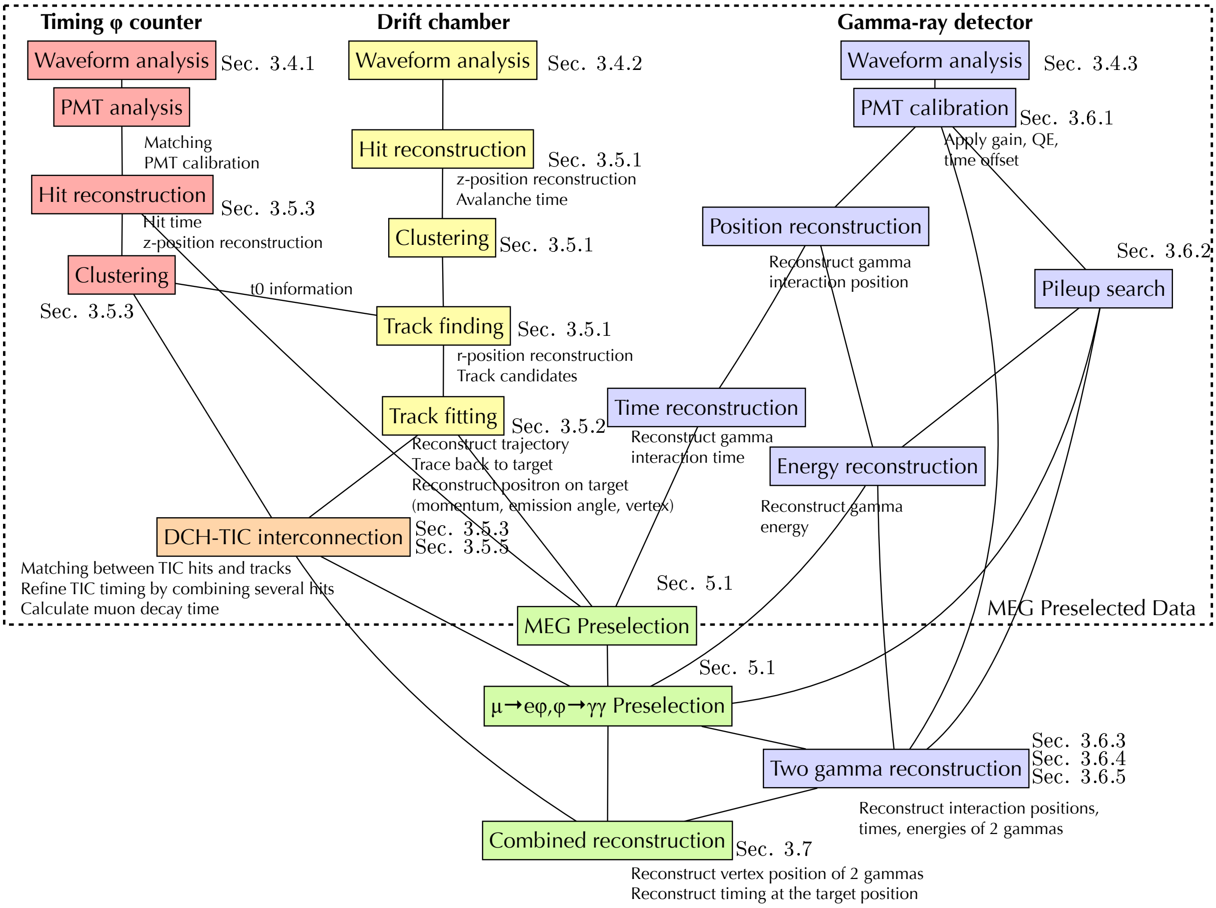

Figure 3.4: Reconstruction sequence and section number in which each item is described.

Just after the physics data is taken, the first processing; waveform analysis (Section 3.4) and rough reconstructions; are done. Then preselection for $\mu^+ \to e^+\gamma$ search is performed to reduce the data size. In this stage, the quality of calibration is not supposed to be excellent, so the preselection is determined to be enough loose not to discard any good events. After that, second processing is done taking all the calibrations into account. We use this second-processed data for $\mu^+ \to e^+\phi, \phi \to \gamma\gamma$ search.

Because the data in this stage contains a lot of events not needed for $\mu^+ \to e^+\phi, \phi \to \gamma\gamma$ search, preselection for $\mu^+ \to e^+\phi, \phi \to \gamma\gamma$ is performed. The selection criteria is described in Section 5.1. The selected events are then processed with third-process to reconstruct position, time and energy of each two gamma-rays (Section 3.6) and the vertex position of ϕ decay point (Section 3.7). Reconstruction of positron track (Section 3.5) is already done, so the reconstruction is skipped and the values processed in the second-process is copied to be used in the combined reconstruction.

3.4 Waveform analysis

We record signals of the detectors in the format of waveform. Extraction of time and charge is performed for each detector according to the characteristics and requirements of the detector.

3.4.1 Waveform analysis of drift chamber

As mentioned in Section 2.3.2, we have 16 drift chamber modules (DCH), 18 wires for each module, and 6 readout channels for each wire (2 from both ends of anode wire. 4 from corresponding cathode pads, that is inner pads and outer pads with two vernier-pattern pads). All in all, we have 16 (modules) $\times$ 18 (wires) $\times$ 6 (channels) = 1728 readout channels. In order to reduce the data size, we apply zero-suppression by discarding zero-signal waveform without recording at the online data taking stage. We can also reduce data size of recorded waveform by re-binning the part of the waveform outside the region around the signal peak.

Informations of hits on DCH are extracted from the recorded waveform of wires and cathode pads. A pulse identification is done by searching for the maximum peak bigger than a certain threshold. The width of the pulse is extracted by pursuing the waveform from the peak in the both directions until it crosses the another threshold. Then, this pulse range is masked and the pulse search is repeated because multiple hits on the same channel can happen.

Time extraction

Time of each pulse is determined by a single-threshold crossing time.

Charge extraction

Charge is extracted by integrating each pulse in a integration window. This window is determined by the anode wire waveform, and used also for the waveform of corresponding cathode pads. The window width is set to 50 ns, which was tuned to optimize the signal-to-noise ratio.

3.4.2 Waveform analysis of timing counter

We record two types of waveforms for timing φ counter (TICP), raw PMT signal and DTD-output NIM pulse, as described in Section 2.6.2.

Time extraction

Information of hit time is obtained by fitting a NIM pulse with a template waveform, which is prepared in advance for each channel by averaging many pulses.

Charge and amplitude extraction

From the raw PMT signal, we get an amplitude and a charge. The amplitude is obtained by comparing the estimated baseline and the pulse peak voltage. This is used for time-walk correction of the NIM-pulse time. The charge is obtained by integrating a pulse with 30 ns integration window. This is used to measure the gains to equalize raw PMT waveforms.

3.4.3 Waveform analysis of gamma-ray detector

We record waveforms of the 846 PMT outputs of the LXe detector. To reduce the data size, we perform re-binning outside the region of interest at the online data taking stage by recording one point per eight sampling points with the average of them. Reduction is not done for leading edge, peak, and the region just before the leading edge. The region to be reduced can be changed by trigger types.

We observed noises originating from the data acquisition DRS chips. Template waveform is made for each channel and subtracted for the noise reduction.

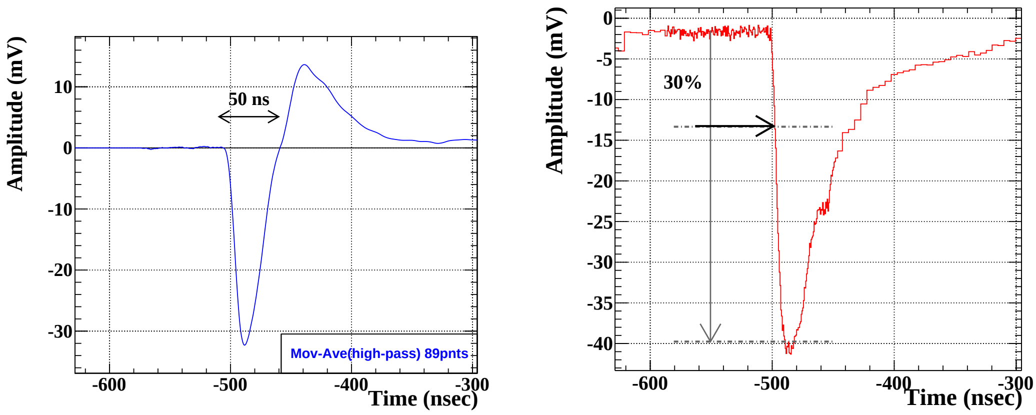

(a) The digital-constant-fraction method (b) High pass filtered waveform

Figure 3.5: LXe waveform

Time extraction

Digital-contant-fraction method is applied to extract time for each PMT. In this method, we can reduce the time-walk effect. Time is determined by the point where the leading edge crosses 30 % of the full pulse height (see Figure 3.5(a)). Here, we do not use the actual pulse height. We measure the relation between the pulse height and the charge in advance. Amplitude is calculated by the charge according to this relation to reduce the effect of noise and the statistical fluctuation of the pulse shape. No filtering is performed not to distort the leading edge shape.

If two gamma-rays are coming close in time and position, time of an earlier gamma-ray or a gamma-ray with larger pulse height will be extracted. Time extraction method dedicated to the pileup event is not prepared.

Charge extraction

High-pass filtered waveform is used for charge extraction of gamma-ray events. ~ 1 MHz noise was observed on PMT waveform, and this noise component is eliminated with this filtering. As shown in Figure 3.5(b), the pulse shape becomes sharper and the baseline becomes flat at zero. Fluctuation of the baseline calculation disappears. The window for the charge integration is determined by using summed waveform, and is used for each PMT commonly. The width of window is set to 48 ns. The narrower time window is effective to reduce pileup gamma-ray coming with some time difference. When a gamma-ray interacts very near to a PMT, the output voltage exceeds a dynamic range of the electronics, and the recoded waveform is saturated. The charge of such PMTs are estimated by time-over-threshold (ToT) method. The time width that a pulse exceeds a given threshold is measured and converted to the charge by using an average pulse shape of gamma-ray interaction events.

3.5 Reconstruction of positron tracks

Positron trajectory is reconstructed using drift chamber modules (DCH). Hit position on a module is reconstructed using signals on anode wires and cathode pads. Then Kalman filter track fitting is performed to reconstruct the track. Muon decay vertex position, positron emission direction, positron momentum and time of flight of positron are extracted from the tracking. Positron hit time is measured by timing φ counter , and together with the reconstructed time of flight, muon decay time is reconstructed.

3.5.1 Hit reconstruction and track finding

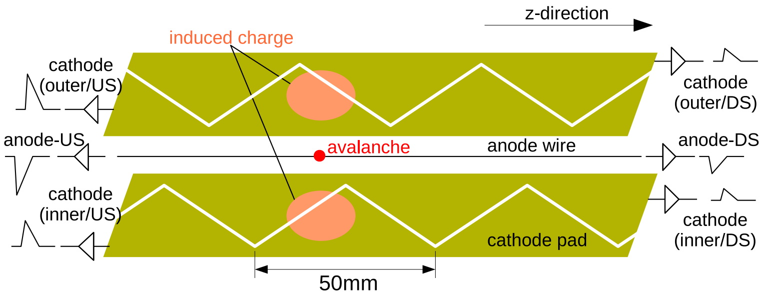

Figure 3.6: Schematic view of the vernier pad method

At first, positron hit z position in a drift cell of a DCH is roughly reconstructed with an accuracy of 1 cm by the ratio of charges measured at both ends of the sense wire, then is reconstructed more precisely using the vernier pad information. Vernier pad method is shown schematically in Figure 3.6. Phases of the Vernier pattern are shifted by 1/4 of a period between inner and outer pads. We measure charges of four vernier pads in a drift cell; outer cathode readout at upstream/downstream(Q_{OU}, Q_{OD}), inner cathode readout at upstream/downstream(Q_{IU}, Q_{ID}). The normalized charge ratio for outer cathode pads (ϵ_1) and inner cathode pads (ϵ_2) is written as follows.

$$\epsilon_1 = \frac{Q_{IU} - Q_{ID}}{Q_{IU} + Q_{ID}}, \epsilon_2 = \frac{Q_{OU} - Q_{OD}}{Q_{OU} + Q_{OD}} \tag{3.7}$$

Figure 3.7(a) shows a scatter plot of ϵ_1 versus ϵ_2 the phase of the vernier pattern; $\alpha = \arctan \epsilon_2/\epsilon_1$. Each line in Figure 3.7(b) indicates the n-th vernier periods on α versus charge division plane. z is reconstructed by

$$z = \frac{l}{2\pi} \cdot \alpha + \delta_{pad} \tag{3.8}$$

where l is the pattern pitch (5 cm) and δ_{pad} is a center position of the pad cycle where the hit exist. The resolution of z is estimated approximately 700 μm.

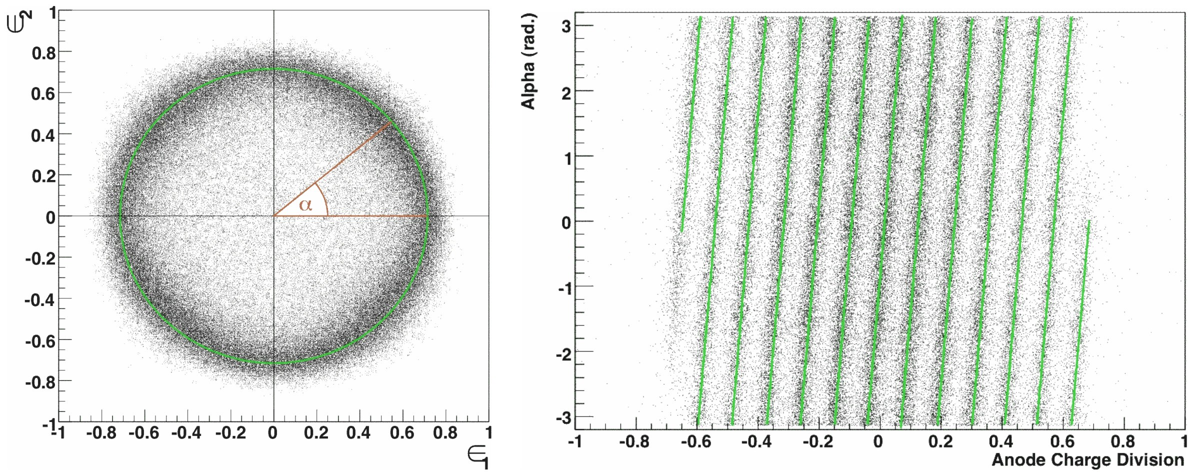

(a) Vernier circle. (b) Phase on vernier circle and anode charge division.

Figure 3.7: Muon stopping target

Because each DCH module is composed of two layers, one module has more than one hit when a positron crosses the module. The clustering of hits in each module is done using z and drift chamber hit time information. Then, we start to find track. First, we search for clusters with the distance from the beam axis larger than 24 cm, because we want to find positron with high momentum efficiently for the $\mu^+ \to e^+\gamma$ search. Then we perform circle fit with three clusters and search for the hit clusters for the same positron track with the smaller distance from the beam axis. Using relative position of hits, the angle that the positron passes the DCH is estimated. This incident angle and an estimation of drift time are used for the reconstruction of the distance between the sense wire and the positron track.

3.5.2 Tracking

Track fitting is performed by means of the Kalman filter technique [65]. It is effective for tracks with small number of hits or noisy environment, thus suitable for the positron tracking in MEG experiment. The features of the Kalman filter are as follows.

- Effects of multiple scattering, energy loss of positron and non-uniform magnetic field are handled correctly.
- Three-dimensional and complex trajectory can be reconstructed.
- Error propagation is taken into account.

The muon decay vertex ($\vec{x}_{\mu\mathrm{decay}}$), direction of positron emission ($\theta_{rec,\vec{dir}_{e^+}}$, $\varphi_{rec,\vec{dir}_{e^+}}$) and the momentum of the positron (P_{rec,e^+}) are fitted by this track fitting.

3.5.3 Positron time

Time walk of TICP NIM pulse is corrected using pulse height of the PMT waveform and a lower threshold in double-threshold discrimination. The hit position in z-coordinate is reconstructed by the time difference between the two PMTs at the both sides of the bar. Then, TICP hit time is reconstructed using the corrected NIM pulse time of the two PMTs and the hit z position. Positron with high momentum often put hits on some of bars. In this case, hits associated with a positron track are clustered by their time and z hit position. Then the timing counter hit time (t_{TIC}) is given by the time of the first bar hit.

The time of flight (TOF) of positron is estimated from the length of the reconstructed positron trajectory. Then the time of muon decay is estimated by subtracting TOF from the timing-counter hit time.

$$t_{e^+} = t_{TIC} - t_{tof,e^+} \tag{3.9}$$

3.5.4 Positron correction

An error on energy reconstruction of positron corresponds to an error on trajectory diameter. So reconstruction of muon decay vertex position especially in y coordinate and positron emission angle especially in φ coordinate are influenced by an error on energy reconstruction. Coefficients of the correlation function between δP_{e^+} and $\delta \varphi_{e^+}$ or $\delta y_{\mu\mathrm{decay}}$ are extracted using $\mu^+ \to e^+\gamma$ MC simulation data, and confirmed with $\mu^+ \to e^+\nu_e\overline{\nu}_\mu$ data taken with the MEG detector and $\mu^+ \to e^+\nu_e\overline{\nu}_\mu$ MC simulation data.

As the correction coefficients are derived for the positron with energy equal to half the muon mass, correction for $\mu^+ \to e^+\phi, \phi \to \gamma\gamma$ positron is done scaling the coefficients according to the expected positron energy. In the $\mu^+ \to e^+\phi, \phi \to \gamma\gamma$ search analysis, positron energy is constant for a certain M_ϕ (Equation 3.1). Correction is done each time while scanning M_ϕ in the analysis.

3.5.5 Positron selection

To ensure the quality of positron reconstruction, we set several cuts for the positron selection. The positron selection criteria consist of basic track cuts, track fitting quality cuts, decay vertex cuts, DCH-TIC matching cuts, and ghost track cuts.

Basic track cuts

Basic track cuts examine the number of hits used for the Kalman filter tracking, which exclude abnormal tracks.

Track fitting quality cuts

Tracks with large uncertainties in momentum and direction evaluated from the Kalman filter are eliminated

Decay vertex cuts

Decay vertex cuts ensure the positron is from a muon which decays on the stopping target. If a event is originated from a muon decaying in the helium atmosphere, we can not identify the precise position of the decay vertex, which leads to large uncertainty in decay time and emission direction reconstruction of both positron and gamma-ray.

DCH-TIC matching

In the DCH-TIC matching cuts, we compare the hit position on TICP bar that is expected from Kalman filter tracking by drift chambers (DCH) and that is reconstructed by TICP PMT signals. In addition to this, we compare hit time of DCH and TICP. These cuts eliminates events with uncorrelated positrons for track and TICP hit, and events that positrons hardly scattered by some materials between DCH and TIC.

Ghost track cuts

In a high rate environment, sometimes different positrons hit the same DCH module at close in time and position. In such cases, different reconstructed trucks may share some hits for the trajectory reconstruction. On the other hand, sometimes tracking process recognize multi-turn events as different tracks. Ghost track cuts select the most probable track out of these tracks.

The selection criteria is the same as the case of $\mu^+ \to e^+\gamma$ analysis except energy selection. In $\mu^+ \to e^+\gamma$ search, positron momentum is equal to half the muon mass. In $\mu^+ \to e^+\phi, \phi \to \gamma\gamma$ search, positron momentum is expected to be lower and it depends on M_ϕ.

3.6 Reconstruction of two gamma-rays

The original MEG reconstruction tool kit offers pileup identification, but does not reconstruct each gamma-ray with good resolutions, so reconstruction dedicated to two gamma-rays is developed. Section 3.6.1 and 3.6.2 describes fundamental method used in two gamma-ray reconstruction. Section 3.6.3–3.7.3 describe reconstructions dedicated to $\mu^+ \to e^+\phi, \phi \to \gamma\gamma$ search.

3.6.1 Scintillation photons

The charge extracted from a PMT can be converted to the number of photo-electrons (N_{pe}) emitted when photons hit the photo-cathode by

$$N_{pe,i} = \mathcal{C} \times Q_i/(G_i \times \mathcal{C}_{CE,i} \times e). \tag{3.10}$$

Then, the number of the photons hitting the photo-cathode (N_{pho}) is reconstructed by

$$N_{pho,i} = N_{pe,i}/(\mathcal{C}_{QE,i}). \tag{3.11}$$

Here, i is the index number of the PMT, Q_i, G_i, $\mathcal{C}_{CE,i}$, and $\mathcal{C}_{QE,i}$ are charge, gain, collection efficiency, and quantum efficiency of the PMT respectively, $\mathcal{C}$ is an attenuation due to electronics, and e is the elementary electric charge.

3.6.2 Pileup identification

Pileup identification task searches the number of incident gamma-rays by looking for peaks in the light distribution observed by PMTs on inner and outer faces. Peaks in two dimensional histogram of N_{pho} which exceed a threshold are searched for each face. Threshold is set to be 200 photons. Details of the algorithm is described in Ref. [66]. The number of found peaks and the peak bins are obtained. interaction position in u,v plane can be known roughly with the resolution of bin width, here the distance between PMTs (= 6.2 cm for inner face). Then comparison of peak position is done to eliminate the same incident. The identification efficiency depends on the distance between two gamma-rays as shown in Figure 3.8. This figure is made using MC simulation with two gamma-rays generated on the muon stopping target with isotropic direction distribution. It is shown that the identification needs at least 3 bins ($\sim$ 20 cm), unless it fails.

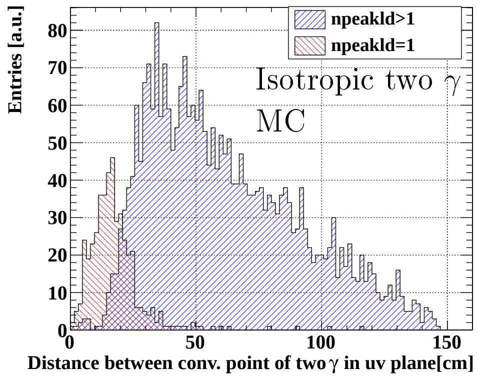

Figure 3.8: Distance between interaction positions of two gamma-rays in uv plane. Red histogram shows that for pileup search fails and blue shows that for pileup is identified.

3.6.3 Position reconstruction

PMT selection

PMT selection is done to minimize the fluctuation by the shower developing behind the first interaction point since we assume in the reconstruction the scintillation light comes from a point-like source. Interaction points of gamma-rays in u,v plane are roughly obtained by the pileup identification. Only the events in which pileup is found are processed. The nearest approximately 16 or 25 PMTs to the interaction position of each gamma-ray are selected from the inner face PMTs. When the interaction positions are close enough that the selected PMTs are overlapped, they are merged. Larger number of the used PMTs is applied for the case that the interaction position in w coordination is larger than 12 cm.

Then Precise three dimensional position is reconstructed by fitting the light distribution observed by inner face PMTs. The rough u,v positions are used as initial values in the reconstruction.

Reconstruction

The first interaction position and the expected number of photons by two gamma-rays ($\gamma 1, \gamma 2$), all in all 8 parameters ($3 \times 2 + 1 \times 2$) are fitted at the same time by minimizing

$$\chi^2_{position} = \sum_{i}^{nPMT} \frac{(N_{pho,i} - N_{pho,\gamma 1} \cdot \Omega_i(\vec{x}_{\gamma 1}) - N_{pho,\gamma 2} \cdot \Omega_i(\vec{x}_{\gamma 2}))^2}{\sigma(N_{pho,i})^2} . \tag{3.12}$$

Here, $N_{pho,i}$ is a measured value, $\sigma(N_{pho,i})$ is calculated using measured values, $\vec{x}_{\gamma}$ and $N_{pho,\gamma}$ are fitted values, and $\Omega_{iPMT}(\vec{x}_{\gamma})$ is calculated using fitted value. $nPMT$ is the number of the selected PMTs. $N_{pho,\gamma}$ is the expected number of photons generated by

$\gamma\,(=\gamma 1$ or $\gamma 2)$, $\vec{x}_\gamma$ is the first interaction position of γ, $\Omega_i(\vec{x}_\gamma)$ is the solid angle of photo-cathode of i-th PMT seen from γ interaction position and $\sigma(N_{pho,i})$ is statistical uncertainty of the number of photons seen by the PMT, which is calculated by

$$\begin{aligned}\sigma(N_{pho,i}) &= \frac{1}{\mathcal{C}_{QE,i}} \times \sigma_{pe,i}(N_{pe,i}) \\ &= \frac{1}{\mathcal{C}_{QE,i}} \times \sqrt{N_{pe,i}} \\ &= \sqrt{\frac{N_{pho,i}}{\mathcal{C}_{QE,i}}}\,.\end{aligned} \tag{3.13}$$

If initial value of $N_{pho,\gamma}$ is much apart from the actual value, position reconstruction in the direction of w can be mis-reconstructed. We perform position reconstruction again after energy reconstruction to use the reconstructed energy for the initial value of $N_{pho,\gamma}$ so as to improve reconstruction efficiency.

Then we perform correction on reconstructed position according to observed bias using MC simulation. Figure 3.9 shows bias in reconstructed position in w coordinate related to energy and reconstructed position. In $\mu^+ \to e^+\phi, \phi \to \gamma\gamma$ decay, gamma-ray energy and its emission angle have strong relation, so the correlation between energy and w may contain the effect by incident angel. The correlation with reconstructed position and energy are studied using $\mu^+ \to e^+\phi, \phi \to \gamma\gamma$ MC simulation and w is corrected.

Gamma-ray interaction positions are reconstructed in xyz coordinate, then they are converted into uvw coordinate system which is described in Section 2.1.1. Shift in u is corrected with 6.2 mm according to alignment calibration (Section 4.2.2). The resolution is expected to be approximately 5.5mm in u, v coordinate, and 6.5mm in w coordinate.

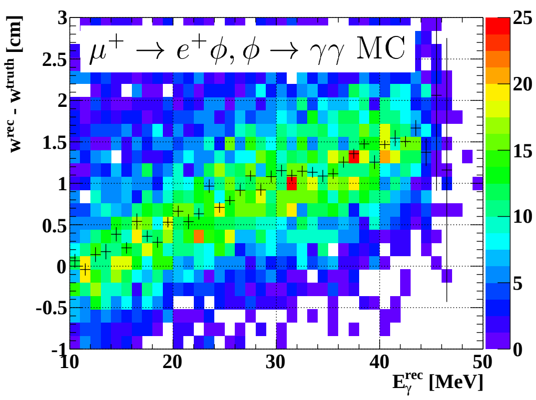

(a) Energy dependence of w reconstruction

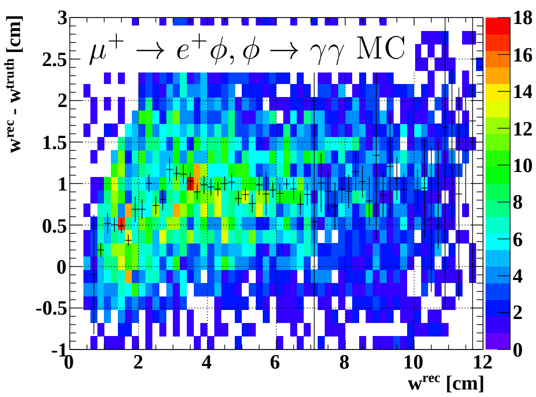

(b) Depth dependence of w reconstruction

Figure 3.9: Correlation between bias in w reconstruction and reconstructed energy, or reconstructed w.

3.6.4 Time reconstruction

PMT selection

Time measured by one PMT have not efficient resolution, so we fit interaction time using PMTs selected from all the faces of the detector. For the interaction time extraction of two gamma-rays, we first speculate which PMT have the information of the interaction time of which gamma-ray using the information obtained from the interaction position fit. We use the expected number of incoming photons to the PMT for the selection. Selection criteria are that,

- Expected number of photons by γ, $N_{pho,\gamma} \cdot \Omega_i(\vec{x}_\gamma)$ is more than 100,
- The ratio of the expected number of photons by γ and γ'; $(N_{pho,\gamma} \cdot \Omega_i(\vec{x}_\gamma))/(N_{pho,\gamma'} \cdot \Omega_i(\vec{x}_{\gamma'}))$ is more than 5,

where γ is the gamma-ray to be reconstructed, γ' is $N_{pho,\gamma}$ is the expected number of photons generated by γ obtained from the position fit and $\Omega_i(\vec{x}_\gamma)$ is the solid angle of i-th PMT from the reconstructed gamma-ray interaction position. The selection and the reconstruction is performed for each gamma-ray individually.

Reconstruction

Time measured by i-th PMT ($t_{PMT,i}$) and interaction time ($t_{hit,i,\gamma}$) of γ (= γ1 or γ2) is supposed to have following relation.

$$t_{hit,i,\gamma} = t_{PMT,i} - t_{delay,i,\gamma} - t_{offset,i} \tag{3.14}$$

Here, $t_{hit,i,\gamma}$ is the gamma-ray interaction time expected from i-th PMT. $t_{PMT,i}$ is the time of the PMT measured by the constant-fraction method described in Section 3.4.3, $t_{delay,i,\gamma}$ is time delay during the scintillation light propagation to the PMT in LXe and the delay caused by time walk, and $t_{offset,i}$ is a constant time offset of the readout channel of the PMT.

The delay time is estimated from the effective velocity of scintillation light in LXe, the number of photo-electron measured by the PMT, and the distance and the angle between the PMT photo-cathode and the gamma-ray interaction position. Calibration of $t_{delay,iPMT}$ is done using CEX data, and the detail is described in Ref. [67]. In the reconstruction for one gamma-ray, the estimation of the delay time includes effect of shower using averaged effective shower length of 52.8 MeV gamma-ray, but the length should be different according to energy of gamma-ray, so this component is not included in this study. The effect is supposed to be small because only PMTs that shower point is nearer than the first interaction position are affected and the difference is supposed to be small.

Then we define the χ^2_{time} for the time fit as follows.

$$\chi^2_{time} = \sum_{i}^{nPMT} \frac{(t_{hit,i,\gamma} - t_{LXe,\gamma})^2}{\sigma_{t,i}(N_{pe,\gamma})^2}, \tag{3.15}$$

where $N_{pe,\gamma}$ is the number of photoelectrons expected from the gamma-ray to be reconstructed. $\sigma_{t,i}(N_{pe,\gamma})^2$ corresponds to time resolution of each PMT, which is $1/\sqrt{N_{pe}}$

corrected with calibration result. PMT selection is done for each gamma-ray and the interaction time ($t_{LXe,\gamma}$) is reconstructed minimizing χ^2_{time} for each gamma-ray. During the fitting process, PMT selection is performed again removing PMTs whose time information differs from the reconstructed interaction time and the minimization is iterated.

In the analysis for one gamma-ray, correction by the sum of the photoelectron is performed, but the energy range is different in the analysis of $\mu^+ \to e^+\phi, \phi \to \gamma\gamma$ from that of $\mu^+ \to e^+\gamma$, and the calibration does not suit for the lower energy, so this correction is not performed in this study.

3.6.5 Energy reconstruction

In the reconstruction of energy, we first reconstruct the ratio of the number of photons emitted by two gamma-ray interactions. Fitting is performed minimizing the same χ^2 as position fit (Equation 3.12) fitting only $N_{pho,\gamma1}$, $N_{pho,\gamma2}$, fixing the interaction positions. Though we selected limited numbers of PMTs only from the inner face for the position fit, we select PMTs from all the faces for this fit removing PMTs with small output. During the fit, PMTs which cause large χ^2 are removed and the fitting is iterated.

After fitting the ratio of the number of photons, we divide reconstructed number of photons of each PMT to reconstruct the number of photons derived from each gamma-ray as follows,

$$N_{pho,i,\gamma} = \frac{N_{pho,\gamma} \cdot \Omega_i(\vec{x}_\gamma)}{N_{pho,\gamma} \cdot \Omega_i(\vec{x}_\gamma) + N_{pho,\gamma'} \cdot \Omega_i(\vec{x}_{\gamma'})} \times N_{pho,i}, \tag{3.16}$$

where $N_{pho,i,\gamma}$ is the number of photons induced by γ and $\Omega_i(\vec{x}_\gamma)$ is the solid angle of i-th PMT viewed from the reconstructed incident position of γ ($= \gamma1$ or $\gamma2$). When the solid angles of both gamma-rays are equal to 0, square of the distance between gamma-ray interaction position and PMT is used instead of the solid angle.

Then, the total number of photons emitted by each gamma-ray is reconstructed by,

$$\begin{aligned} N_{f,\gamma} &= \sum_i^{PMT\in f\text{th face}} w_i \times N_{pho,i,\gamma}, \\ N_{sum,\gamma} &= \sum_f^{\text{all faces}} w_f(u,v,w) \times N_{f,\gamma}, \end{aligned} \tag{3.17}$$

where f indicates inner, outer, lateral upstream, lateral downstream, top, or bottom face that PMTs are located, $N_{f,\gamma}$ is the total number of photons collected by PMTs in f-th face, w_i is a weight factor which is inverse of photo-cathode coverage of i-th PMT (see Figure 3.10), $w_f(u,v,w)$ is a weight factor to sum each face which is a function of the reconstructed interaction position of a gamma-ray, and $N_{sum,\gamma}$ is the total number of photons emitted by the interaction of γ. All the PMTs are used in the summation. $w_f(u,v,w)$ is optimized to make the energy resolution better using π^0-55 MeV peak data. We did not apply the technique of the face factor for the data taken in 2009, so $w_f = 1$ for the analysis of the 2009 data and the face factor technique is only applied to 2010 data in this thesis. Because $N_{sum,\gamma}$ calculated here have better resolution than the result of energy fit ($N_{pho,\gamma}$), we repeat this procedure from the division of the number of photons of each PMT replacing $N_{pho,\gamma}$ with $N_{sum,\gamma'}$ in Equation 3.16 and iterate.

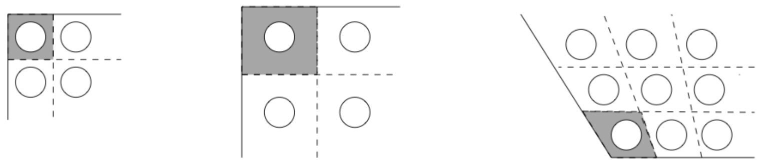

Figure 3.10: Photo-cathode coverage on different faces. From the left, inner, outer and top faces are shown. The circle is area of PMT photo-cathode and gray filled area is coverage of the PMT.

Then the energy of a gamma-ray is reconstructed by,

$$E_\gamma = F(u, v, w) \times T(t) \times C \times N_{sum,\gamma}, \tag{3.18}$$

where $F(u, v, w)$ a non-uniformity correction factor, $T(t)$ is a correction to compensate the change of light yield, and C is conversion factor from the number of photons to energy.

Non uniformity correction: $F(u, v, w)$

The LXe detector has non uniform response because scintillation photon collection efficiency depends on where the gamma-ray convert. Moreover, additional non-uniformity can be introduced in reality by several effects, such as deformation of detector, local bias of PMT calibration, and the face factors. Thus, we calibrate for the overall effects by scanning the real response of detector to calibration data over all acceptance. The non uniformity correction factor $F(u, v, w)$ is obtained using 17.6 MeV gamma-line from ${}^{7}_{3}\mathrm{Li}(\mathrm{p}, \gamma){}^{8}_{4}\mathrm{Be}$ reaction with help of π^0-55 MeV gamma-ray events.

Light yield: $T(t)$

Light yield is monitored with several calibration methods. In 2009 and 2010, the light yield was very stable, and the stability of 17.6 MeV gamma-line peak is 0.3 (0.2) % in RMS for 2009 (2010). Calibration with 17.6 MeV gamma-line is performed 2-3 times per week during the data taking period. Light yield correction factor $T(t)$ is prepared using 17.6 MeV gamma-line and cosmic ray data as well as π^0 data during the CEX runs. The possible errors in the correction are estimated and assigned to the energy scale uncertainty.

Conversion factor from the number of photons to energy: C

The linearity between N_{sum} and gamma energy E_γ was checked using gamma-ray with several energy available from our calibration methods. The conversion factor from N_{sum} to energy is given from calibration run using 55 MeV gamma-ray. Figure 3.11 shows the linearity of the detector checked with several calibration sources.

Resolution of the sum energy of two gamma-rays is estimated using MC simulation to be approximately 2 %, and the resolution of the ratio of the energy of two gamma-rays $(E_{\gamma 1}/(E_{\gamma 1} + E_{\gamma 2}))$ is 1.9×10^{-2} (here $E_{\gamma 1} > E_{\gamma 2}$). Then resolution of each gamma-ray energy is approximately 1 MeV.

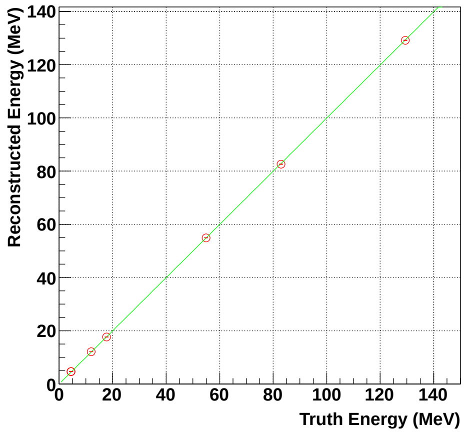

Figure 3.11: Linearity of reconstructed energy.

3.7 Combined analysis

3.7.1 ϕ decay vertex

ϕ decay vertex position is required to estimate momentum of gamma-rays and relative time between two gamma-rays or a positron and a gamma-ray. The decay vertex is reconstructed using the kinematics of $\mu^+ \to e^+\phi, \phi \to \gamma\gamma$ decay. Kinematics of the decay is described in Section 3.2. When M_ϕ is determined to a certain value, the decay kinematics is determined according to the equations described in the Section 3.2. ϕ decay vertex is reconstructed by using muon decay vertex position ($\vec{x}_{\mu\mathrm{decay}}$), opposite direction of positron ($\theta_{-\vec{dir}_{e^+}}, \varphi_{-\vec{dir}_{e^+}}$), and energy ($E_\gamma$) and position (u, v, w) of gamma-ray. The ϕ decay vertex position ($\vec{x}_{\mathrm{vtxfit}}$), and gamma-ray emission angles ($\varphi_\gamma, \vartheta_{\mathrm{rest}}$) are fitted using these measured values. $\vartheta_{\mathrm{rest}}$ is gamma-ray emission angle in the rest frame of ϕ, which is shown schematically in Figure 3.2 in Section 3.2. φ_γ is angle along the traveling direction of ϕ. Fitting is done minimizing χ^2 setting M_ϕ as a fixed parameter, and it is performed several times changing M_ϕ to a various values.

The χ^2 is defined as,

$$
\begin{aligned}
\chi^2_{\mathrm{vtxfit}} = & \sum_{\gamma=\gamma1,\gamma2} (E_\gamma - E_\gamma^{\mathrm{vtxfit}}(M_\phi, \vartheta_{\mathrm{rest}}))^2/\sigma^2_{E_\gamma} \\
& + (\theta_{-\vec{dir}_{e^+}} - \theta^{\mathrm{vtxfit}}_{\vec{dir}_\phi}(\vec{x}_{\mathrm{vtxfit}} - \vec{x}_{\mu\mathrm{decay}}))^2/\sigma^2_\theta \\
& + (\varphi_{-\vec{dir}_{e^+}} - \varphi^{\mathrm{vtxfit}}_{\vec{dir}_\phi}(\vec{x}_{\mathrm{vtxfit}} - \vec{x}_{\mu\mathrm{decay}}))^2/\sigma^2_\varphi \\
& + \sum_{\gamma=\gamma1,\gamma2} \sum_{X=u,v,w} (X_\gamma - X_\gamma^{\mathrm{vtxfit}}(\vec{x}_{\mathrm{vtxfit}}, \vartheta_{e\gamma}(M_\phi, \vartheta_{\mathrm{rest}}), \varphi_\gamma, r_\gamma))^2/\sigma^2_X.
\end{aligned}
\tag{3.19}
$$

Here, $E_\gamma^{\mathrm{vtxfit}}$, $\theta^{\mathrm{vtxfit}}_{\vec{dir}_\phi}$, $\varphi^{\mathrm{vtxfit}}_{\vec{dir}_\phi}$, and $X_\gamma^{\mathrm{vtxfit}}$ are values calculated using the fitting values. $E_\gamma^{\mathrm{vtxfit}}$ is expected gamma-ray energy calculated according to Equation 3.5, $\theta^{\mathrm{vtxfit}}_{\vec{dir}_\phi}$ and $\varphi^{\mathrm{vtxfit}}_{\vec{dir}_\phi}$ are angles of ϕ travel ($\vec{x}_{\mathrm{vtxfit}} - \vec{x}_{\mu\mathrm{decay}}$), r_γ is the distance that γ travels before the first interaction in the LXe detector which is set to be $|\vec{x}_\gamma - \vec{x}_{\mathrm{vtxfit}}|$, and $X_\gamma^{\mathrm{vtxfit}}$ is expected gamma-ray interaction position calculated from the $\mu^+ \to e^+\phi, \phi \to \gamma\gamma$ kinematics. Gamma emission angle relative to positron direction in the experimental frame ($\vartheta_{e\gamma}$) is calculated with M_ϕ and $\vartheta_{\mathrm{rest}}$ as described in Equation 3.6. Then gamma-ray interaction position can be calculated using $\vartheta_{e\gamma}$, the emission angle (φ_γ) along the axis of ϕ travel and the distance (r_γ) gamma-ray travels before the interaction in LXe. Then, χ^2_{vtxfit} is obtained by Equation 3.19 as a sum of position, energy difference of positron and gamma-rays with weight factors. These weight factors are determined taking resolutions of the detector into account. Because E_γ has asymmetric distribution, we assign different values on σ_{E_γ} according to sign of $E_\gamma - E_\gamma^{\mathrm{vtxfit}}$.

ϕ and e^+ are emitted coincident in time, and two gamma-rays are coincident, too. So it is possible to use time information in the fitting. However, this can make bias in the time structure of accidental backgrounds. We estimate the number of background events using time sidebands, which we will describe in the Section 5.2. The estimation of backgrounds fails if bias exists in the time structure, so we do not include time information in the χ^2 for the ϕ decay vertex fit.

3.7.2 Momentum reconstruction

Direction of gamma-rays are reconstructed connecting the reconstructed interaction position in the LXe detector and the reconstructed ϕ decay point.

$$\vec{n}_\gamma = (\vec{x}_\gamma - \vec{x}_{\mathrm{vtxfit}})/|\vec{x}_\gamma - \vec{x}_{\mathrm{vtxfit}}| \tag{3.20}$$

And we can estimate momentum of gamma-ray as,

$$\vec{P}_\gamma = E_\gamma \cdot \vec{n}_\gamma. \tag{3.21}$$

Using directions of gamma-rays, we can define following vectors,

$$\begin{aligned} \vec{n}_{perp} &= (\vec{P}_{\gamma 1} \times \vec{P}_{\gamma 2})/|\vec{P}_{\gamma 1} \times \vec{P}_{\gamma 2}|, \\ \vec{n}_{para} &= (\vec{P}_{\gamma 1} + \vec{P}_{\gamma 2})/|\vec{P}_{\gamma 1} + \vec{P}_{\gamma 2}|, \\ \vec{n}_{orth} &= \vec{n}_{perp} \times \vec{n}_{para}, \end{aligned} \tag{3.22}$$

where $\vec{n}_{perp}$ is a normal vector perpendicular to the plane which $\vec{n}_{\gamma 1}$ and $\vec{n}_{\gamma 2}$ makes, $\vec{n}_{para}$ is a direction parallel to the sum of momentum of two gamma-rays, and $\vec{n}_{orth}$ is a direction which is on the plane of $\vec{n}_{\gamma 1}$ and $\vec{n}_{\gamma 2}$ and orthogonal to $\vec{n}_{para}$.

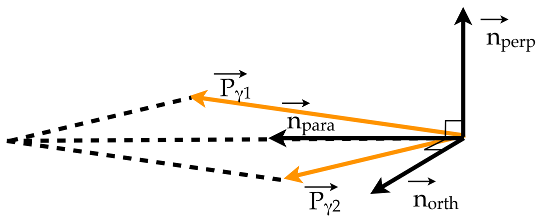

Figure 3.12: Coordination of direction for the sum of momentum.

Then the sum of the momentums of a positron and two gamma-rays and components in the direction defined in Equation 3.22 are estimated with

$$\begin{aligned} \vec{P}_{sum} &= \vec{P}_{e^+} + \vec{P}_{\gamma 1} + \vec{P}_{\gamma 2}, \\ P_{sum,perp} &= \vec{n}_{perp} \cdot \vec{P}_{sum}, \\ P_{sum,para} &= \vec{n}_{para} \cdot \vec{P}_{sum}, \\ P_{sum,orth} &= \vec{n}_{orth} \cdot \vec{P}_{sum}. \end{aligned} \tag{3.23}$$

P_{sum} should be zero for the signal $\mu^+ \to e^+\phi, \phi \to \gamma\gamma$ from the conservation of momentum. In the final state, all the tree particles are on one plane, and the reconstruction of $\vec{n}_{perp}$ does not depend much on the resolution of gamma-ray energies, so we can expect better resolution for $P_{sum,perp}$ than $P_{sum,para}$ and $P_{sum,orth}$.

3.7.3 Relative time

The time of flight of a gamma-ray and ϕ is estimated according to the expected M_ϕ as,

$$t_{tof,\gamma} = |\vec{x}_\gamma - \vec{x}_{\mathrm{vtxfit}}|/c + |\vec{x}_{\mathrm{vtxfit}} - \vec{x}_{\mu\mathrm{vtx}}|/(\beta_\phi \cdot c). \tag{3.24}$$

Then, relative time of reconstructed muon decay time is calculated by

$$\begin{aligned} \Delta t_{\gamma e^+} &= (t_{LXe,\gamma} - t_{tof,\gamma}) - t_{e^+} \\ \Delta t_{\gamma 1 \gamma 2} &= (t_{LXe,\gamma 1} - t_{tof,\gamma 1}) - (t_{LXe,\gamma 2} - t_{tof,\gamma 2}) \end{aligned} \tag{3.25}$$

Chapter 4

Detector performance and Monte Carlo simulation

In this chapter, the consistency of detector performance between Monte Carlo simulation and the actual detector is discussed.

We perform detector simulation with MEGMC and simulate waveform outputs of detectors with MEGBartender. The simulation program is carefully constructed to reproduce the actual detector, nevertheless there is small difference in resolutions between the simulation and the real detector. It is because we sometimes suffer trips of drift chamber HV and instability of muon beam, there might be some small misalignments or uncertainty of position in the actual detector, some of the optical properties of liquid xenon has uncertainties, and the noise situation cannot be perfectly reproduced in the simulation.

We use Monte Carlo simulation to estimate sensitivity for the $\mu^+ \to e^+\phi, \phi \to \gamma\gamma$ decay. We describe here how we smear the simulation data to make it consistent with the experimental data.

4.1 Positron spectrometer

4.1.1 Double turn method

In the MEG experiment there is no direct way to measure the positron resolutions, so we developed a method to evaluate them using tracks which make two turns inside the drift chamber. On average, each track makes 1.5 turns inside the spectrometer. In order to evaluate resolutions, we use tracks which make 2 turns inside the drift chambers.

When a positron makes 2 turns inside the drift chambers, we obtain hit clusters for each turn. We reconstruct each turn as an independent pseudo-track from each hit clusters. Each pseudo-track is then projected, after the first turn, to a fictitious plane on the beam line with the same inclination as the original target and the difference is used to measure resolutions. Energy, emission direction of positron and muon decay vertex resolutions can be obtained by this technique.

4.1.2 Smearing of positron spectrometer reconstruction

To reproduce the actual performance of the positron spectrometer with MC simulation, smearing of positron reconstruction is performed with two steps for MC simulation.

First, we randomly move interaction time and z position in each cells of drift chamber modules according to gaussian distribution. After this smearing, reconstruction of positron trajectory of MC simulation data come closer to the real data, but resolutions are still better in the case of MC simulation data.

Then the remaining small discrepancies are corrected by smearing the reconstructed position, energy and direction to be the same resolution as the case of the experiment. Comparison is done using $\mu^+ \to e^+\phi, \phi \to \gamma\gamma$ MC data of the case of $M_\phi = 25$MeV and experimental data of $\mu^+ \to e^+\nu_e\overline{\nu}_\mu$ positron with momentum between 49.87 ± 1MeV.

Smearing on hit reconstruction of drift chamber

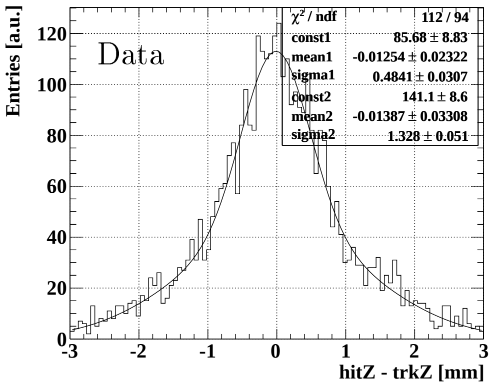

(a) Michel data with energy selection

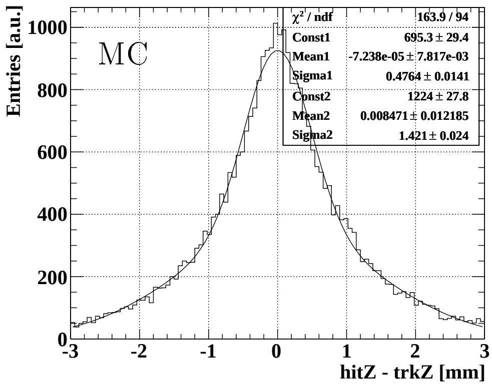

(b) $\mu^+ \to e^+\phi, \phi \to \gamma\gamma$ MC ($M_\phi = 25$ MeV)

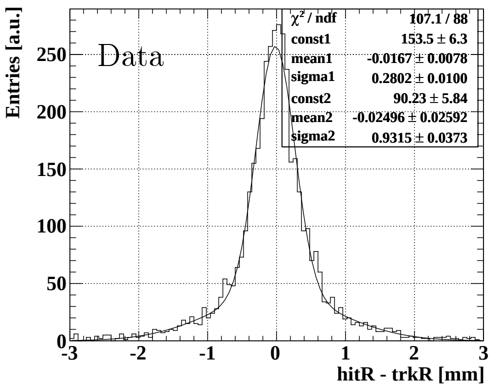

(c) Michel data with energy selection

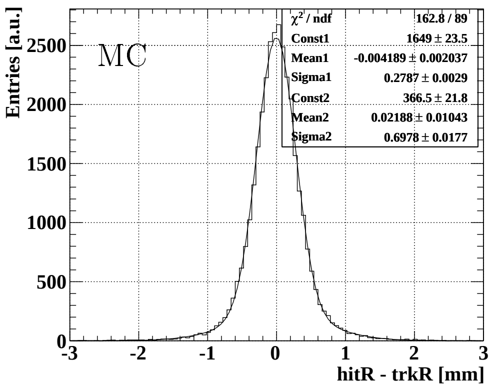

(d) $\mu^+ \to e^+\phi, \phi \to \gamma\gamma$ MC ($M_\phi = 25$ MeV)

Figure 4.1: Drift chamber hit position from hit reconstruction minus that from track fitting. Upper figures show those for Z position and lower show those for distance from sense wire. Right figures are from experimental Michel data, and left ones from MC simulation with hit reconstruction smearing. Solid curve shows double gaussian fit line.

Hit position resolution is estimated from the difference between hit position and track. Hit position in each cell of the drift chamber modules obtained from the fitted track have better resolution than that obtained by the hit reconstruction, so the difference between these roughly represents the hit resolution. The amount of smearing of z position and hit time are adjusted comparing this estimator with $\mu^+ \to e^+\phi, \phi \to \gamma\gamma$ MC simulation of the case of $M_\phi = 25\text{MeV}$ and experimental Michel data selecting positron energy between $49.87 \pm 1\text{MeV}$. The result is shown in Figure 4.1. Z position and hit time are smeared with $220\mu\text{m}$ and 7 ns respectively.

Smearing on reconstructed track

We estimate the amount of smearing needed to compensate remaining differences after the hit smearing from the resolutions estimated by double turn method. Figure 4.2 and 4.3 show double turn resolutions after hit smearing. Resolutions and its fitting errors of positron energy (E_e), positron emission angle (φ_e, θ_e), and muon decay vertex (radius from beam axis:R_e, distance in z direction:Z_e) are summarized in Table 4.1.

Difference of each resolution is used to smear reconstruction of MC simulation and fitting error is counted as systematic uncertainty.

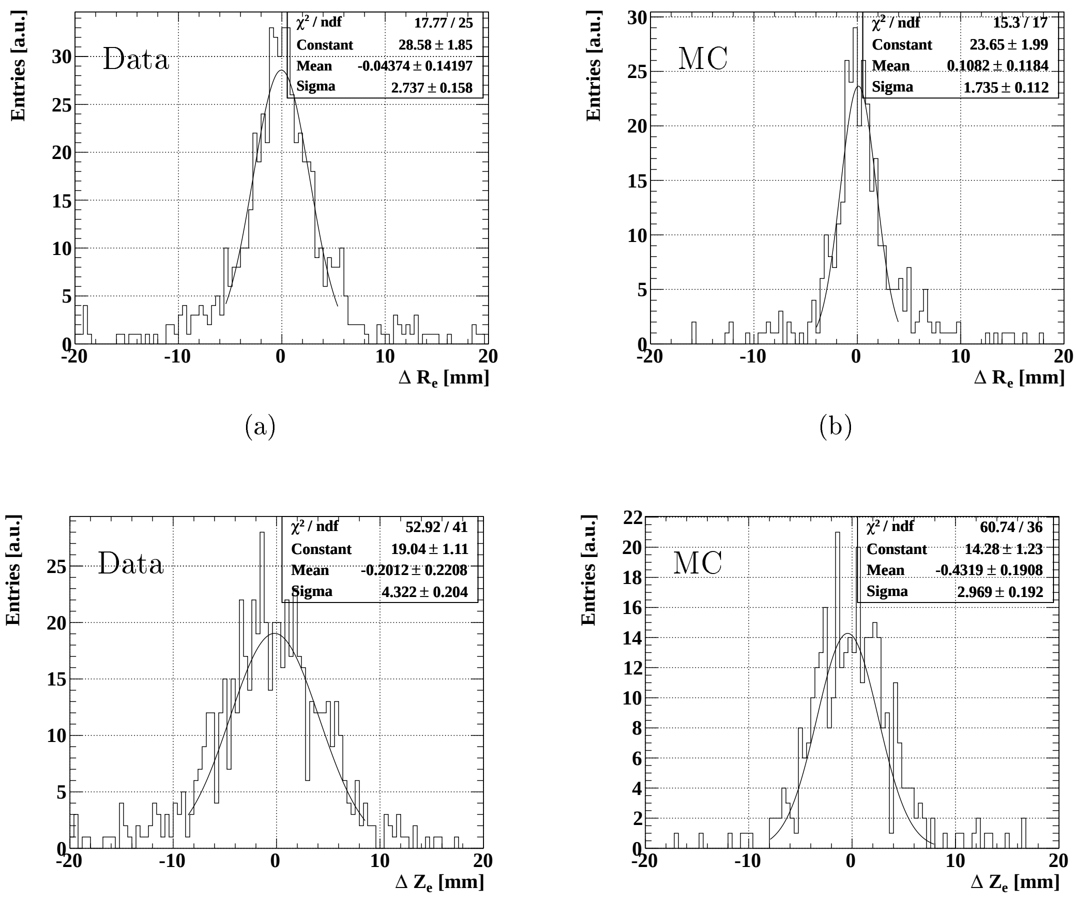

(a) (b) (c) (d)

Figure 4.2: Resolution of position on the stopping target plane obtained by double turn method. Distribution of the radius from the beam axis and that of z position are shown. Figure 4.2(a), 4.2(c) show these for experimental data of positrons with momentum between $49.87 \pm 1\text{MeV}$, and Figure 4.2(b), 4.2(d), 4.3(d) show these for $\mu^+ \to e^+\phi, \phi \to \gamma\gamma$ MC data of the case of $M_\phi = 25MeV$ after smearing of the hit reconstruction.

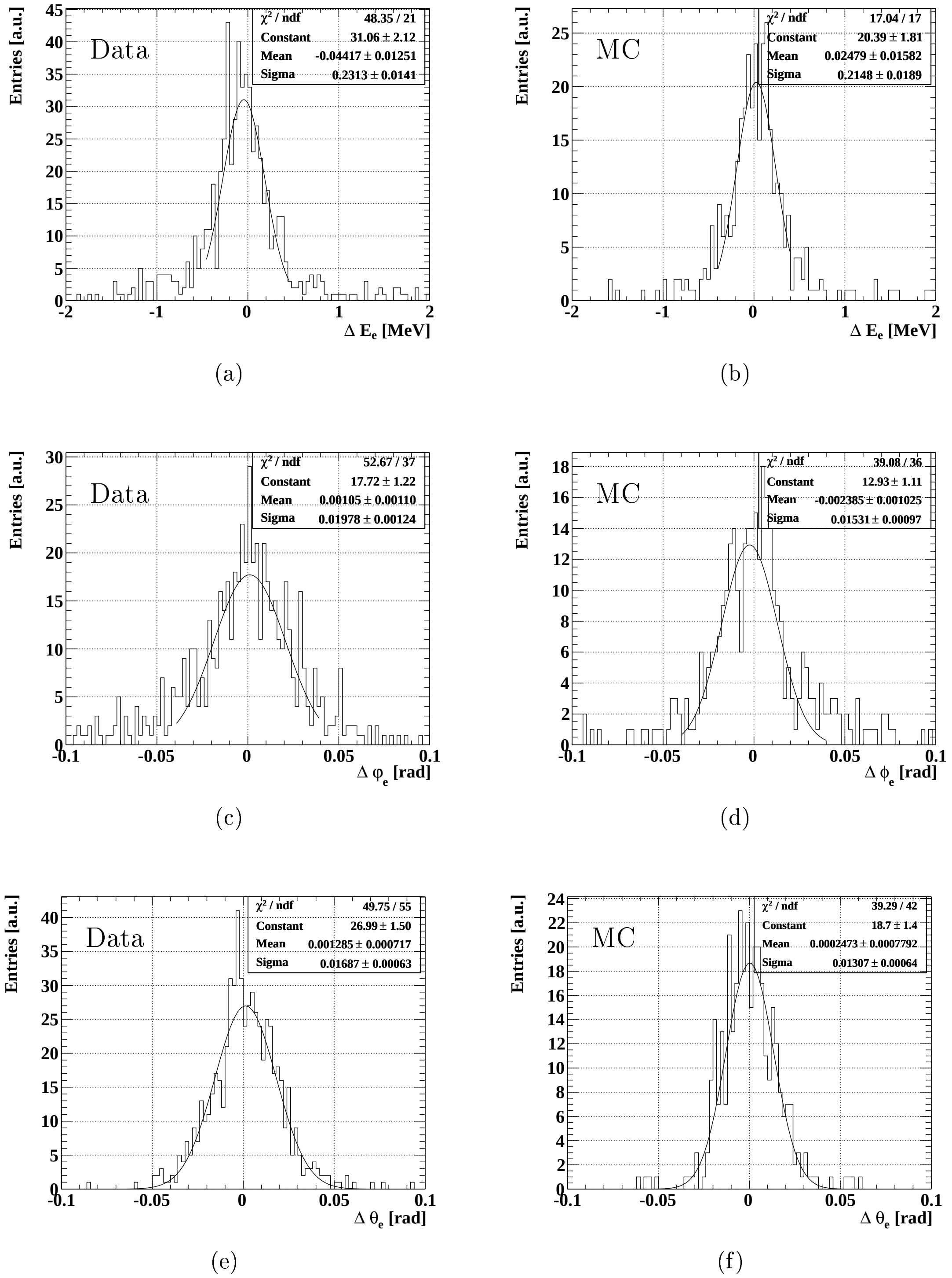

Figure 4.3: Energy (4.3(a), 4.3(b)), direction (4.3(c), 4.3(d), 4.3(e), 4.3(f)) resolutions obtained by double turn method. Figure 4.3(a), 4.3(e), 4.3(c) show these for experimental data of positrons with momentum between 49.87±1MeV, and Figure 4.3(b), 4.3(f), 4.3(d) show these for $\mu^+ \to e^+\phi, \phi \to \gamma\gamma$ MC data of the case of $M_\phi = 25MeV$ after smearing of the hit reconstruction.

Table 4.1: Double turn resolutions

	Data	MC	Difference	Uncertainty
σ_{E_e}(keV)	231 ± 14	215 ± 19	86	61
σ_{φ_e}(mrad)	19.8 ± 1.2	15.3 ± 1.0	12.5	2.3
σ_{θ_e}(mrad)	16.9 ± 0.6	13.1 ± 0.6	10.7	1.3
σ_{R_e}(mm)	2.7 ± 0.2	1.7 ± 0.1	2.1	0.2
σ_{Z_e}(mm)	4.3 ± 0.2	3.0 ± 0.2	3.1	0.3

4.2 Liquid xenon gamma-ray detector

In this section, we discuss about gamma-ray detector in MC simulation and experiment. We don't have proper calibration source for two gamma-ray reconstruction, so we can not estimate the resolution of it with experimental data. As basis of reconstruction algorithm for two gamma-ray is the same as that for one gamma-ray, we compare resolution of one gamma-ray reconstruction between experimental data and MC simulation, and obtained difference is used for smearing the resolution of two gamma-ray. Pseudo two gamma-ray events are generated superposing photon distribution of Li gamma-ray calibration data (Section 2.5.3). Difference between one gamma-ray reconstruction and two gamma-ray reconstruction was compared and the obtained difference is assigned as systematic uncertainty.

4.2.1 Detector efficiency

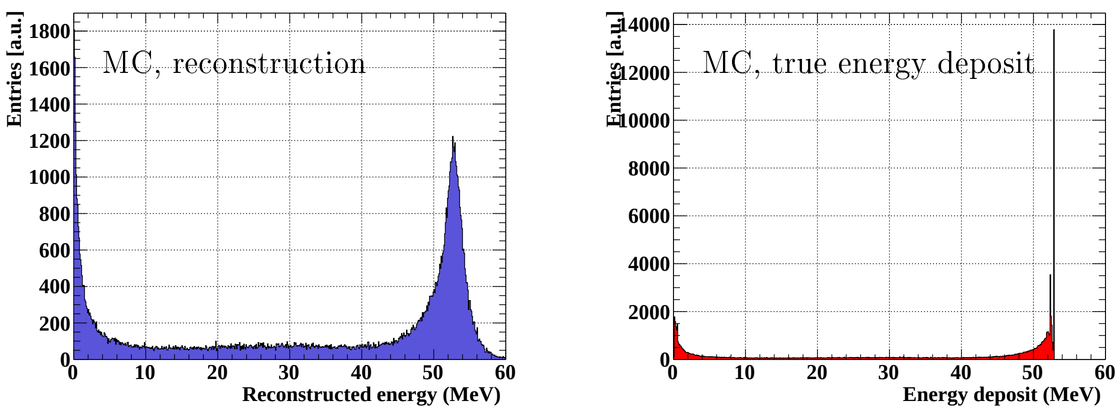

(a) Reconstructed energy.

(b) Distribution of the energy deposit in LXe.

Figure 4.4: Distribution of energy for 52.8 MeV gamma-ray MC simulation.

Figure 4.4 shows distributions of reconstructed energy and MC truth energy deposit in LXe. Figure 4.5 shows distribution of gamma-ray first conversion point. These three figures are obtained using 52.8 MeV gamma-ray MC simulation.

Gamma-ray passes through COBRA magnet, honeycomb window, inner face PMT. Lower tail of the energy histogram is mainly due to energy loss by interactions before entering the detector active volume, or shower escape in case that gamma-ray interact close to the detector face.

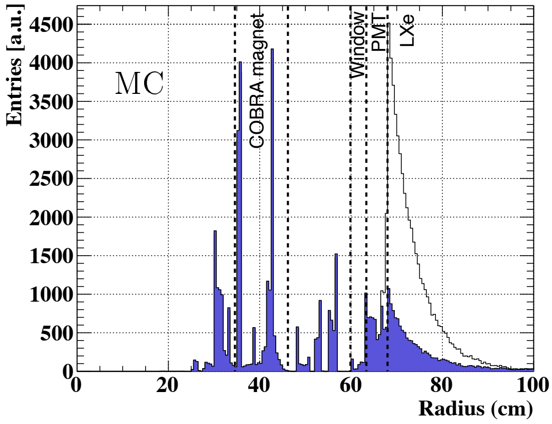

Figure 4.5: Distance from beam axis to gamma-ray first conversion point. Blue filled: energy deposit in LXe < 48 MeV. blank: all events.

Gamma-ray detector efficiency agrees well with experiment and MC simulation. When we define the efficiency to be the probability that reconstructed energy of 52.8 MeV gamma-ray is larger than 48 MeV, it is estimated to be 65 % from MC simulation and 64-67 % from experimental data.

4.2.2 Energy and position resolution

Energy and position resolutions of the LXe detector are estimated using calibration data of 55 MeV gamma-ray from π^- charge exchange reaction (Section 2.5.4). Difference between experimental data and MC simulation is estimated, and the obtained values are used to reproduce the actual detector resolution by MC simulation.

Energy

Energy resolution is studied using 55 MeV gamma-ray. Study on MC simulation with the same situation shows that gaussian smearing on the reconstructed energy randomly with 1.15% reproduces the resolution by experimental data. As the total energy of two gamma-rays with the $\mu^+ \to e^+\phi, \phi \to \gamma\gamma$ decay is about the same, and the same amount of smearing on the total energy is adopted for MC simulation.

Uncertainty of the energy scale in the experiment is estimated with several calibration data. We monitor light yield of LXe using cosmic ray muon and 17.6 MeV gamma-ray from Li nuclear reaction (Section 2.5.3). Gain is monitored using LED. Huge number of 17.6 MeV gamma-ray data gives dependence of reconstructed energy on interaction position. Combining the result of gain and light yield monitoring, dependence on interaction position, and statistical uncertainty of fitting, we assign 0.33 % to the energy scale uncertainty.

Position

Position reconstruction is studied using 55 MeV gamma-ray and putting lead collimator in front of the entrance window of the detector. Shape of the collimator used in 2008 run is shown in Figure 4.6. Three slits parallel to the u direction are formed on the collimator.

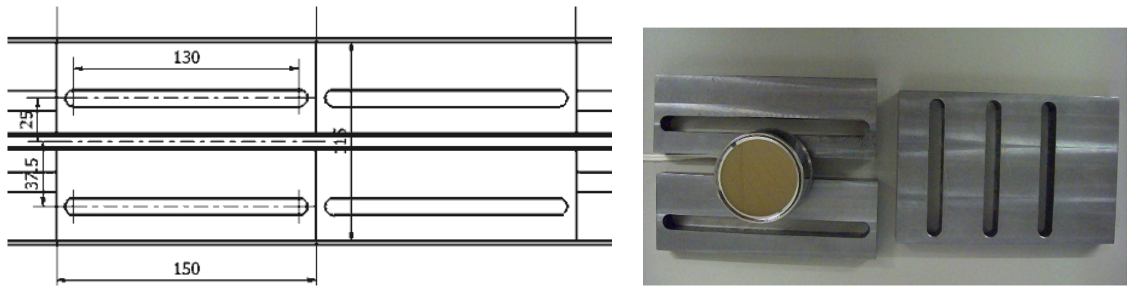

(a) Design of lead collimator. Width of slit is 1 cm. Thickness is 1.8 cm.

(b) Picture of lead collimator. A 2-inch PMT is put for a reference of size.

Figure 4.6: Lead collimator

Distribution of reconstructed position in v direction is shown in Figure 4.7(a). That for the same setting with MC simulation is shown in Figure 4.7(b). Gamma-rays which pass through slits of the collimator make three peaks. Fitted sigma of each peak is compared between experimental data and MC simulation, and the difference is estimated to be 1.8 mm. Reconstructed position with $\mu^+ \to e^+\phi, \phi \to \gamma\gamma$ MC simulation is smeared randomly with gaussian distribution with width of 1.8 mm.

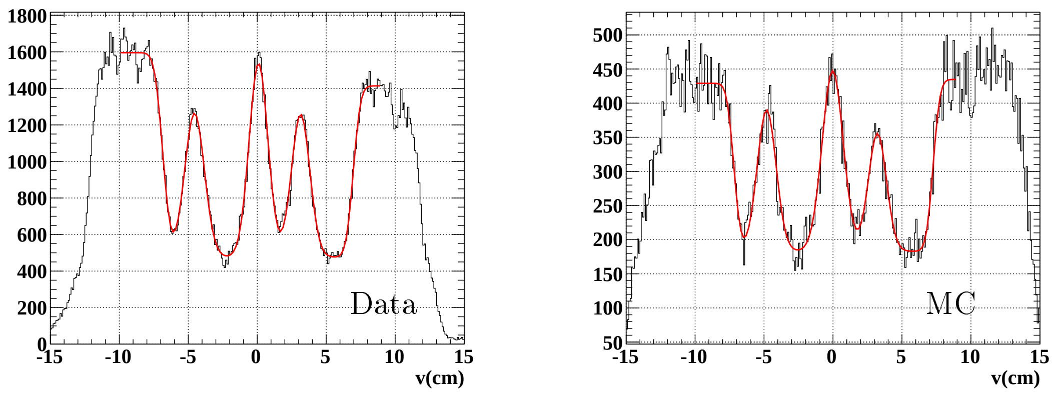

(a) Data in 2008 run

(b) MC

Figure 4.7: Distribution of reconstructed position in lead collimator run. Red line shows fit curve.

Alignment

We measured the LXe detector alignment with three ways.

One is a measurement of cosmic ray. The trajectory of high energy cosmic ray is approximately straight when the magnets are turned off. Reconstructing the trajectory of cosmic ray which penetrates both the LXe detector and the drift chambers gives relative alignment information.

Second measurement is done placing lead cubes in front of gamma ray entrance window using 17.6 MeV gamma-line from Li nuclear reaction (Section 2.5.3). Lead cubes make shadows in reconstructed gamma-ray incident position. Comparison of the positions of lead cubes and the shadows gives absolute position information.

Third measurement is done placing AmBe 4.4 MeV gamma-ray source in front of gamma-ray entrance window. We compare the placed position and reconstructed gamma-ray position.

We combined the results of these three measurements and evaluated the LXe detector alignment to be $\Delta z = -6.2 \pm 2.3$(mm).

In this thesis, the LXe detector is placed 6.2 mm shifted position in the event generation of MC simulation. 2.3 mm is treated as systematic uncertainty in z.

Two gamma-ray reconstruction

As we do not have suitable two gamma-ray calibration data, performance of two gamma-ray reconstruction is examined by making pseudo two gamma-ray events from two sets of one gamma-ray data. As shown in Figure 2.31 in Section 2.5.3, Li gamma-ray spectrum have 17.6 MeV gamma-line and broad 14.7 MeV gamma-ray, which are a bit small but near to the energy of $\mu^+ \to e^+\phi, \phi \to \gamma\gamma$ gamma-ray. Pseudo two gamma-ray events are made superposing photon distributions from two sets of Li gamma-ray data. One example is shown in Figure 4.8

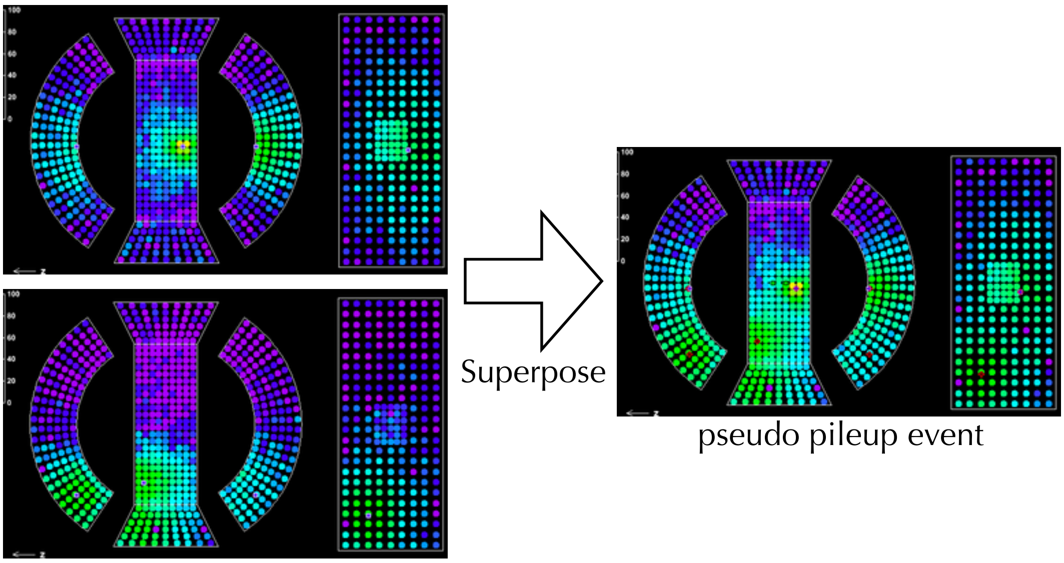

Figure 4.8: Pseudo pileup event generation.

Ordinary one gamma-ray reconstruction used for $\mu^+ \to e^+\gamma$ search is applied before mixing. Performance of one gamma-ray reconstruction is confirmed with several calibrations, and the result of two gamma-ray reconstruction after the mix is compered with the reconstruction done before the mix. In this way, effect of noise is also accumulated, so the resolution is supposed to become worse than the actual resolution. The result is shown in Table 4.2. Here, EnergyRatio is defined as $E_{\gamma 1}/(E_{\gamma 1} + E_{\gamma 2}), (E_{\gamma 1} > E_{\gamma 2})$. Because the sum of the energies of two gamma-rays is almost the same as the total number of observed photons, it is thought to have good resolution. Loss of energy resolution stems in the separation of energies, so we compare the resolution of separation here. It is shown that two gamma-ray reconstruction on pseudo pileup event reproduces one gamma-ray reconstruction applied before the mix. One big difference is that shift of mean of w is seen with data. This is probably because of insufficient knowledge on optical property of the detector, for example dependence of PMT Q.E. on incident angle of incoming scintillation photon. Quadratic difference between the result of data and MC simulation is counted as systematic uncertainty. This difference should be bigger than the true value because of accumulation of noise.

Table 4.2: Difference between one and two gamma-ray reconstruction

	Data	MC
$\sigma_{\Delta\mathrm{EnergyRatio}}(\%)$	2.3 ± 0.1	2.0 ± 0.1
$\sigma_{\Delta u1}(\mathrm{mm})$	0.78 ± 0.03	0.63 ± 0.04
$\sigma_{\Delta u2}(\mathrm{mm})$	0.74 ± 0.03	0.59 ± 0.04
$\sigma_{\Delta v1}(\mathrm{mm})$	0.77 ± 0.03	0.60 ± 0.03
$\sigma_{\Delta v2}(\mathrm{mm})$	0.64 ± 0.02	0.63 ± 0.04
$\sigma_{\Delta w1}(\mathrm{mm})$	2.5 ± 0.1	2.2 ± 0.1
$\sigma_{\Delta w2}(\mathrm{mm})$	2.2 ± 0.1	2.4 ± 0.1
$\mu_{\Delta w1}(\mathrm{mm})$	1.69 ± 0.07	0.45 ± 0.09
$\mu_{\Delta w2}(\mathrm{mm})$	1.28 ± 0.06	0.61 ± 0.11

Table 4.3: Systematic uncertainty in two gamma-ray reconstruction

	Systematic uncertainty
Energy Scale(%)	0.33
Energy Ratio(%)	1.1
σ_u, σ_v (mm)	0.5
σ_w (mm)	1.2
μ_w (mm)	1.6

4.3 Time reconstruction

Table 4.4: Time resolution

	2009	2010	MC
σ_{t_γ} (ps)	96	67	61
$\sigma_{t_{e\gamma}}$ (ps)	146	122	94

Table 4.5: Time smearing

	for 2009	for 2010
Smearing on t_γ (ps)	74	28
Smearing on t_e (ps)	84	73

Table 4.4 shows time resolution of the LXe detector and positron gamma relative time resolution estimated from the data taken in 2009, 2010 and $\mu^+ \to e^+\gamma$ MC. The difference between MC simulation and the experiment is calculated and the result is summarized in Table 4.5. Amount of smearing on gamma-ray time reconstruction needed to adjust time resolution of MC events is estimated from the difference of σ_{t_γ}. Then the smearing factor for positron reconstruction for MC is is estimated from the difference of $\sigma_{e\gamma}$ taking the smearing factor of LXe detector into account.

Time reconstruction for two gamma-rays is based on the same algorithm as the reconstruction for one gamma-ray except for the PMT selection criteria and energy range of reconstructed gamma-ray, so we can expect that smearing factors for one gamma-ray work also for two gamma-ray reconstruction. As calibration for time reconstruction of gamma-ray is made by π^0-55 MeV gamma-ray to suit for the analysis of $\mu^+ \to e^+\gamma$ decay, we observe shift of mean in the time reconstruction of gamma-ray with low energy. Calibration for MC is also made in the same procedure using 55 MeV MC simulation data.

As we do not have proper calibration data for two gamma-ray time reconstruction, we can not compare difference between one gamma-ray reconstruction and two gamma-ray reconstruction with experimental data. Superposing light distribution of two sets of one gamma-ray events do not work on time reconstruction, and we need to go back to waveform analysis. But the superposition of waveforms of experimental data is not developed yet. Systematic uncertainty is set to be 150 ps ($\sim 2 \times smearing$) for mean and sigma of time reconstruction for a conservative estimation.

Table 4.6: Systematic uncertainty in time

$\mu_{t_{e\gamma}}$ (ps)	150
$\sigma_{t_{e\gamma}}$ (ps)	150

Part IV

Analysis

Chapter 5

ϕ-mediated decay search analysis

This chapter presents the analysis of searching for lepton flavor violating decay mediated by a (pseudo-)scalar particle ϕ. We use data pre-selected for $\mu^+ \to e^+\gamma$ search taken in 2009 and 2010. The analysis is based on a simple cut analysis. The pre-selection and the signal selection cuts are described in Section 5.1. We estimate the number of background events in Section 5.2 and that of observed in the signal region in Section 5.3. Normalization is discussed in Section 5.4. Bounds on the branching ratio are shown in Section 5.5.

5.1 Signal event selection

The first processing is done just after the physics data is taken. Then preselection is performed to reduce data size for more precise analysis with the second processing. The preselection criteria for $\mu^+ \to e^+\gamma$ search are defined as,

i) $-6.875\,\mathrm{ns} < t_\gamma - t_{TICHIT} < 4.375\,\mathrm{ns}$,

ii) $|t_{track} - t_{TICHIT}| < 50\,\mathrm{ns}$,

where t_γ is the reconstructed gamma emission time with an assumption that one gamma-ray is coming from the origin, and t_{TICHIT} is TICP (timing ϕ counter) hit timing without subtraction of the time of flight Thus we did not use precise tracking information for the preselection. The reason of the asymmetric window for preselection i) is to acquire the multi-turn events; because of the absence of the tracking, we do not know the number of turns before the hit on the timing counter. The second criterion requires at least one track associated with the trigger is found. With this preselection, the data size is reduced by a factor about 0.3-0.4. The selected events are reprocessed when the calibration or the reconstruction algorithm is updated.

We use this preselected data to search for the ϕ-mediated decay. In addition to this criteria, another pre-selection dedicated to the $\mu^+ \to e^+\phi, \phi \to \gamma\gamma$ search is applied subsequently. This selection criteria are defined as follows,

- $npeakld > 1$,
- At least one good positron track,
- $|E_{\gamma normal} + E_{e^+} - M_\mu| < M_\mu \times 20\%$,

- $E_{\gamma normal} > 40\,\mathrm{MeV}$,

where *npeakld* is the number of peaks found by pileup identification on the LXe detector (Section 3.6.2), good positron is a positron track passing MEG positron selection criteria (Section 3.5.5) except the energy selection, and $E_{\gamma normal}$ is a reconstructed total energy deposit in the LXe detector without unfolding pileup.

After these preselection, second processing is done to perform reconstructions dedicated to $\mu^+ \to e^+\phi, \phi \to \gamma\gamma$ search. Then analysis cuts are applied to select signal events and eliminate background events. The definition of the cut is as follows.

Gamma-ray acceptance

- $|u_\gamma| < 25\mathrm{cm} \wedge |v_\gamma| < 71\mathrm{cm}$ for each gamma-rays

Cut for pileup identification

- $\sqrt{(u_{\gamma 1} - u_{\gamma 2})^2 + (v_{\gamma 1} - v_{\gamma 2})^2} > 20\mathrm{cm}$

Energy selection

- $|E_{\gamma 1} + E_{\gamma 2} + E_{e^+} - M_\mu| < M_\mu \times 10\%$
- $E_{\gamma 1} > 10\mathrm{MeV}$, $E_{\gamma 2} > 10\mathrm{MeV}$
- $|P_{e^+} - P_\phi| < 1\mathrm{MeV}$

Time selection

- $|t_{\gamma 1 e^+} - 0.1\mathrm{ns}| < 0.5\mathrm{ns}$ $(E_{\gamma 1} > E_{\gamma 2})$
- $|t_{\gamma 1 \gamma 2}| < 0.5\mathrm{ns}$

Certification for the quality of ϕ decay vertex fit

- $-4\mathrm{MeV} < E_\gamma - E_\gamma^{\mathrm{vtxfit}}(M_\phi, \vartheta_{\mathrm{rest}}) < 2\mathrm{MeV}$ for $\gamma = \gamma 1, \gamma 2$
- $|\theta_{-\overrightarrow{dir}_{e^+}} - \theta^{\mathrm{vtxfit}}_{\overrightarrow{dir}_\phi}| < 30\mathrm{mrad}$
- $|\varphi_{-\overrightarrow{dir}_{e^+}} - \varphi^{\mathrm{vtxfit}}_{\overrightarrow{dir}_\phi}| < 30\mathrm{mrad}$
- $\sqrt{(u_\gamma - u_\gamma^{\mathrm{vtxfit}})^2 + (v_\gamma - v_\gamma^{\mathrm{vtxfit}})^2} < 2$ cm for $\gamma = \gamma 1, \gamma 2$
- $|w_\gamma - w_\gamma^{\mathrm{vtxfit}}| < 1$ cm for $\gamma = \gamma 1, \gamma 2$

Momentum conservation

- $|P_{sum,perp}| < 1.5\mathrm{MeV}$
- $-5\mathrm{MeV} < P_{sum,para} < 2\mathrm{MeV}$
- $|P_{sum,orth}| < 3\mathrm{MeV}$

The acceptance region is based on interval of inner face PMTs, which excludes a half size of PMT interval around edges of u and v. Position reconstruction is done using PMTs only on the inner face, so the resolution become worse at the edge. Energy resolution also become worse at the edge because of higher probability of shower escape. Acceptance region is determined to exclude such events.

Pileup search fails when the distance between incident positions of two gamma-rays in u,v is smaller than 20 cm which corresponds to approximately three times PMT intervals as mentioned in Section 3.6.2. Figure 5.1 shows the distribution of this distance in u,v.

We observe decay of stopped muon, so the sum of the energies of the final three particles should be the same as the muon mass, and the momentum of the positron should be the same as that of ϕ. Events with either gamma-ray with reconstructed energy less than 10 MeV are eliminated because we have more backgrounds in the lower energy region. Efficiency of reconstruction is also affected in the low energy region. These cuts and the distributions of the estimator are shown in Figure 5.2, 5.3, and 5.4.

A example of time structure of B.G. and signal is shown in Figure 5.5. There is a small shift about 100 psec in gamma-ray time reconstruction. This is because calibration of time reconstruction for gamma-ray with low energy is not prepared and gamma-ray position correction with incident angle is not performed. So the cut for $t_{\gamma 1 e^+}$ is set to be shifted. Main B.G. is the events that two gamma-rays coming approximately the same in time and one positron overlap in time accidentally. Distribution of time difference of two gamma-rays is broader for B.G. events than the signal.

Distributions of estimators for the cuts to certify the quality of ϕ decay vertex fit and cut for for momentum conservation are shown in Figure 5.6–5.9 together with the cut region shown with red lines. Definition of the estimator of the ϕ decay vertex fit is the same as discussed in Section 3.7.1. Coordination of the momentum sum vector is defined in Section 3.7.2. Cut region is determined taking resolutions and B.G. distributions into account. For example, gamma-ray energy cut is set to be stricter compared to the other estimators so as to eliminate the B.G. events.

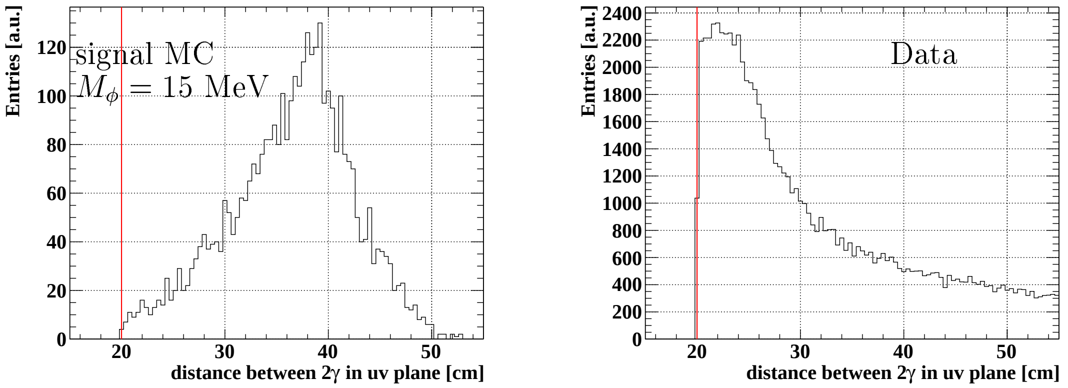

(a) $\sqrt{(u_{\gamma 1} - u_{\gamma 2})^2 + (v_{\gamma 1} - v_{\gamma 2})^2}$ distribution of signal by MC

(b) $\sqrt{(u_{\gamma 1} - u_{\gamma 2})^2 + (v_{\gamma 1} - v_{\gamma 2})^2}$ distribution of data

Figure 5.1: Distribution of $\sqrt{(u_{\gamma 1} - u_{\gamma 2})^2 + (v_{\gamma 1} - v_{\gamma 2})^2}$. Distribution of this for signal events depends on M_ϕ. When M_ϕ is light, peak position comes closer to 0. Preselection, acceptance cut, energy sum cut, and gamma-ray energy cut are applied. Red line shows cut line.

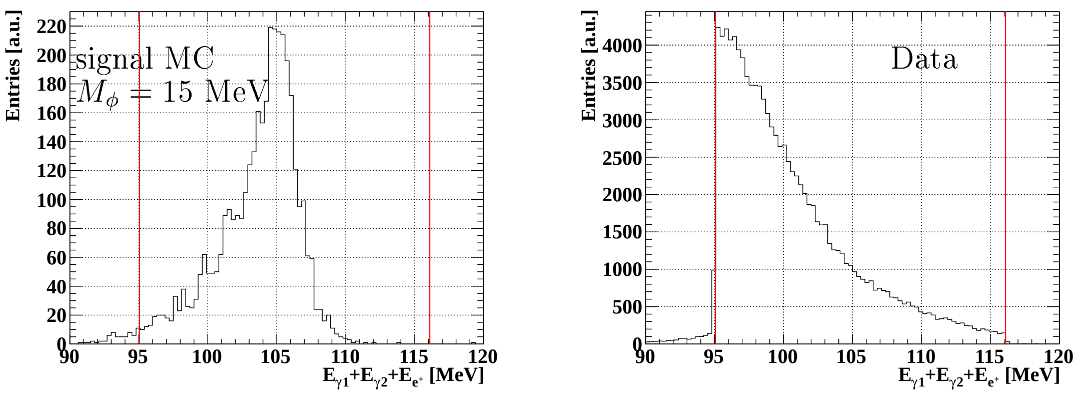

(a) Distribution for energy sum of signal by MC

(b) Distribution for energy sum of data

Figure 5.2: Distribution of energy sum of three particles. Preselection, acceptance cut, energy sum cut, and gamma-ray energy cut are applied. Small tail outside the cut region is made by a pileup positron. Red line shows cut region.

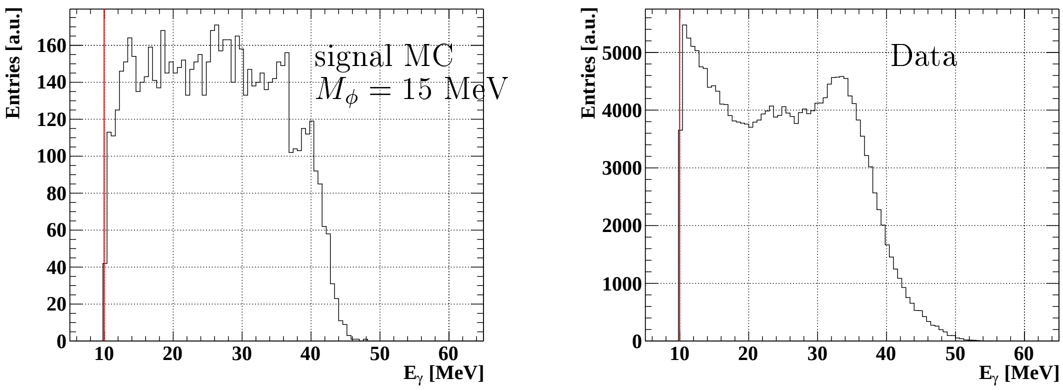

(a) Distribution of E_γ of signal by MC

(b) Distribution for E_γ of data

Figure 5.3: Distribution of energy of a gamma-ray. Preselection, acceptance cut, energy sum cut, and gamma-ray energy cut are applied. Red line shows cut line.

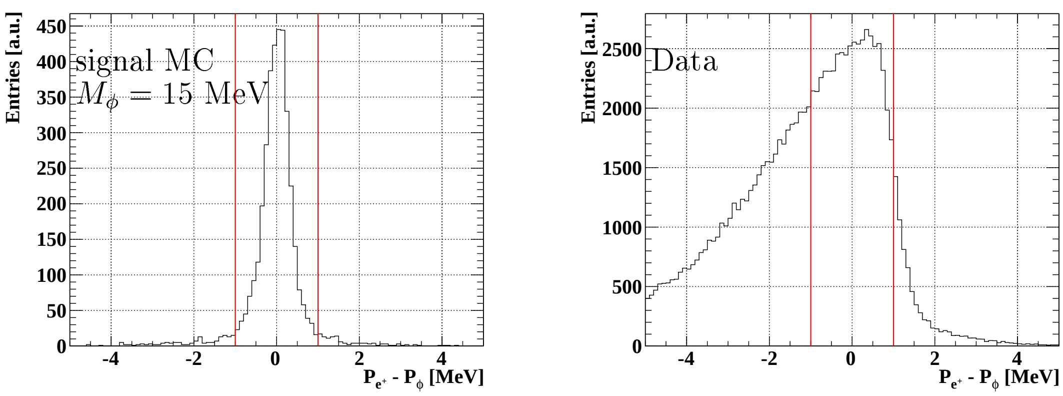

(a) Distribution for $P_{e+} - P_\phi$ of signal by MC

(b) Distribution for $P_{e+} - P_\phi$ of data

Figure 5.4: Distribution of difference of gamma-ray energy between reconstructed and that from ϕ decay vertex fit. P_ϕ is calculated expecting M_ϕ to be 15 MeV for both data and MC. Preselection, acceptance cut, energy sum cut, and gamma-ray energy cut are applied. Red line shows cut region.

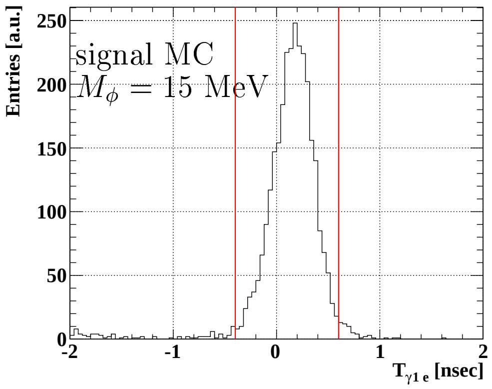

(a) Distribution for $t_{\gamma 1 e}$ of signal by MC

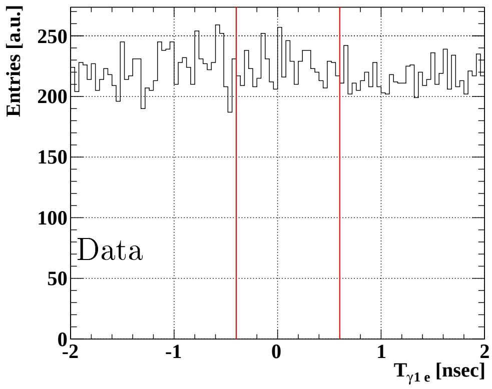

(b) Distribution for $t_{\gamma 1 e}$ of data

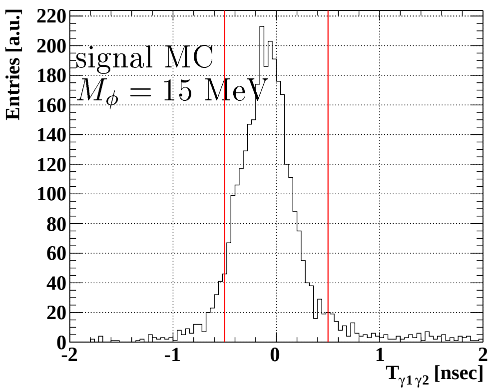

(c) Distribution for $t_{\gamma 1 \gamma 2}$ of signal by MC

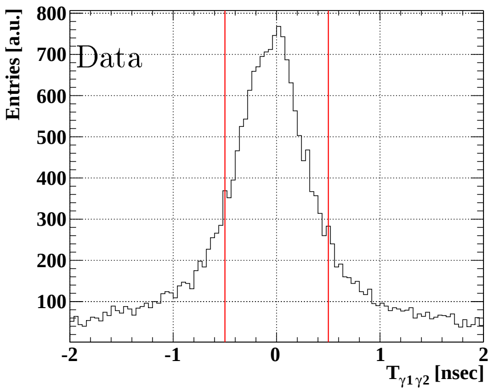

(d) Distribution for $t_{\gamma 1 \gamma 2}$ of data

Figure 5.5: Distribution of relative times. Vertex fit is done expecting M_ϕ to be 15 MeV for both data and MC. Preselection, acceptance cut, energy sum cut, and gamma-ray energy cut are applied. Red line shows cut region.

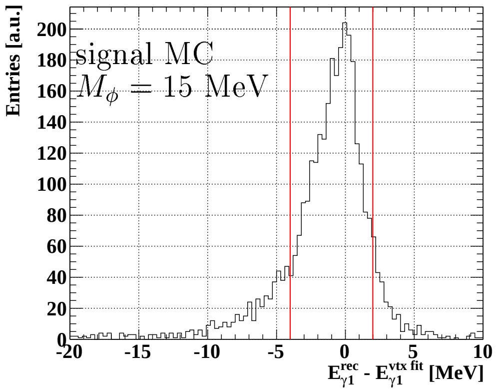

(a) Distribution for $E_{\gamma 1}$ of signal by MC

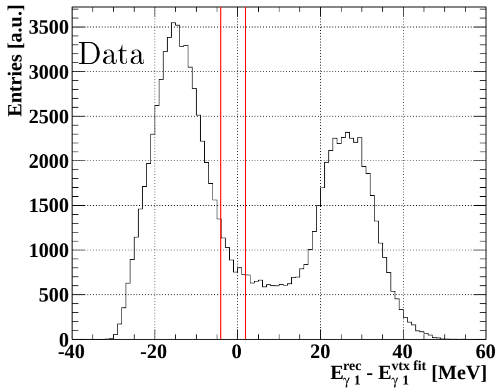

(b) Distribution for $E_{\gamma 1}$ of data

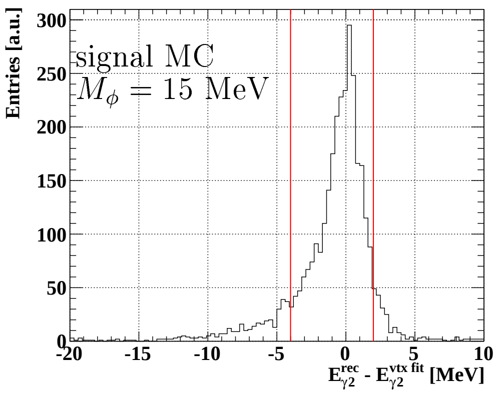

(c) Distribution for $E_{\gamma 2}$ of signal by MC

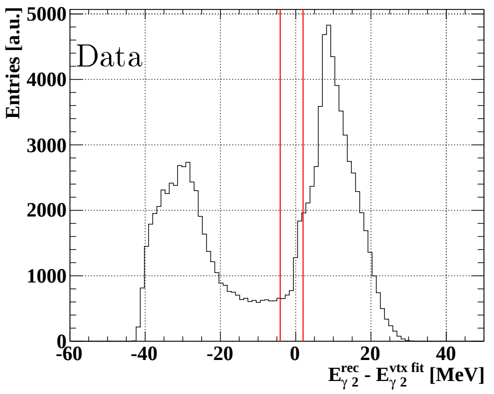

(d) Distribution for $E_{\gamma 2}$ of data

Figure 5.6: Distribution of difference of gamma-ray energy between reconstructed and that from ϕ decay vertex fit. Vertex fit is done expecting M_ϕ to be 15 MeV. Red line shows cut region. Preselection, acceptance cut, energy sum cut, and gamma-ray energy cut are applied. Original distribution of gamma-ray energy of the background is a broad one peak distribution, and that of signal is narrower, so the difference of them makes two peaks.

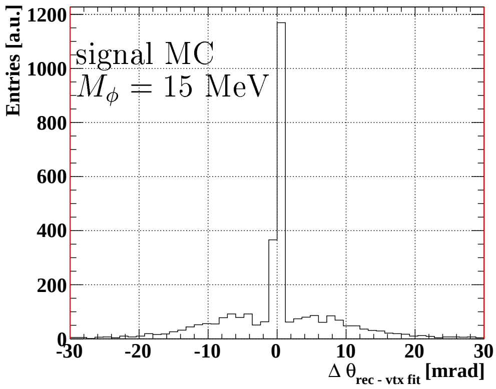

(a) Distribution for θ of signal by MC

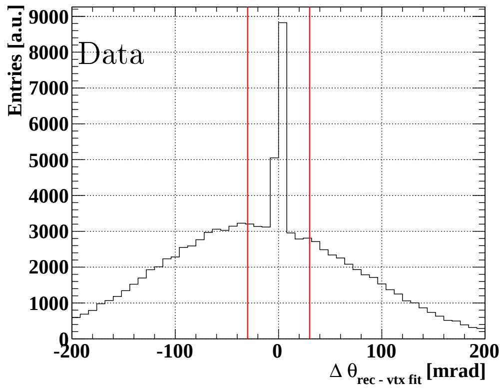

(b) Distribution for θ of data

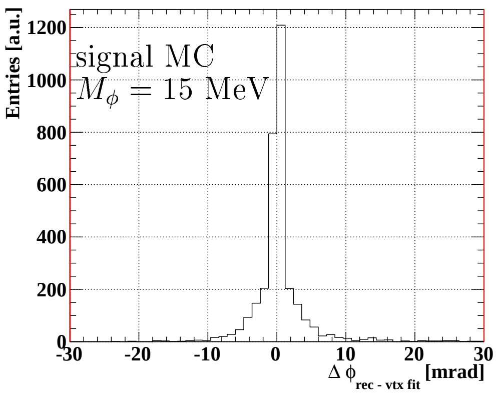

(c) Distribution for φ of signal by MC

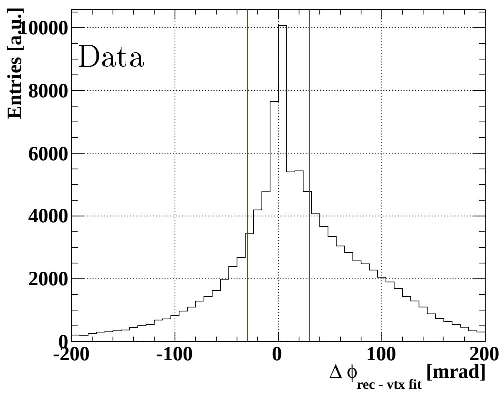

(d) Distribution for φ of data

Figure 5.7: Distribution of difference of θ and ϕ between reconstructed and that from ϕ decay vertex fit. Vertex fit is done expecting M_ϕ to be 15 MeV. Preselection, acceptance cut, energy sum cut, and gamma-ray energy cut are applied. Red line shows cut region. Initial values of θ and φ for ϕ decay vertex fit is equal to that of e^+, so if there is a local minimum around the initial value of the fit, it makes sharp peak at 0 in the distribution shown above. Cut region is set to be 3 σ of the resolution of the positron spectrometer.

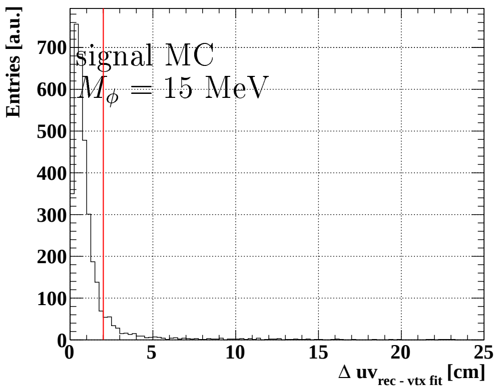

(a) Distribution for incident position in uv of signal by MC

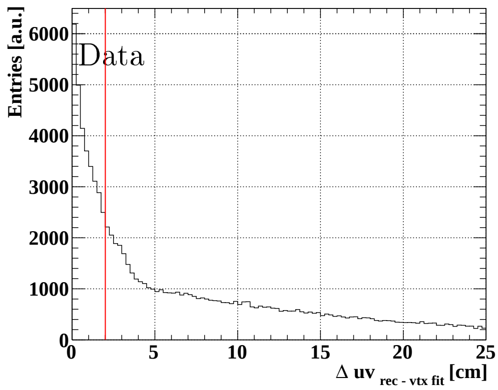

(b) Distribution for incident position in uv of data

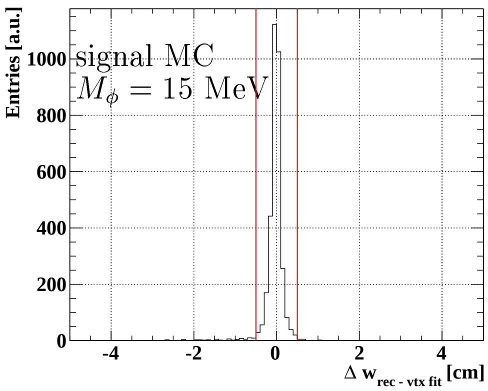

(c) Distribution for incident position in w of signal by MC

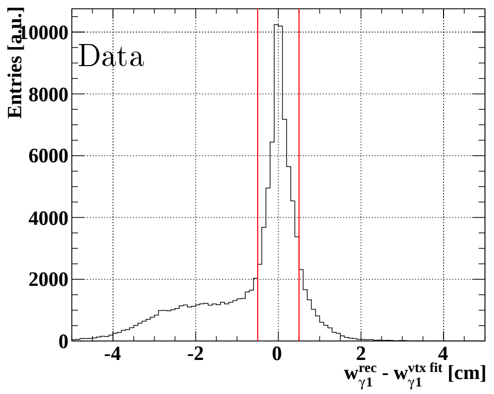

(d) Distribution for incident position in w by data

Figure 5.8: Distribution of $\sqrt{(u_\gamma - u_\gamma^{\text{vtxfit}})^2 + (v_\gamma - v_\gamma^{\text{vtxfit}})^2}$ and $w_\gamma - w_\gamma^{\text{vtxfit}}$. Vertex fit is done expecting M_ϕ to be 15 MeV. Preselection, acceptance cut, energy sum cut, and gamma-ray energy cut are applied. Red line shows cut region.

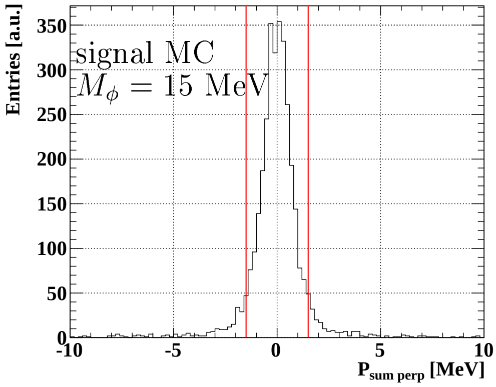

(a) Distribution for $P_{sum,perp}$ of signal by MC

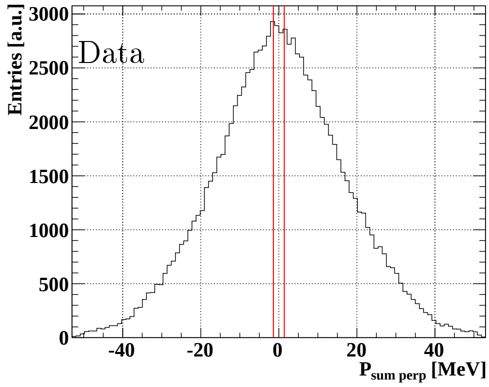

(b) Distribution for $P_{sum,perp}$ of data

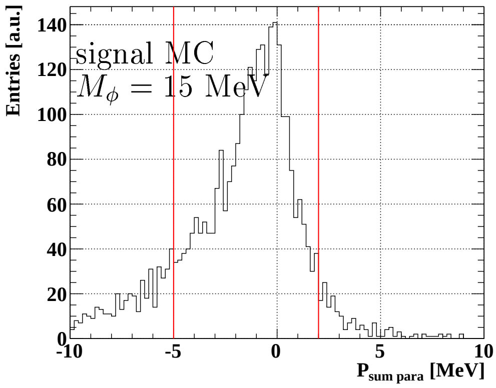

(c) Distribution for $P_{sum,para}$ of signal by MC

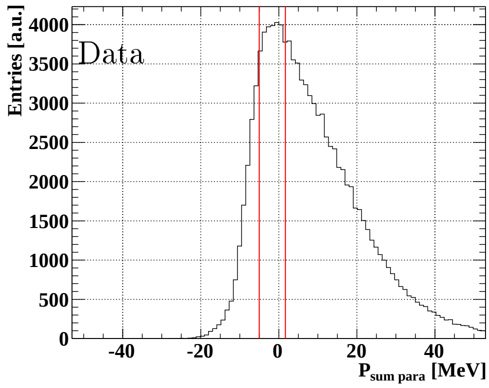

(d) Distribution for $P_{sum,para}$ of data

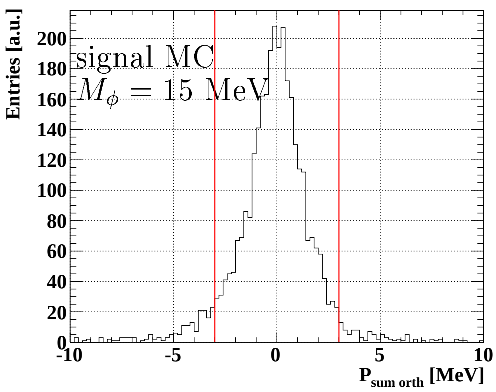

(e) Distribution for $P_{sum,orth}$ of signal by MC

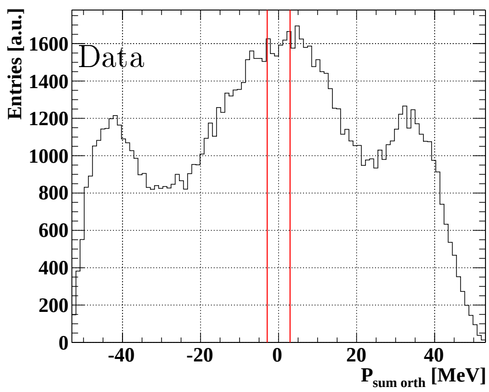

(f) Distribution for $P_{sum,orth}$ of B.G. by data

Figure 5.9: Distribution of the sum of momentum vectors of positron and two gamma-rays. Definition of coordination used here is discussed in Section 3.7.2. Vertex fit is done expecting M_ϕ to be 15 MeV. Preselection, acceptance cut, energy sum cut, and gamma-ray energy cut are applied. Red line shows cut region.

5.2 Backgrounds

We estimate the number of background (B.G.) events which can be misidentified as $\mu^+ \to e^+\phi, \phi \to \gamma\gamma$ using time sideband. B.G.s are classified to four types by the time structure as follows.

i) Two γs induced from one muon decay & coincident Michel e$^+$

  (a) Two γs from annihilation in flight (AIF) & Michel e$^+$

  (b) $\mu^+ \to e^+\nu_e\overline{\nu}_\mu\gamma$, e$^+$ $\to \gamma$ by AIF or bremsstrahlung & Michel e$^+$

ii) e$^+$ and one γ from one muon decay & one γ from another

  (a) $\mu^+ \to e^+\nu_e\overline{\nu}_\mu\gamma$ & $\mu^+ \to e^+\nu_e\overline{\nu}_\mu\gamma$

  (b) $\mu^+ \to e^+\nu_e\overline{\nu}_\mu\gamma$ & γ from AIF or bremsstrahlung of Michel e$^+$

iii) Triple accidental coincidence

  Michel e$^+$ & each γ from $\mu^+ \to e^+\nu_e\overline{\nu}_\mu\gamma$, AIF or bremsstrahlung

iv) All the e$^+$ and two γs induced from one muon decay

  (a) Generic $\mu^+ \to e^+\gamma\gamma$

  (b) $\mu^+ \to e^+\gamma\gamma\nu_\mu\overline{\nu}_e$

B.G. iv) is negligible, because of the limited acceptance of the MEG detector and the small branching ratio. Only e$^+$ with large momentum hits the timing counter (TIC) and the acceptance of the gamma-ray detector is small. The branching ratio of the generic $\mu^+ \to e^+\gamma\gamma$ decay is less than 7.2×10^{-11} [19]. The decay $\mu^+ \to e^+\gamma\gamma\nu_\mu\overline{\nu}_e$ is not well studied and the branching ratio of this decay is not listed on the PDG [33]. But we can expect the probability of misidentifying $\mu^+ \to e^+\gamma\gamma\nu_\mu\overline{\nu}_e$ to be $\mu^+ \to e^+\phi, \phi \to \gamma\gamma$ is quite small because both the neutrinos should have very small momentum, the gamma-rays should be emitted near to each other and the momentum of e$^+$ should be high.

The time sidebands for the B.G. estimation are defined as follows.

(A) $(|\Delta t_{\gamma_1\gamma_2}| < 0.5 \text{ ns}) \wedge (1 \text{ ns} < |\Delta t_{\gamma_1 e^+}| < 3.6 \text{ ns})$ for type i) + iii)

(B) $(1 \text{ ns} < |\Delta t_{\gamma_1\gamma_2}| < 3.6 \text{ ns}) \wedge (|\Delta t_{\gamma_1 e^+} - 0.1 \text{ ns}| < 0.5 \text{ ns})$ for type ii) + iii)

(C) $(1 \text{ ns} < |\Delta t_{\gamma_1\gamma_2}| < 3.6 \text{ ns}) \wedge (1 \text{ ns} < |\Delta t_{\gamma_1 e^+}| < 3.6 \text{ ns})$ for type iii)

Scatter plot of time difference between a gamma-ray with higher energy (γ_1) and a gamma-ray with lower energy (γ_2) versus that between γ_1 and a positron is shown in Figure 5.10(a) together with the defined time sideband. Preselection, acceptance cut, energy sum cut, and gamma-ray energy cut are applied on this plot, without the other signal cuts. From the Figure 5.10, we can see that the event type i) is the major background.

The number of events in each time side band $(N_{obs.(A)}, N_{obs.(B)}, N_{obs.(C)})$ is counted by applying the signal cut with changed time cut. Estimation of the number of events are done at grid point of M_ϕ. They are plotted on the Figure 5.10(b). Because the type iii) B.G. events are included in the time side band regions (A) and (B), and the number of

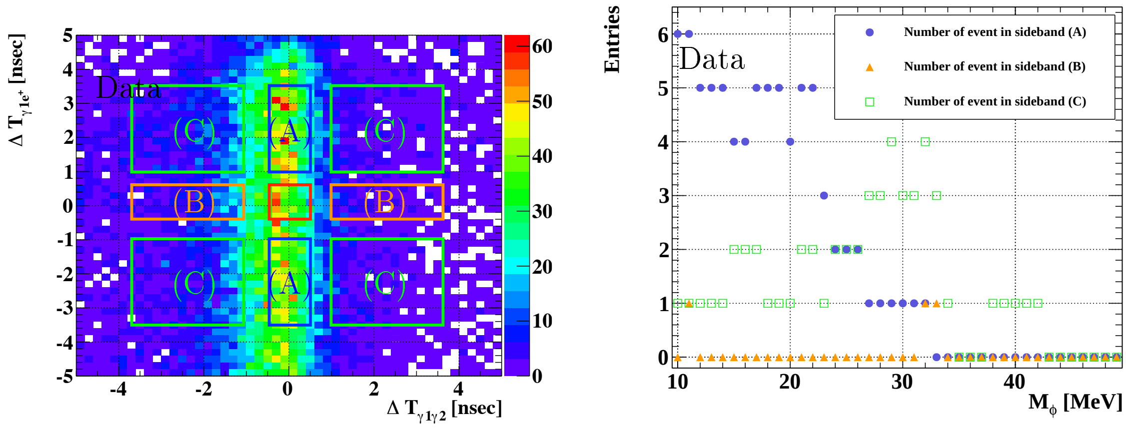

(a) Time structure of preselected events. Most of the signal cuts are not applied.

(b) Distribution of the number of observed events in each time sideband

Figure 5.10: Time sideband and the number of backgrounds. Red shows signal region. Blue, orange, and green represent time sideband regions (A), (B), and (C) respectively.

events can not be negative, the number of each B.G. type of events ($N_{B.G.i)}, N_{B.G.ii)}, N_{B.G.iii)}$) is calculated by,

$$\begin{aligned} N_{B.G.i)} &= \text{Max}(0, N_{obs.(A)} - (0.5/2.6) \times N_{obs.(C)}), \\ N_{B.G.ii)} &= \text{Max}(0, N_{obs.(B)} - (0.5/2.6) \times N_{obs.(C)}), \\ N_{B.G.iii)} &= N_{obs.(C)}. \end{aligned} \tag{5.1}$$

Then the number of expected B.G. in the signal region is calculated as follows,

$$N_{B.G.} = (0.5/2.6) \times N_{B.G.i)} + (0.5/2.6) \times N_{B.G.ii)} + (0.5/2.6) \times (0.5/2.6) \times N_{B.G.iii)}. \tag{5.2}$$

When we have finite B.G. events in all the sideband regions, Equation 5.2 is written as $N_{B.G.} = (N_{obs.(A)}$ term)+($N_{obs.(B)}$ term)−($N_{obs.(C)}$ term). Tail of $N_{B.G.i)}$ in $N_{obs.(B)}$ is canceled by subtraction with $N_{obs.(C)}$. As shown in Figure 5.10(b), $N_{obs.(B)}$ is zero most of the cases. Then term of $N_{obs.(C)}$ is canceled and the Equation 5.2 becomes $N_{B.G.} = (N_{obs.(A)}$ term). We have another case that both $N_{obs.(A)}$ and $N_{obs.(B)}$ are zero. In this case, $N_{B.G} = (N_{obs.(C)}$ term). Because $N_{B.Gi)}$ is negligible, its tail is also negligible.

All in all in the region of 10MeV $< M_\phi <$ 50MeV, the total number of observed events in each time sideband was 14, 2, 11 for region (A), (B), (C) respectively, so the total number of expected number of background in the signal region is 2.7 events.

5.3 Observed events in signal region

The number of observed in the signal region is summarized in Figure 5.11. The total number of observed events in the signal region is 4. This is consistent with no signal event.

Error for the number of events in each time sideband is estimated by square-root of the number except the case the number is zero, in which case 1 is assigned as error for conservative estimation. Then, total error is calculated adding each error values quadratically normalizing with time width.

Table 5.1 shows 90 % confidence level (C.L.) interval by Feldman Cousins method [68]. The number of signal event is zero consistent at all the grid points of mass of ϕ. Note that this includes neither systematic uncertainties nor Poisson statistical errors in the number of observed events. We will estimate bounds on branching ratio later in Section 5.5 taking systematic errors into account.

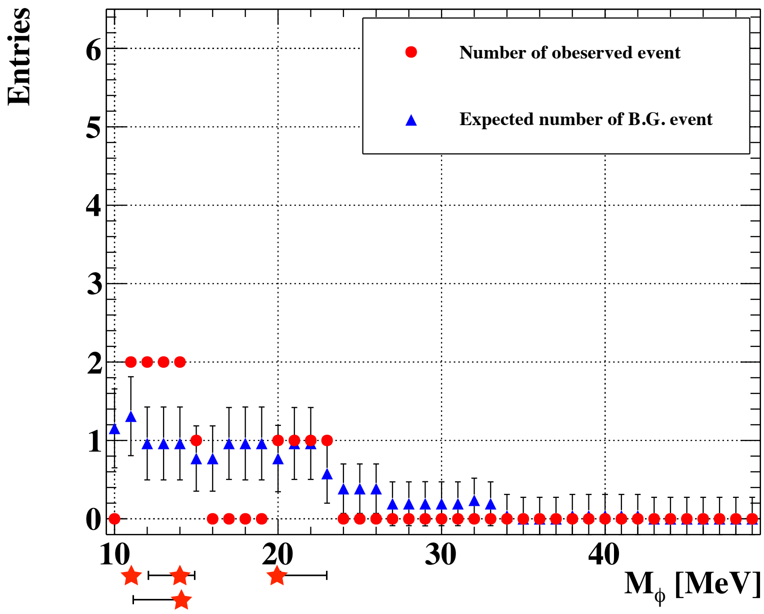

Figure 5.11: The number of observed events (red circle) and expected number of B.G. events (blue triangle) in the signal region. Black bar with red star is mass of each observed event. Red star is the mass that χ^2 of ϕ decay vertex fit was the smallest. Total number of observed events in the signal region was 4.

Table 5.1: 90 % C.L. interval by Feldman Cousins method

M_ϕ [MeV]	10	11	12	13	14	15	16	17	18	19
Upper	1.53	4.61	4.95	4.95	4.95	3.59	1.74	1.63	1.63	1.63
Lower	0.00	0.00	0.00	0.00	0.00	0.00	0.00	0.00	0.00	0.00
M_ϕ [MeV]	20	21	22	23	24	25	26	27	28	29
Upper	3.59	3.40	3.40	3.79	2.06	2.06	2.06	2.25	2.25	2.25
Lower	0.00	0.00	0.00	0.00	0.00	0.00	0.00	0.00	0.00	0.00
M_ϕ [MeV]	30	31	32	33	34	35	36	37	38	39
Upper	2.25	2.25	2.20	2.25	2.40	2.44	2.44	2.44	2.40	2.40
Lower	0.00	0.00	0.00	0.00	0.00	0.00	0.00	0.00	0.00	0.00
M_ϕ [MeV]	40	41	42	43	44	45	46	47	48	49
Upper	2.40	2.40	2.40	2.44	2.44	2.44	2.44	2.44	2.44	2.44
Lower	0.00	0.00	0.00	0.00	0.00	0.00	0.00	0.00	0.00	0.00

5.4 Normalization

The number of signal events ($N_{e\phi,\phi\to\gamma\gamma}$) observed with a certain combination of M_ϕ and τ_ϕ is proportional to the branching ratio, and the relation can be written as,

$$\mathcal{B}(\mu^+ \to e^+\phi, \phi \to \gamma\gamma) = \frac{N_{e\phi,\phi\to\gamma\gamma}}{k}. \tag{5.3}$$

The normalization parameter k is equal to the inverse of the single event sensitivity (S.E.S.). In the experiment, we sometimes suffered from instabilities such as unstable beam intensity or trips of DCH high voltages. Condition of the experiment was not always the same. The normalization factor was evaluated taking these effects into account. We describe here how we extracted it.

The total number of signal events observed in the data taken with $\mu^+ \to e^+\gamma$ search trigger is calculated by,

$$\begin{aligned} N_{e\phi,\phi\to\gamma\gamma} = & \mathcal{B}(\mu^+ \to e^+\phi, \phi \to \gamma\gamma) \times N_\mu \\ & \times A^{e^+}_{e\phi,\phi\to\gamma\gamma} \times A^{\gamma\gamma}_{e\phi,\phi\to\gamma\gamma} \\ & \times \epsilon^{trg:0}_{e\phi,\phi\to\gamma\gamma} \times \frac{1}{P^{trg:0}} \\ & \times \epsilon^{e^+}_{e\phi,\phi\to\gamma\gamma} \times \epsilon^{\gamma\gamma}_{e\phi,\phi\to\gamma\gamma} \\ & \times \epsilon^{cut}_{e\phi,\phi\to\gamma\gamma}, \end{aligned} \tag{5.4}$$

where

$\mathcal{B}(\mu^+ \to e^+\phi, \phi \to \gamma\gamma)$	: The branching ratio of $\mu^+ \to e^+\phi, \phi \to \gamma\gamma$ decay,
N_μ	: The total number of muons stopped on the target during the live time,
$A^{e^+}_{e\phi,\phi\to\gamma\gamma}, A^{\gamma\gamma}_{e\phi,\phi\to\gamma\gamma}$	: Acceptance of the positron spectrometer and the LXe gamma-ray detector for $\mu^+ \to e^+\phi, \phi \to \gamma\gamma$ decay,
$\epsilon^{trg:0}_{e\phi,\phi\to\gamma\gamma}$	: Trigger efficiency for the $\mu^+ \to e^+\phi, \phi \to \gamma\gamma$ events by $\mu^+ \to e^+\gamma$ trigger (id=0),
$P^{trg:0}$	: $= 1$, Pre-scale factor of $\mu^+ \to e^+\gamma$ trigger (id=0) which is described in Section 2.6.2,
$\epsilon^{e^+}_{e\phi,\phi\to\gamma\gamma}, \epsilon^{\gamma\gamma}_{e\phi,\phi\to\gamma\gamma}$	: Reconstruction efficiency of positron and two gamma-rays,
$\epsilon^{cut}_{e\phi,\phi\to\gamma\gamma}$	: Efficiency of signal cut.

As mentioned in Section 2.6.2, we take Michel decay ($\mu^+ \to e^+\nu_e\overline{\nu}_\mu$) data with TIC self-trigger (id=22) in parallel with $\mu^+ \to e^+\gamma$ trigger data. The number of Michel positrons with momentum in a certain range can be written in a similar way to $N_{e\phi,\phi\to\gamma\gamma}$ as follows.

$$\begin{aligned}
N_{e\nu\overline{\nu}} = &\mathcal{B}(\mu^+ \to e^+\nu_e\overline{\nu}_\mu) \times N_\mu \\
&\times f_{e\nu\overline{\nu}}^{P_e\text{selection}} \\
&\times A_{e\nu\overline{\nu}}^{e^+} \\
&\times \epsilon_{e\nu\overline{\nu}}^{trg:22} \times \frac{1}{P^{trg:22}} \\
&\times \epsilon_{e\nu\overline{\nu}}^{e^+},
\end{aligned} \tag{5.5}$$

where

$\mathcal{B}(\mu^+ \to e^+\nu_e\overline{\nu}_\mu)$: $\sim 100\%$, The branching ratio of $\mu^+ \to e^+\nu_e\overline{\nu}_\mu$ decay,

$f_{e\nu\overline{\nu}}^{P_e\text{selection}}$: The fraction of Michel spectrum in a certain momentum range,

$A_{e\nu\overline{\nu}}^{e^+}$: Acceptance of the positron spectrometer for $\mu^+ \to e^+\nu_e\overline{\nu}_\mu$ decay,

$\epsilon_{e\nu\overline{\nu}}^{trg:22}$: Trigger efficiency of TIC alone trigger (id=22),

$P^{trg:22}$: $= 10^7$, Pre-scale factor of TIC alone trigger (id=22),

$\epsilon_{e\nu\overline{\nu}}^{e^+}$: Reconstruction efficiency of positron.

Here, N_μ is the same as that of Equation 5.4 as we use the data taken in parallel. From Equation 5.3, 5.4, and 5.5, we can obtain the normalization factor as follows.

$$1/k = \frac{1}{N_{e\nu\overline{\nu}}} \times \frac{f_{e\nu\overline{\nu}}^{E_e\text{selection}}}{P^{trg:22}} \times \frac{A_{e^+}^{e\nu\overline{\nu}}}{A_{e^+}^{e\phi,\phi\to\gamma\gamma}} \times \frac{1}{A_{\gamma\gamma}^{e\phi,\phi\to\gamma\gamma}} \times \frac{\epsilon_{e\nu\overline{\nu}}^{trg:22}}{\epsilon_{e\phi,\phi\to\gamma\gamma}^{trg:0}} \times \frac{\epsilon_{e\nu\overline{\nu}}^{e^+}}{\epsilon_{e\phi,\phi\to\gamma\gamma}^{e^+}} \times \frac{1}{\epsilon_{e\phi,\phi\to\gamma\gamma}^{\gamma\gamma}} \times \frac{1}{\epsilon_{e\phi,\phi\to\gamma\gamma}^{cut}}. \tag{5.6}$$

We evaluate the normalization factor with the product of the number of the Michel positrons, the relative acceptance and efficiency of the positron spectrometer, and acceptance and efficiency of the gamma-ray detector. $N_{e\nu\overline{\nu}}$ is measured using the experimental data, and the other parameters are estimated by using MC simulation of signal events for different sets of mass and lifetime values.

We select Michel positron momentum near the target momentum of $\mu^+ \to e^+\phi, \phi \to \gamma\gamma$ positron according to M_ϕ. The behavior of the positron with the same momentum is expected to be the same for the Michel decay and the signal. $N_{e\nu\overline{\nu}}$ is evaluated from the data taken in parallel with the physics data, so we can evaluate the periodical changes in the beam and positron spectrometer conditions. Efficiency of the positron spectrometer differs accoriding to the data taking period, but relative efficiency $(\epsilon_{e\nu\overline{\nu}}^{e^+}/\epsilon_{e\phi,\phi\to\gamma\gamma}^{e^+})$ can be stably estimated with the help of the energy selection. The combination of the estimation of the number of Michel positrons taken in parallel and its momentum selection gives stable evaluation of the normalization factor.

Efficiencies and acceptances were evaluated for the mass values between 10 and 40 MeV with an interval of 5 MeV and for the lifetime of 10 ps, 100 ps, 1 ns, 10 ns, using MC simulations. Then interpolation is performed for the masses in-between. This is because MC simulation needs a lot of time and disk space. The reconstructed values were conservatively smeared to reproduce the detector performance of the 2009 experiment.

In the following sections, we are going to see fraction of the positron momentum selection (Sec. 5.4.1), acceptance of the positron spectrometer (Sec. 5.4.2) and the gamma-ray detector (Sec. 5.4.3), efficiency of the direction match of trigger setting (Sec. 5.4.4), efficiency of the positron selection (Sec. 5.4.5) and the gamma-ray reconstruction (Sec. 5.4.6), signal cut efficiency (Sec. 5.4.7) and trigger efficiency of gamma-ray energy selection (Sec. 5.4.8). Selection is performed according to the order of the section number. Applied requirements of the former sections are applied to the following sections.

5.4.1 Positron momentum selection

In this section, we estimate the fraction of momentum selection on Michel positron.

The number of DCH hits used for track fitting is smaller for low momentum positrons because of smaller radius of the helical trajectory. Therefore track fitting suffers more from trips of DCH HV for low momentum positrons. Efficiency of positron spectrometer depends on run period. However, behavior of positrons with the same momentum is expected to be the same both for the Michel decay and $\mu^+ \to e^+\phi, \phi \to \gamma\gamma$ decay. Therefore proper selection of the positron momentum helps stable estimation of the normalization.

Positron momentum of ϕ-mediated muon decay is monochromatic which is calculated by Equation 3.1 for a given M_ϕ. On the other hand, Michel positron momentum follows a certain spectrum. Figure 5.12 shows momentum spectrum of Michel positron. Red line is theoretical spectrum, green one is smeared spectrum with energy resolution, and blue one is that containing geometrical acceptance and track fit efficiency of the MEG positron spectrometer. Upper tail is made by the energy resolution, and lower one is mainly by geometrical acceptance.

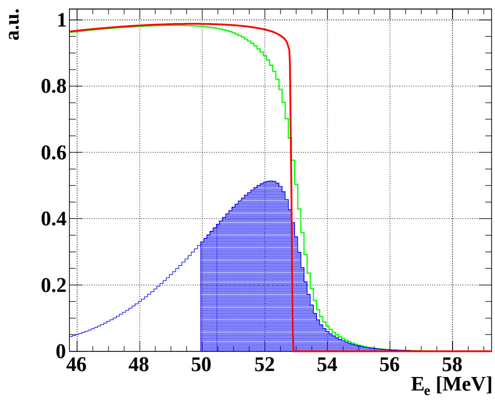

Figure 5.12: Momentum spectrum of Michel positron. Red line: theoretical Michel spectrum including radiative correction. Green line: red one smeared by detector resolution. Blue line: "good" positron detected by the MEG spectrometer. Blue hatched region: the momentum selection region for $M_\phi \leq 20$MeV/c.

If M_ϕ is very light, momentum of signal positron come closer to the upper edge of the Michel spectrum. In this case, we set energy selection region between 50 MeV and 56 MeV to include the tail made by momentum resolution. On the other hand, in the case that M_ϕ is large enough, we select momentum for the estimation of the number of Michel positron in the region that is within $|P_\phi| \pm 1$MeV.

When $M_\phi = 20$MeV, $P_\phi \simeq 51$MeV, and when $M_\phi = 25$MeV, $P_\phi \simeq 50$MeV. We use the energy region 50MeV $< P_e <$ 56MeV when $M_\phi \leq 20$MeV, and $|P_e - P_\phi| < 1$MeV when $M_\phi \geq 25$MeV. The fraction is estimated with Michel positron MC simulation applying energy selection for each cases of M_ϕ. Only the selection of momentum is performed here, and no acceptance cut or so is performed for the estimation of the fraction. The result appears in Table 5.2. Energy selection is done using energy of simulation truth, then corrected taking the energy resolution into account.

Table 5.2: The fraction of Michel spectrum

M_ϕ [MeV]	10, 15, 20	25	30
$E_e$selection [MeV]	$50 < E_e < 56$	$\lvert E_e - 49.9\rvert < 1.0$	$\lvert E_e - 48.6\rvert < 1.0$
$f_{e\nu\overline{\nu}}^{E_e\text{selection}}$	$(9.9 \pm 0.2) \times 10^{-2}$	$(7.1 \pm 0.2) \times 10^{-2}$	$(6.8 \pm 0.2) \times 10^{-2}$
M_ϕ [MeV]	35	40	45
$E_e$selection [MeV]	$\lvert E_e - 47.0\rvert < 1.0$	$\lvert E_e - 45.3\rvert < 1.0$	$\lvert E_e - 43.2\rvert < 1.0$
$f_{e\nu\overline{\nu}}^{E_e\text{selection}}$	$(7.2 \pm 0.2) \times 10^{-2}$	$(6.9 \pm 0.3) \times 10^{-2}$	$(8.1 \pm 0.7) \times 10^{-2}$

5.4.2 Relative acceptance for positron

Positron acceptance for $\mu^+ \to e^+\phi, \phi \to \gamma\gamma$ event; $A_{e^+}^{e\phi,\phi\to\gamma\gamma}$ is defined as the probability of having at least one timing-counter hit for isotropically generated signal events. Positron acceptance for $\mu^+ \to e^+\nu_e\overline{\nu}_\mu$ event; $A_{e^+}^{e\nu\overline{\nu}}$ is defined as the same probability for isotropically generated $\mu^+ \to e^+\nu_e\overline{\nu}_\mu$ positrons with the energy written in Table 5.2.

Relative acceptance for positron does not depend on the lifetime of ϕ (τ_ϕ), but on the mass of ϕ (M_ϕ), so it is estimated for each M_ϕ. As we compare acceptance for positrons with similar energy, the relative acceptance is near to 100% as shown in Table 5.3. Listed error is statistical error.

Table 5.3: Relative acceptance for positron

M_ϕ [MeV]	10	15	20	25
$(A_{e^+}^{e\nu\overline{\nu}})/(A_{e^+}^{e\phi,\phi\to\gamma\gamma})(\%)$	89.9 ± 1.0	95.1 ± 1.1	105.6 ± 1.2	101.1 ± 1.5
M_ϕ [MeV]	30	35	40	45
$(A_{e^+}^{e\nu\overline{\nu}})/(A_{e^+}^{e\phi,\phi\to\gamma\gamma})$ (%)	101.7 ± 1.7	98.6 ± 2.0	96.9 ± 2.5	87.7 ± 3.1

5.4.3 Acceptance for two gamma-rays

We estimate here the acceptance for two gamma-rays. Estimation is performed using MC truth of gamma-ray emission direction and energy deposit in liquid xenon. Estimation by reconstructed values will be done in the Section 5.4.6. Acceptance for two gamma-rays is defined here as follows.

- Energy deposit of each gamma-ray in liquid xenon > 5 MeV
- Total energy deposit in liquid xenon > 40 MeV

- ϕ decays before passing inner face of the LXe detector; $\sqrt{x_{\phi\mathrm{decay}}^2 + y_{\phi\mathrm{decay}}^2} < 67.85$cm
- Gamma direction is within the extended detector acceptance; $|u_\gamma| < 28.1$ cm , $|v_\gamma| < 74.1$ cm at $w_\gamma = 0$ cm for each gamma-ray.

Acceptance of the incident position in the analysis is defined that $|u_\gamma| < 25$ cm, $|v_\gamma| < 71$ cm, and we require here the direction of gamma-ray is within the extended range; $|u_\gamma| < 28.1$ cm, $|v_\gamma| < 74.1$ cm, which are set large enough taking the detector resolution into account. Here, u_γ and v_γ are estimated extending the gamma direction of MC truth from the generating point until it reaches the inner face of the LXe detector ($\sqrt{x^2 + y^2} = 67.85$ cm). As the positron direction is limited to the acceptance of positron spectrometer which is back to back to the LXe detector, center of the two gamma-rays should be already restricted around the acceptance, so the estimated values here can become larger than the solid angle of the LXe detector ($\sim 10\%$).

The estimation is done for each M_ϕ and τ_ϕ sets. The result with statistical error is listed in Table 5.4.

Table 5.4: Acceptance for two gamma-rays

	M_ϕ [MeV]	10	15	20	25
$A_{\gamma\gamma}^{e\phi,\phi\to\gamma\gamma}(\%)$	$(\tau_\phi = 10\mathrm{ps})$	24.2 ± 0.2	16.6 ± 0.2	10.4 ± 0.2	7.5 ± 0.1
	$(\tau_\phi = 100\mathrm{ps})$	28.6 ± 0.2	20.2 ± 0.2	13.0 ± 0.2	9.0 ± 0.2
	$(\tau_\phi = 1\mathrm{ns})$	13.6 ± 0.2	16.1 ± 0.2	16.1 ± 0.2	15.4 ± 0.2
	$(\tau_\phi = 10\mathrm{ns})$	1.7 ± 0.1	2.3 ± 0.1	2.7 ± 0.1	2.9 ± 0.1
	M_ϕ [MeV]	30	35	40	45
$A_{\gamma\gamma}^{e\phi,\phi\to\gamma\gamma}(\%)$	$(\tau_\phi = 10\mathrm{ps})$	5.8 ± 0.1	4.1 ± 0.1	2.7 ± 0.1	1.8 ± 0.1
	$(\tau_\phi = 100\mathrm{ps})$	6.2 ± 0.1	4.7 ± 0.2	3.5 ± 0.2	2.1 ± 0.2
	$(\tau_\phi = 1\mathrm{ns})$	13.6 ± 0.2	11.3 ± 0.2	8.8 ± 0.3	6.9 ± 0.3
	$(\tau_\phi = 10\mathrm{ns})$	2.8 ± 0.1	3.1 ± 0.1	3.0 ± 0.2	3.2 ± 0.2

Longer lifetime makes the probability that ϕ decays near the detector bigger, which makes the acceptance better, however, too long lifetime makes it worse because the probability that ϕ penetrates the detector without decaying into gamma-rays increases.

Smaller M_ϕ makes the angle between two gamma-rays smaller with the Lorentz boost effect, and larger M_ϕ makes this opening angle bigger. So, the acceptance is better in case that ϕ has smaller mass. But when the mass is too small, effective lifetime of ϕ in the experimental frame becomes longer by the Lorenz boost effect, and this makes flight length longer and effects on the acceptance.

5.4.4 Direction match trigger efficiency

We discuss about trigger efficiency in this section. Trigger settings for trigger id=0, 22 are described in Table 2.4. Trigger id = 0 is the trigger for $\mu^+ \to e^+\gamma$ search and id = 22 is the trigger for Michel decay ($\mu \to e\nu_\mu\overline{\nu}_e$). Trigger efficiency is estimated for the events which satisfy acceptance requirements. Acceptance is discussed in Section 5.4.2 and 5.4.3.

Positron acceptance is already satisfied, so the trigger efficiency for trigger id = 22 ($\epsilon_{e\nu\overline{\nu}}^{trg:22}$) is equal to 1.

Trigger id=0 is composed of three components; $\epsilon^{trg:0}_{e\phi,\phi\to\gamma\gamma} = \epsilon^{E_\gamma THR}_{e\phi,\phi\to\gamma\gamma} \times \epsilon^{T_{e\gamma}}_{e\phi,\phi\to\gamma\gamma} \times \epsilon^{DM}_{e\phi,\phi\to\gamma\gamma}$, where $\epsilon^{E_\gamma THR}_{e\phi,\phi\to\gamma\gamma}$, $\epsilon^{T_{e\gamma}}_{e\phi,\phi\to\gamma\gamma}$ and $\epsilon^{DM}_{e\phi,\phi\to\gamma\gamma}$ represent the trigger efficiency of gamma-ray energy selection, gamma-ray positron coincident event selection and the direction match selection respectively. Because time window of trigger id=0 is large enough for $\mu^+ \to e^+\phi, \phi \to \gamma\gamma$ event, $\epsilon^{T_{e\gamma}}_{e\phi,\phi\to\gamma\gamma}$ is equal to 1. So we should estimate efficiency of direction match and gamma-ray energy thresholds. Efficiency of direction match is estimated here, and estimate efficiency of gamma-ray energy selection of trigger later in Section 5.4.8.

Direction match is designed to trigger back to back positron and gamma-ray with the energy equal to half the muon mass. Look up table for the direction match; i.e. the PMT with the largest incoming photon and z of the TICP first hit position; is made using $\mu^+ \to e^+\gamma$ MC simulation. We check if the event satisfies the look up table. Table 5.5 summarize the efficiency of the direction match. Longer lifetime makes the probability that ϕ decays near the detector bigger, and this helps to make the direction match efficiency better. Smaller M_ϕ also results in better direction-match efficiency, because stronger Lorentz boost makes the opening angle between gamma-ray and positron near back to back. Larger M_ϕ makes positron momentum smaller, which makes the radius of positron trajectory smaller and hit position on TIC bar different from the case of 52.8 MeV positron.

Table 5.5: Direction match efficiency

	M_ϕ [MeV]	10	15	20	25
$\epsilon^{DM}_{e\phi,\phi\to\gamma\gamma}(\%)$	$(\tau_\phi = 10\text{ps})$	61.0 ± 0.6	45.0 ± 0.5	36.3 ± 0.5	28.3 ± 0.5
	$(\tau_\phi = 100\text{ps})$	68.1 ± 0.6	51.0 ± 0.5	39.7 ± 0.5	31.5 ± 0.5
	$(\tau_\phi = 1\text{ns})$	73.9 ± 0.6	67.0 ± 0.6	59.5 ± 0.6	51.7 ± 0.6
	$(\tau_\phi = 10\text{ns})$	75.0 ± 0.6	68.8 ± 0.6	61.6 ± 0.6	54.5 ± 0.6
	M_ϕ [MeV]	30	35	40	45
$\epsilon^{DM}_{e\phi,\phi\to\gamma\gamma}(\%)$	$(\tau_\phi = 10\text{ps})$	22.9 ± 0.5	18.1 ± 0.5	14.4 ± 0.6	13.0 ± 0.7
	$(\tau_\phi = 100\text{ps})$	24.8 ± 0.5	20.5 ± 0.5	18.2 ± 0.6	15.0 ± 0.8
	$(\tau_\phi = 1\text{ns})$	42.7 ± 0.6	33.9 ± 0.6	27.7 ± 0.7	23.2 ± 0.9
	$(\tau_\phi = 10\text{ns})$	47.0 ± 0.6	38.0 ± 0.6	31.3 ± 0.7	26.1 ± 0.9

5.4.5 Positron relative efficiency

We discussed about the selection criteria to ensure the quality of positron track fit in Section 3.5.5. We check the efficiency of the selection in this section. The efficiency of the selection is estimated using the events which satisfy the detector acceptance cut and trigger setting.

The result is shown in Table 5.6. From this table, we can see that the positron selection efficiency for $\mu^+ \to e^+\phi, \phi \to \gamma\gamma$ decay is better than that for $\mu^+ \to e^+\nu_e\overline{\nu}_\mu$ decay. As described in Section 5.4.3, both two gamma-rays are requested to be inside the extended detector acceptance. This decreases events near the edge of positron spectrometer acceptance, which result in better efficiency for the $\mu^+ \to e^+\phi, \phi \to \gamma\gamma$ decay.

Table 5.6: Positron relative selection efficiency

	M_ϕ [MeV]	10	15	20	25
$\epsilon^{e^+}_{e\nu\bar{\nu}}/\epsilon^{e^+}_{e\phi,\phi\to\gamma\gamma}(\%)$	$(\tau_\phi = 10\text{ps})$	69.7 ± 1.3	71.4 ± 1.5	72.9 ± 1.6	74.0 ± 2.1
	$(\tau_\phi = 100\text{ps})$	70.3 ± 1.3	70.6 ± 1.4	72.6 ± 1.6	74.7 ± 2.1
	$(\tau_\phi = 1\text{ns})$	70.8 ± 1.3	71.2 ± 1.3	73.3 ± 1.4	72.8 ± 1.8
	$(\tau_\phi = 10\text{ns})$	71.2 ± 1.3	71.3 ± 1.3	73.2 ± 1.4	73.8 ± 1.8
	M_ϕ [MeV]	30	35	40	45
$\epsilon^{e^+}_{e\nu\bar{\nu}}/\epsilon^{e^+}_{e\phi,\phi\to\gamma\gamma}(\%)$	$(\tau_\phi = 10\text{ps})$	72.0 ± 2.5	73.5 ± 3.5	69.1 ± 5.2	81.2 ± 10.9
	$(\tau_\phi = 100\text{ps})$	70.3 ± 2.4	73.6 ± 3.4	63.5 ± 4.4	67.3 ± 8.2
	$(\tau_\phi = 1\text{ns})$	73.7 ± 2.2	80.9 ± 3.2	78.2 ± 4.9	93.2 ± 10.6
	$(\tau_\phi = 10\text{ns})$	73.9 ± 2.2	82.9 ± 3.2	75.1 ± 4.5	97.2 ± 10.7

5.4.6 Gamma-ray efficiency

Gamma-ray efficiency is defined here as the probability that reconstruction of two gamma-rays satisfy following requirements.

- Position, energy and time fit do not diverge and are successfully finished,
- $\sqrt{(u_{\gamma1} - u_{\gamma2})^2 + (v_{\gamma1} - v_{\gamma2})^2} > 20\text{cm}$,
- $|u_\gamma| < 25\text{cm} \wedge |v_\gamma| < 71\text{cm}$ for each gamma-rays,
- $E_{\gamma2} > 10\text{MeV}$ $(E_{\gamma1} > E_{\gamma2})$,
- $E_{\gamma1} + E_{\gamma2} > 40\text{MeV}$.

The result is summarized in Table 5.7.

Table 5.7: Gamma-ray efficiency

	M_ϕ [MeV]	10	15	20	25
$\epsilon^{\gamma\gamma}_{e\phi,\phi\to\gamma\gamma}(\%)$	$(\tau_\phi = 10\text{ps})$	58.3 ± 0.8	59.9 ± 1.0	61.5 ± 1.2	60.8 ± 1.5
	$(\tau_\phi = 100\text{ps})$	32.8 ± 0.6	56.2 ± 0.9	56.9 ± 1.1	59.5 ± 1.4
	$(\tau_\phi = 1\text{ns})$	10.4 ± 0.3	22.5 ± 0.5	29.5 ± 0.6	36.4 ± 0.8
	$(\tau_\phi = 10\text{ns})$	8.6 ± 0.3	18.6 ± 0.4	24.5 ± 0.5	29.7 ± 0.7
	M_ϕ [MeV]	30	35	40	45
$\epsilon^{\gamma\gamma}_{e\phi,\phi\to\gamma\gamma}(\%)$	$(\tau_\phi = 10\text{ps})$	62.0 ± 2.0	62.6 ± 2.8	58.8 ± 4.6	60.0 ± 8.4
	$(\tau_\phi = 100\text{ps})$	61.3 ± 1.9	59.8 ± 2.6	61.9 ± 4.0	67.2 ± 7.6
	$(\tau_\phi = 1\text{ns})$	41.4 ± 1.1	46.7 ± 1.8	53.9 ± 3.1	57.0 ± 6.2
	$(\tau_\phi = 10\text{ns})$	35.8 ± 1.0	41.7 ± 1.5	43.1 ± 2.4	54.5 ± 5.7

Loss of the efficiency stems from the requirement of the distance between interaction positions of two gamma-rays. We can see from the Table 5.7 that efficiency is smaller for the case of smaller M_ϕ, because of smaller angle between two gamma-rays. Longer lifetime make the ϕ decay vertex position to distribute near the detector , which also makes the distance between incident positions of two gamma-rays smaller and makes the efficiency smaller.

5.4.7 Event selection efficiency

Definition of analysis cuts is shown in Section 5.1 As we already estimated the effect of the acceptance cuts, gamma-ray energy cut, and cut for pileup search quality, we estimate here the efficiency for positron energy cut, cuts for ϕ decay vertex fit quality, and cut of momentum and energy conservation. The result is summarized in Table 5.8.

As shown in the Figure 5.5–5.9 in Section 5.1, loss of efficiency stems in the energy loss of gamma-ray by shower escape.

In case that τ_ϕ is long or M_ϕ is large, more gamma-rays are expected to enter the detector with large incident angle , which are expected to be reconstructed with worse resolutions.

Table 5.8: Cut efficiency

	M_ϕ [MeV]	10	15	20	25
$\epsilon^{cut}_{e\phi,\phi\to\gamma\gamma}(\%)$	$(\tau_\phi = 10\text{ps})$	43.8 ± 0.9	47.0 ± 1.2	48.1 ± 1.4	50.0 ± 1.8
	$(\tau_\phi = 100\text{ps})$	44.6 ± 1.2	45.8 ± 1.1	45.2 ± 1.3	46.5 ± 1.7
	$(\tau_\phi = 1\text{ns})$	43.2 ± 1.9	46.3 ± 1.4	41.3 ± 1.3	39.1 ± 1.4
	$(\tau_\phi = 10\text{ns})$	43.5 ± 2.0	44.0 ± 1.5	40.4 ± 1.4	36.9 ± 1.4
	M_ϕ [MeV]	30	35	40	45
$\epsilon^{cut}_{e\phi,\phi\to\gamma\gamma}(\%)$	$(\tau_\phi = 10\text{ps})$	47.3 ± 2.2	40.8 ± 2.9	37.1 ± 4.7	23.5 ± 6.8
	$(\tau_\phi = 100\text{ps})$	45.1 ± 2.1	43.8 ± 2.9	31.4 ± 3.6	29.5 ± 6.1
	$(\tau_\phi = 1\text{ns})$	33.5 ± 1.6	29.9 ± 2.0	24.3 ± 2.8	22.4 ± 5.1
	$(\tau_\phi = 10\text{ns})$	32.0 ± 1.5	25.4 ± 1.8	22.5 ± 2.7	23.1 ± 5.0

5.4.8 Gamma-ray trigger efficiency

We changed trigger setting of gamma-ray energy selection three times during 2009 and 2010; gamma-ray threshold is lowered a bit during 2009, gamma-ray energy online estimator is changed at the beginning of 2010, and cosmic ray veto threshold is raised early in 2010. For the convenience, we name here each period 2009a, 2009b, 2010a, and 2010b.

Total energy of two gamma-rays of $\mu^+ \to e^+\phi, \phi \to \gamma\gamma$ decay is larger than the case of $\mu^+ \to e^+\gamma$ decay, so the trigger threshold which is aimed to trigger $\mu^+ \to e^+\gamma$ decay is not a big problem, but cosmic-ray veto threshold except the period of latter part of 2010 can affect if M_ϕ is large.

Gamma-ray efficiency curve of trigger for each period is made using π^0-55 MeV gamma-ray calibration data (Section 2.5.4) which is triggered with gamma-ray energy threshold lower than that of trigger $id = 0$ without veto threshold. Although original energy of the gamma-ray is fixed approximately 55 and 83 MeV, some of the gamma-rays lose some energy before entering the detector with reaction with the material of magnet and so on. Then, collected data contains gamma-ray events of various energies lower than 55 or 83 MeV. We record also the information used for trigger, so we can check how the trigger setting works afterwards. The efficiency curve histogram is obtained comparing the reconstructed energy spectrum with and without trigger gamma-ray energy selection settings. Figure 5.13 shows the obtained curve. Gamma-ray energy estimator of trigger have worse resolution than that of the analysis, which makes this curve.

The efficiency is estimated multiplying the histogram with energy spectrum of $\mu^+ \to e^+\phi, \phi \to \gamma\gamma$ data which survived all the cuts. Efficiencies for the period 2009a, 2009b, 2010a and 2010b are 79–88, 81–89, 86–96 and 91–97 % respectively.

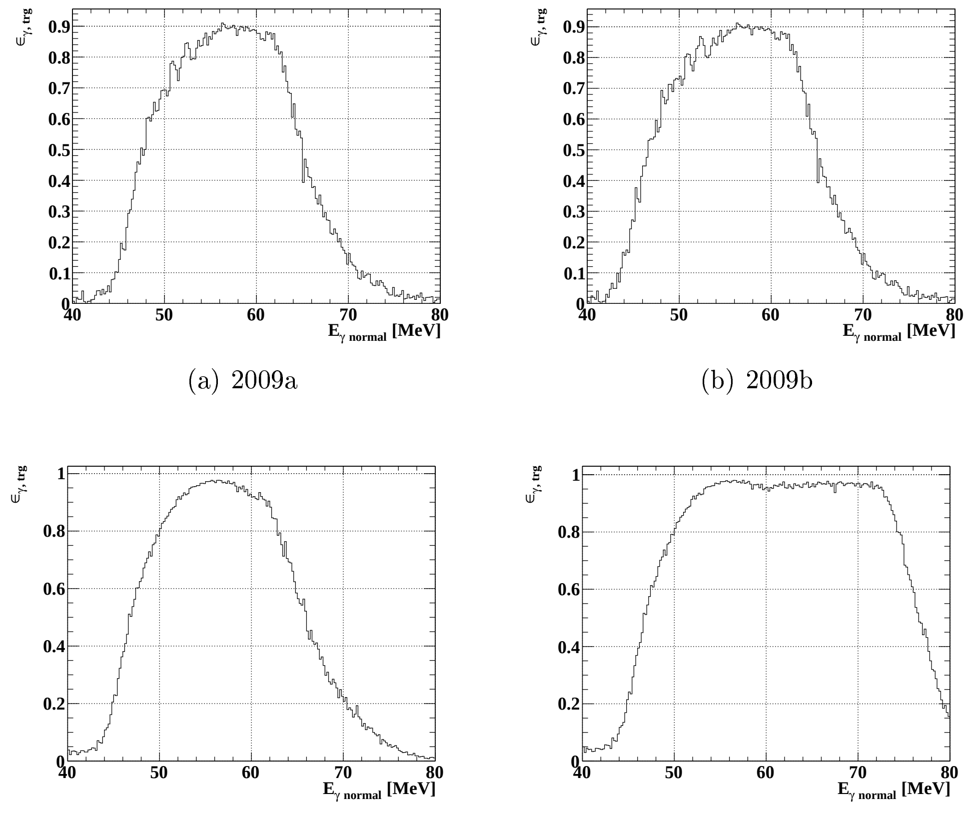

(a) 2009a (b) 2009b

(c) 2010a (d) 2010b

Figure 5.13: Trigger efficiency of gamma-ray energy selection. $E_{\gamma normal}$ is a reconstructed total energy deposit in the LXe detector.

5.4.9 The number of measured Michel positrons

The number of Michel positrons is counted selecting its energy as described in Section 5.4.1. As mentioned in Section 5.4.8, there are four periods with different gamma-ray efficiency. Then the number of measured Michel positrons is counted separately according to the change of trigger setting of gamma-ray energy selection.

Table 5.9 shows the number of Michel positrons for each period.

Table 5.9: The number of measured Michel positrons

M_ϕ [MeV]	10, 15, 20	25	30	35	40	45
$N_{e\nu\bar{\nu}}$ in 2009a	10047	6208	4799	3091	1619	670
2009b	5627	3390	2738	1770	976	380
2010a	1179	684	550	321	155	57
2010b	29562	16493	11769	7172	3459	1287

5.4.10 Systematic uncertainties

Systematic uncertainties mainly come from incompleteness of MC simulations and smearing. Systematic error is estimated adding following two components.

Gamma-ray detector efficiency
: As described in the Section 4.2.1, gamma-ray detector efficiency is estimated to be 65 % in MC and 64-67 % in the experiment. We observe two gamma-rays, so square of the difference gives the effect of the uncertainty of gamma-ray detector efficiency. The effect is then estimated to be 6.2 %.

Detector resolutions and calibrations
: Smearing factors and their uncertainties are discussed in the Chapter 4. Effect of the uncertainties in the reproducibility of the resolutions and the calibrations are estimated by adding the uncertainties to the smearing parameters and shifting the reconstructed values with uncertainties in mean. We estimate the normalization factor for whole the period and compared the results with and without the additional smearing, changing scales, and shifting the reconstructed position with the uncertainty in the alignment.

Contribution of uncertainty in positron spectrometer performance is small because we use relative efficiency of $\mu^- \to e^-\nu_e\overline{\nu}_\mu$ and $\mu^+ \to e^+\phi, \phi \to \gamma\gamma$ by the MEG detector, and behavior of positrons with approximately the same momentum are expected to be the same. Systematic uncertainty stems the resolutions of the detectors and the efficiency of the gamma-ray detector, especially uncertainty in gamma-ray time reconstruction because we assign large value for a conservative analysis.

5.4.11 Interpolation

We can now calculate the normalization factor k of each period combining the result of the Section 5.4.1–5.4.8 according to the equation 5.6. We separate the estimation of the efficiencies and acceptances to see each contribution, but in the analysis, we apply all the selection criteria at once, and use overall efficiency. The normalization factor for all the period (k_{total}) can be calculated by adding them as,

$$k_{total} = k_{2009a} + k_{2009b} + k_{2010a} + k_{2010b}, \tag{5.7}$$

where k_{2009a} and so on represent the normalization factor for each period. Then the single event sensitivity for each period is obtained from the inverse of k_{total}. $1/k_{total}$ with statistical error is shown in Figure 5.14.

We generate MC with a Interval of 5 MeV for M_ϕ. Points in-between are interpolated by fitting nearest four points with exponential of third order polynomial function. We also perform fitting nearest three points with exponential of second order polynomial function, and the difference is taken as systematic error of interpolation. An example of the interpolation is shown in Figure 5.15.

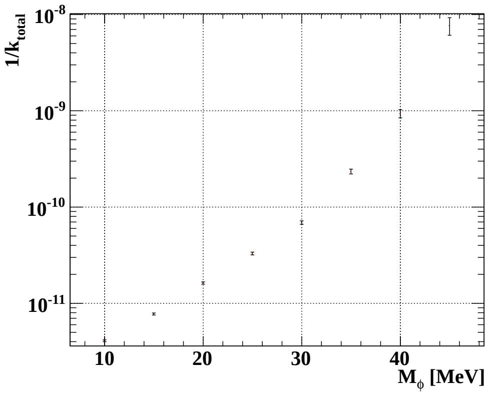

(a) $\tau_\phi = 10\text{ps}$

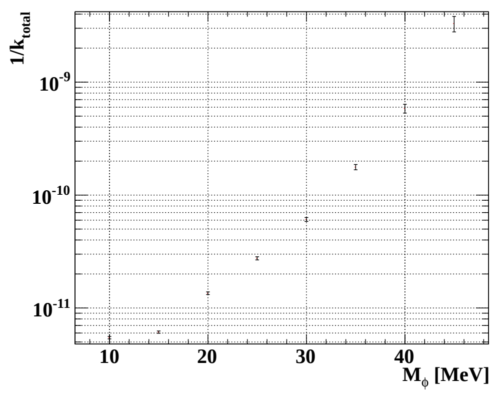

(b) $\tau_\phi = 100\text{ps}$

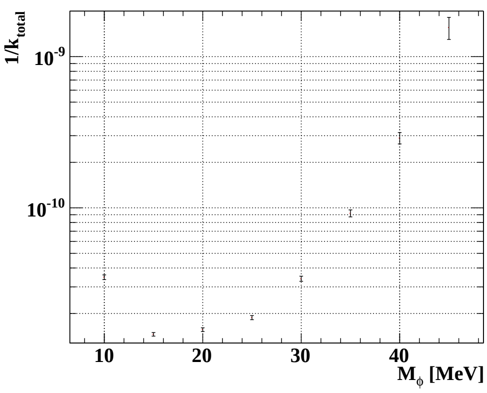

(c) $\tau_\phi = 1\text{ns}$

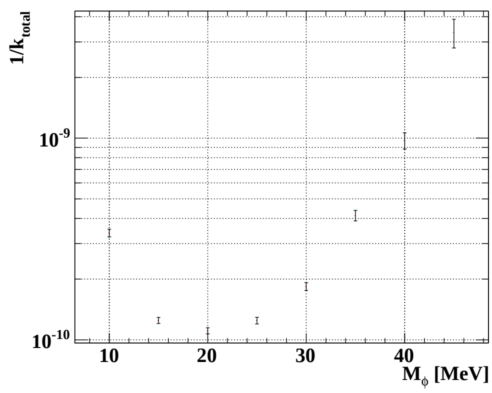

(d) $\tau_\phi = 10\text{ns}$

Figure 5.14: $1/k_{total}$ with statistical error for each lifetime and mass of ϕ.

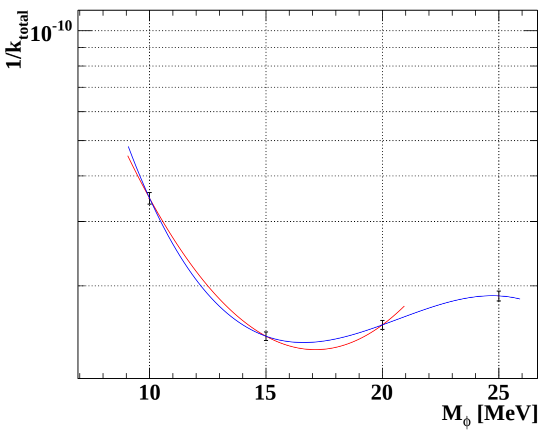

Figure 5.15: An example of interpolation. Red and blue lines are exponential of 2nd and 3rd polynomial function respectively. The region $M_\phi \leq 17$ [MeV] is interpolated with blue line in this case. The difference between blue and red is counted as systematic error.

5.4.12 Single event sensitivity

The result of the estimation of the single event sensitivity ($= 1/k_{total}$) is summarized in the Figure 5.16 and the values are listed in Table A.1–A.4. Systematic errors of the case with $M_\phi = 10, 15, \ldots, 45$ MeV are the sum of the two components described in Section 5.4.10 ; 6.2 % from uncertainty in gamma-ray detector efficiency, and the other from the effect of uncertainty in resolutions and calibrations.

For the interpolated points, bigger value of the sum of statistical and systematic errors of the nearest two points is assigned as systematic error. The sum of this systematic error and the error for interpolation is counted as the total systematic error in the final analysis.

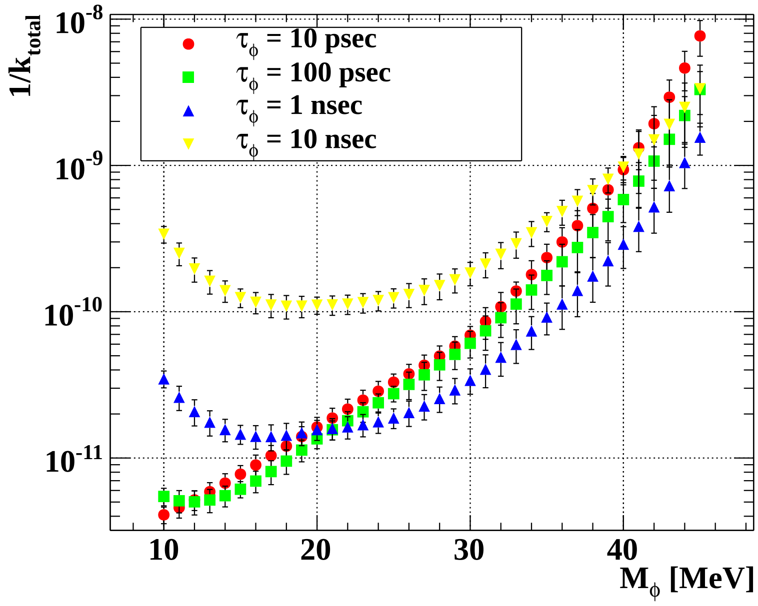

Figure 5.16: $1/k_{total}$ v.s. M_ϕ for each τ_ϕ settings. The error bar shows the sum of systematic error and statistic error.

5.5 Upper bounds on the branching ratio

To extract the 90% confidence level interval (C.I.) of branching ratio, Rolke's method [69] is adopted. Confidence intervals can be extracted finding the points where the $-2log$ likelihood function increases by a factor defined by the required confidence level in $\ln\mathcal{L} + 1/2$ method, which used to be used widely in high energy physics. This method is based on large-sample theory, and it has under-coverage in certain circumstances, but it can be adapted to treat problems with several nuisance parameters which are not known exactly. Rolke's method combine the $\ln\mathcal{L}+1/2$ method with the profile likelihood method in which the multi-dimensional likelihood function is reduced to a function that only depends on the parameter of prime interest. The method is generalized to the problem of a signal with a Poisson distribution, a background with either a Poisson or a Gaussian distribution and an efficiency with either a Binomial or a Gaussian distribution. It is examined to have very good coverage even in cases when the parameters lie close or at the physical boundaries.

In this thesis, we treat expected backgrounds in the signal region and overall efficiency as Gaussian distributions. Background events are classified to three types from the time structure as described in Section 5.3. The number of each types of backgrounds are estimated from three types of time sidebands; category (A), (B), and (C). Then the expected number of backgrounds in the signal region is calculated with equation 5.1 and 5.2. Error of the expected background is estimated adding Poisson errors of the number of observed event in (A), (B) and (C) quadratically normalizing with time width. Although it is exact to treat the expected backgrounds as a sum of three Poisson distribution, we treat it as a Gaussian distribution because of offered option of Rolke's method. We also tried backgrounds with a Poisson distribution with a Poisson error equal to the estimated one, and the difference is estimated to be much smaller than 1%. Therefore the effect of the background distribution shape is expected to be negligible.

The result is shown in the Figure 5.17 and the values are listed in Table B.1. The result of the number of the signal events was consistent with 0, and we only get the upper limit for the branching ratio of $\mu^+ \to e^+\phi, \phi \to \gamma\gamma$ decay. When the lifetime of ϕ is 10 psec, ϕ travels only a few mm, and difference of the efficiency is expected to be very small. Therefore the result of the case $\tau_\phi = 10$ psec is expected to be valid for shorter lifetime, too. However, if the life time is too short and $\Gamma_\phi \ll M_\phi$ does not hold, we can not assume $\mu^+ \to e^+\phi, \phi \to \gamma\gamma$ mode as on-shell process. This result does not hold in this case.

When the mass of ϕ is smaller than ~ 25 MeV and its lifetime is shorter than 1 ns, we get the upper limit of the order of 10^{-11}. Obtained upper limits are better than the expected upper limit from the Crystal Box which is estimated in Section 1.2.2 when $M_\phi <$ 30–40 MeV.

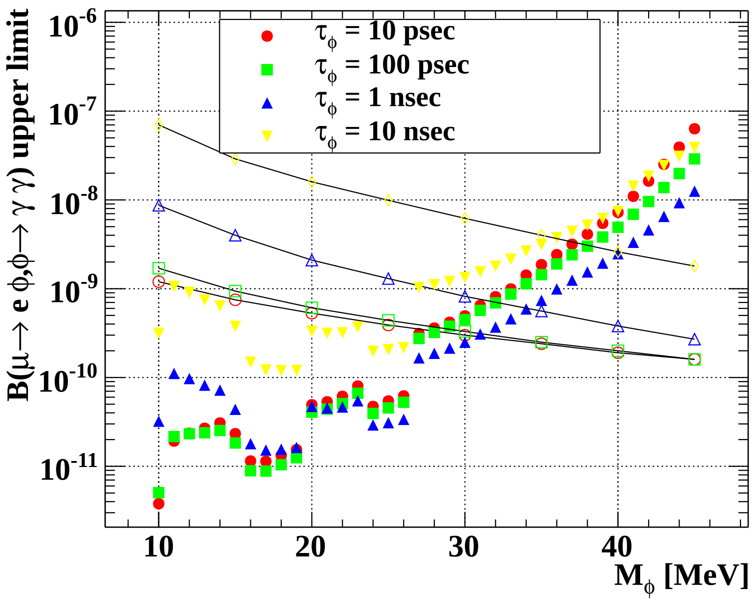

Figure 5.17: Upper Limit of $\mathcal{B}(\mu^+ \to e^+\phi, \phi \to \gamma\gamma\ )$ at grid points of M_ϕ and τ_ϕ (90% C.L.).Solid black line with blank marker is upper limit from Crystal Box experiment estimated in Section 1.2.2. Marker color represent lifetime of ϕ. Red points are expected to be valid for shorter lifetime as long as $\Gamma_\phi \ll M_\phi$ holds.

From the obtained upper bounds, we can obtain constraints for $\lambda_{\mu e}$. Equation 1.6 can be calculated as follows,

$$|\lambda_{\mu e}| \cdot \sqrt{\mathcal{B}(\phi \to \gamma\gamma)} \simeq \sqrt{\mathcal{B}(\mu \to e\phi, \phi \to \gamma\gamma) \cdot 1.7 \times 10^{-7} / \left(1 - \left(\frac{M_\phi}{M_\mu}\right)^2\right)^2}. \tag{5.8}$$

The result is shown in Figure 5.18.

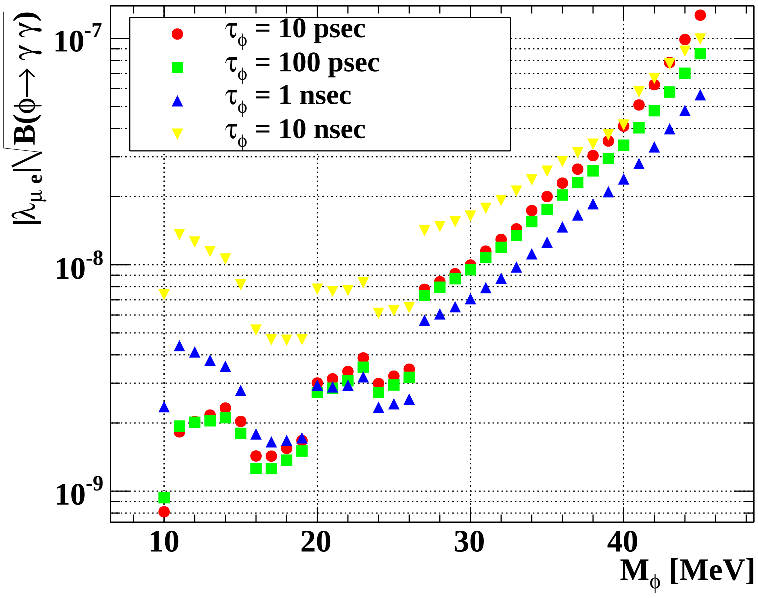

Figure 5.18: Upper Limit of $|\lambda_{\mu e}|\sqrt{\mathcal{B}(\phi \to \gamma\gamma)}$ at grid points of M_ϕ and τ_ϕ (90% C.L.).
.

Chapter 6

Conclusion

A first search for a new light neutral particle ϕ, which causes lepton flavor violating (LFV) muon decay and decays into a pair of photons, $\mu^+ \to e^+\phi, \phi \to \gamma\gamma$, was performed by the MEG experiment. The experiment is designed to search for another LFV decay, $\mu^+ \to e^+\gamma$, and collect gamma-ray and positron signals from muon decays with a novel gamma-ray detector and a positron spectrometer. Although the detectors and trigger settings are not optimized to detect other decay modes, we have good detection efficiency for $\mu^+ \to e^+\phi, \phi \to \gamma\gamma$ mode when the mass of ϕ is small.

We assume ϕ to be a (pesudo)scalar particle with long lifetime and small mass, which decays into gamma-ray pair isotropically in the rest frame of itself. The search was performed using data taken in 2009 and 2010, which corresponds to 1.8×10^{14} muon stop in the target.

The $\mu^+ \to e^+\phi, \phi \to \gamma\gamma$ decay was not detected and we set upper limit on the branching ratio of it for various mass values 10–45 MeV and lifetimes ≤ 10 ns. Obtained upper limits are better than the expected constraints from the bound on generic $\mu^+ \to e^+\gamma\gamma$ set by the Crystal Box experiment [19] when ϕ is lighter than 25–40 MeV. The upper limits are about the order of 10^{-11} when $10 \leq M_\phi \leq 26$ MeV and $\tau_\phi \leq 1$ ns. This established the most stringent limits on cLFV decay mediated by ϕ, which decays into two photons.

The sensitivity is now limited by statistics, so we can expect improvement collecting more data. In 2011 the MEG experiment collected about the same statistics as the sum of 2009 and 2010, and we are planning to collect data until 2013. The sensitivity is expected to improve approximately by a factor of 3 using all the data taken from 2009 to 2013.

Appendix A

Normalization Factor

Values of normalization factor and their errors are listed in Table A.1– A.4.

Table A.1: Normalization factor for $\tau_\phi = 10$ ps

M_ϕ [MeV]	$1/k_{total}$	statistical error	systematic error	error of interpolation
10	4.09×10^{-12}	±2.2%	±10.8%	
11	4.58×10^{-12}		±14.5%	±0.7%
12	5.17×10^{-12}		±14.5%	±0.9%
13	5.88×10^{-12}		±14.5%	±0.8%
14	6.74×10^{-12}		±14.5%	±0.4%
15	7.75×10^{-12}	±2.4%	±12.1%	
16	8.96×10^{-12}		±16.5%	±0.4%
17	1.04×10^{-11}		±16.5%	±0.8%
18	1.21×10^{-11}		±16.5%	±0.8%
19	1.40×10^{-11}		±16.5%	±0.4%
20	1.63×10^{-11}	±2.7%	±13.8%	
21	1.88×10^{-11}		±16.5%	±0.2%
22	2.20×10^{-11}		±16.5%	±0.4%
23	2.49×10^{-11}		±16.5%	±0.4%
24	2.86×10^{-11}		±16.5%	±0.2%
25	3.30×10^{-11}	±3.3%	±10.4%	
26	3.76×10^{-11}		±14.8%	±1.4%
27	4.30×10^{-11}		±14.8%	±2.6%
28	4.97×10^{-11}		±14.8%	±2.5%
29	5.81×10^{-11}		±14.8%	±1.4%
30	6.91×10^{-11}	±4.1%	±10.7%	
31	8.57×10^{-11}		±23.4%	±1.0%
32	1.08×10^{-10}		±23.4%	±1.8%
33	1.38×10^{-10}		±23.4%	±1.8%
34	1.79×10^{-10}		±23.4%	±1.0%
35	2.34×10^{-10}	±5.8%	±17.6%	
36	3.00×10^{-10}		±23.4%	±1.8%
37	3.87×10^{-10}		±23.4%	±3.2%
38	5.09×10^{-10}		±23.4%	±3.1%
39	6.81×10^{-10}		±23.4%	±1.8%
40	9.35×10^{-10}	±9.7%	±11.5%	
41	1.32×10^{-9}		±27.4%	±1.8%
42	1.93×10^{-9}		±27.4%	±3.2%
43	2.93×10^{-9}		±27.4%	±3.7%
44	4.63×10^{-9}		±27.4%	±2.7%
45	7.68×10^{-9}	±20.7%	±6.7%	

Table A.2: Normalization factor for $\tau_\phi = 100$ ps

M_ϕ [MeV]	$1/k_{total}$	statistical error	systematic error	error of interpolation
10	5.46×10^{-12}	±2.5%	±11.2%	
11	5.10×10^{-12}		±13.7%	±3.7%
12	5.02×10^{-12}		±13.7%	±5.0%
13	5.16×10^{-12}		±13.7%	±4.4%
14	5.53×10^{-12}		±13.7%	±2.5%
15	6.12×10^{-12}	±2.3%	±10.4%	
16	6.96×10^{-12}		±14.4%	±2.4%
17	8.08×10^{-12}		±14.4%	±4.2%
18	9.53×10^{-12}		±14.4%	±4.4%
19	1.13×10^{-11}		±14.4%	±2.5%
20	1.35×10^{-11}	±2.7%	±11.7%	
21	1.56×10^{-11}		±14.4%	±0.5%
22	1.80×10^{-11}		±14.4%	±0.9%
23	2.07×10^{-11}		±14.4%	±0.9%
24	2.39×10^{-11}		±14.4%	±0.5%
25	2.75×10^{-11}	±3.3%	±8.9%	
26	3.18×10^{-11}		±20.7%	±0.6%
27	3.70×10^{-11}		±20.7%	±1.1%
28	4.33×10^{-11}		±20.7%	±1.1%
29	5.11×10^{-11}		±20.7%	±0.6%
30	6.09×10^{-11}	±4.0%	±16.7%	
31	7.40×10^{-11}		±25.9%	±0.5%
32	9.10×10^{-11}		±25.9%	±0.8%
33	1.13×10^{-10}		±25.9%	±0.8%
34	1.41×10^{-10}		±25.9%	±0.5%
35	1.77×10^{-10}	±5.4%	±20.5%	
36	2.20×10^{-10}		±30.4%	±1.3%
37	2.75×10^{-10}		±30.4%	±2.3%
38	3.48×10^{-10}		±30.4%	±2.3%
39	4.47×10^{-10}		±30.4%	±1.3%
40	5.84×10^{-10}	±8.9%	±21.5%	
41	7.81×10^{-10}		±32.6%	±1.3%
42	1.07×10^{-9}		±32.6%	±2.3%
43	1.51×10^{-9}		±32.6%	±2.7%
44	2.19×10^{-9}		±32.6%	±2.0%
45	3.30×10^{-9}	±15.7%	±16.9%	

Table A.3: Normalization factor for $\tau_\phi = 1$ ns

M_ϕ [MeV]	$1/k_{total}$	statistical error	systematic error	error of interpolation
10	3.48×10^{-11}	±3.6%	±9.6%	
11	2.60×10^{-11}		±14.8%	±4.1%
12	2.08×10^{-11}		±14.8%	±5.5%
13	1.76×10^{-11}		±14.8%	±4.8%
14	1.56×10^{-11}		±14.8%	±2.7%
15	1.46×10^{-11}	±2.8%	±12.0%	
16	1.41×10^{-11}		±15.7%	±2.6%
17	1.40×10^{-11}		±15.7%	±4.5%
18	1.43×10^{-11}		±15.7%	±4.8%
19	1.49×10^{-11}		±15.7%	±2.7%
20	1.56×10^{-11}	±2.8%	±12.9%	
21	1.59×10^{-11}		±15.7%	±1.0%
22	1.63×10^{-11}		±15.7%	±1.7%
23	1.69×10^{-11}		±15.7%	±1.7%
24	1.77×10^{-11}		±15.7%	±1.0%
25	1.88×10^{-11}	±3.1%	±12.3%	
26	2.05×10^{-11}		±19.7%	±0.02%
27	2.27×10^{-11}		±19.7%	±0.04%
28	2.55×10^{-11}		±19.7%	±0.04%
29	2.92×10^{-11}		±19.7%	±0.02%
30	3.40×10^{-11}	±3.9%	±15.8%	
31	4.05×10^{-11}		±24.5%	±0.8%
32	4.89×10^{-11}		±24.5%	±1.4%
33	5.98×10^{-11}		±24.5%	±1.4%
34	7.39×10^{-11}		±24.5%	±0.8%
35	9.20×10^{-11}	±5.3%	±19.2%	
36	1.13×10^{-10}		±31.7%	±1.2%
37	1.40×10^{-10}		±31.7%	±2.2%
38	1.75×10^{-10}		±31.7%	±2.1%
39	2.23×10^{-10}		±31.7%	±1.2%
40	2.90×10^{-10}	±8.6%	±23.1%	
41	3.84×10^{-10}		±31.7%	±1.2%
42	5.21×10^{-10}		±31.7%	±2.2%
43	7.27×10^{-10}		±31.7%	±2.5%
44	1.05×10^{-9}		±31.7%	±1.9%
45	1.56×10^{-9}	±16.6%	±8.0%	

Table A.4: Normalization factor for $\tau_\phi = 10$ ns

M_ϕ [MeV]	$1/k_{total}$	statistical error	systematic error	error of interpolation
10	3.39×10^{-10}	$\pm 4.4\%$	$\pm 8.6\%$	
11	2.51×10^{-10}		$\pm 14.6\%$	$\pm 3.1\%$
12	1.96×10^{-10}		$\pm 14.6\%$	$\pm 4.2\%$
13	1.62×10^{-10}		$\pm 14.6\%$	$\pm 3.7\%$
14	1.39×10^{-10}		$\pm 14.6\%$	$\pm 2.1\%$
15	1.25×10^{-10}	$\pm 3.5\%$	$\pm 11.1\%$	
16	1.16×10^{-10}		$\pm 14.6\%$	$\pm 2.0\%$
17	1.11×10^{-10}		$\pm 14.6\%$	$\pm 3.5\%$
18	1.09×10^{-10}		$\pm 14.6\%$	$\pm 3.7\%$
19	1.09×10^{-10}		$\pm 14.6\%$	$\pm 2.1\%$
20	1.11×10^{-10}	$\pm 3.5\%$	$\pm 9.9\%$	
21	1.11×10^{-10}		$\pm 15.0\%$	$\pm 0.1\%$
22	1.13×10^{-10}		$\pm 15.0\%$	$\pm 0.2\%$
23	1.15×10^{-10}		$\pm 15.0\%$	$\pm 0.2\%$
24	1.19×10^{-10}		$\pm 15.0\%$	$\pm 0.1\%$
25	1.25×10^{-10}	$\pm 3.8\%$	$\pm 11.2\%$	
26	1.31×10^{-10}		$\pm 18.2\%$	$\pm 0.5\%$
27	1.40×10^{-10}		$\pm 18.2\%$	$\pm 0.8\%$
28	1.51×10^{-10}		$\pm 18.2\%$	$\pm 0.8\%$
29	1.65×10^{-10}		$\pm 18.2\%$	$\pm 0.5\%$
30	1.84×10^{-10}	$\pm 4.4\%$	$\pm 13.8\%$	
31	2.12×10^{-10}		$\pm 18.2\%$	$\pm 1.2\%$
32	2.47×10^{-10}		$\pm 18.2\%$	$\pm 2.1\%$
33	2.91×10^{-10}		$\pm 18.2\%$	$\pm 2.1\%$
34	3.46×10^{-10}		$\pm 18.2\%$	$\pm 1.2\%$
35	4.14×10^{-10}	$\pm 6.0\%$	$\pm 8.8\%$	
36	4.84×10^{-10}		$\pm 18.3\%$	$\pm 1.1\%$
37	5.69×10^{-10}		$\pm 18.3\%$	$\pm 1.9\%$
38	6.73×10^{-10}		$\pm 18.3\%$	$\pm 1.9\%$
39	8.04×10^{-10}		$\pm 18.3\%$	$\pm 1.1\%$
40	9.73×10^{-10}	$\pm 9.2\%$	$\pm 9.1\%$	
41	1.20×10^{-9}		$\pm 45.1\%$	$\pm 1.1\%$
42	1.49×10^{-9}		$\pm 45.1\%$	$\pm 1.9\%$
43	1.91×10^{-9}		$\pm 45.1\%$	$\pm 2.2\%$
44	2.49×10^{-9}		$\pm 45.1\%$	$\pm 1.6\%$
45	3.34×10^{-9}	$\pm 16.2\%$	$\pm 28.9\%$	

Appendix B

Upper limits for each set of mass and lifetime values

Values of upper limit are listed in Table B.1.

Table B.1: Estimated upper limit for each M_ϕ and τ_ϕ

M_ϕ [MeV]	$\tau_\phi = 10$ps	100ps	1ns	10 ns
10	3.8×10^{-12}	5.1×10^{-12}	3.2×10^{-11}	3.1×10^{-10}
11	1.9×10^{-11}	2.2×10^{-11}	1.1×10^{-10}	1.1×10^{-09}
12	2.4×10^{-11}	2.3×10^{-11}	9.7×10^{-11}	9.1×10^{-10}
13	2.7×10^{-11}	2.4×10^{-11}	8.2×10^{-11}	7.5×10^{-10}
14	3.1×10^{-11}	2.5×10^{-11}	7.2×10^{-11}	6.4×10^{-10}
15	2.3×10^{-11}	1.8×10^{-11}	4.4×10^{-11}	3.8×10^{-10}
16	1.1×10^{-11}	8.9×10^{-12}	1.8×10^{-11}	1.5×10^{-10}
17	1.1×10^{-11}	8.8×10^{-12}	1.5×10^{-11}	1.2×10^{-10}
18	1.3×10^{-11}	1.0×10^{-11}	1.6×10^{-11}	1.2×10^{-10}
19	1.5×10^{-11}	1.2×10^{-11}	1.6×10^{-11}	1.2×10^{-10}
20	4.9×10^{-11}	4.1×10^{-11}	4.7×10^{-11}	3.3×10^{-10}
21	5.3×10^{-11}	4.4×10^{-11}	4.5×10^{-11}	3.1×10^{-10}
22	6.1×10^{-11}	5.1×10^{-11}	4.7×10^{-11}	3.2×10^{-10}
23	8.0×10^{-11}	6.6×10^{-11}	5.5×10^{-11}	3.7×10^{-10}
24	4.7×10^{-11}	3.9×10^{-11}	2.9×10^{-11}	2.0×10^{-10}
25	5.4×10^{-11}	4.5×10^{-11}	3.1×10^{-11}	2.1×10^{-10}
26	6.2×10^{-11}	5.3×10^{-11}	3.4×10^{-11}	2.2×10^{-10}
27	3.1×10^{-10}	2.8×10^{-10}	1.7×10^{-10}	1.0×10^{-9}
28	3.6×10^{-10}	3.2×10^{-10}	1.9×10^{-10}	1.1×10^{-9}
29	4.2×10^{-10}	3.8×10^{-10}	2.1×10^{-10}	1.2×10^{-9}
30	4.9×10^{-10}	4.5×10^{-10}	2.5×10^{-10}	1.3×10^{-9}
31	6.5×10^{-10}	5.7×10^{-10}	3.1×10^{-10}	1.6×10^{-9}
32	8.1×10^{-10}	6.9×10^{-10}	3.7×10^{-10}	1.8×10^{-9}
33	9.9×10^{-10}	8.7×10^{-10}	4.6×10^{-10}	2.1×10^{-9}
34	1.4×10^{-9}	1.1×10^{-9}	5.9×10^{-10}	2.7×10^{-9}
35	1.9×10^{-9}	1.4×10^{-9}	7.4×10^{-10}	3.1×10^{-9}
36	2.4×10^{-9}	1.9×10^{-9}	9.9×10^{-10}	3.8×10^{-9}
37	3.2×10^{-9}	2.4×10^{-9}	1.2×10^{-9}	4.4×10^{-9}
38	4.1×10^{-9}	3.0×10^{-9}	1.5×10^{-9}	5.2×10^{-9}
39	5.4×10^{-9}	3.8×10^{-9}	1.9×10^{-9}	6.2×10^{-9}
40	7.3×10^{-9}	4.9×10^{-9}	2.5×10^{-9}	7.4×10^{-9}
41	1.1×10^{-8}	6.9×10^{-9}	3.3×10^{-9}	1.4×10^{-8}
42	1.6×10^{-8}	9.6×10^{-9}	4.6×10^{-9}	1.9×10^{-8}
43	2.5×10^{-8}	1.4×10^{-8}	6.5×10^{-9}	2.4×10^{-8}
44	3.9×10^{-8}	2.0×10^{-8}	9.3×10^{-9}	3.1×10^{-8}
45	6.3×10^{-8}	2.9×10^{-8}	1.3×10^{-8}	3.9×10^{-8}

Acknowledgment

The MEG experiment is a project performed by a collaboration of University of Tokyo, KEK, Waseda University, Paul Scherrer Institut, INFN and Pisa, University of Genova, University of Pavia, University Rome Sapienza, University of Lecce, BINP Novosibirsk, JINR Dubna and University of California Irvine. Research and development works took over a decade, and we started taking physics data from 2008. This work could be finished with many helps and efforts by the MEG collaborators.

I am deeply grateful to my supervisor, Prof. Toshinori Mori who provided carefully considered feedback and valuable comments. He is one of the spokespersons of the MEG collaboration and gave me chances to work for the MEG experiment.

I am thankful to Prof. Satoshi Mihara, who accepted me as co-operative researcher of KEK after I left the University of Tokyo. His daily guide was hard, but indispensable to finish this work.

During my research in PSI, I get ill and supports from Japanese collaborators was very grateful. Especially I can not thank enough for Prof. Wataru Ootani's help when I stayed in a hospital in Baden, Switzerland. I want to thank his suggestion to study about generic $\mu^+ \to e^+\gamma\gamma$ decay, which was starting of this work.

I would like to express my gratitude to Prof. Toshiyuki Iwamoto, Dr. Ryu Sawada and Dr. Yusuke Uchiyama, who worked together in the same office room. Their opinions and information have helped me very much throughout the production of this study.

I would also like to thank Dr. Hajime Nishiguchi, Mr. Yuki Fujii, Dr. Elisabetta Baracchini, Dr. Cecilia Voena and Dr. Francesco Renga for giving me informations about analysis of the positron spectrometer. I appreciate Dr. Marco Grassi, Dr. Donato Nicolò and Dr. Luca Galli for useful informations about trigger system. I would like to express my appreciation to Dr. Stefan Ritt, Dr. Peter R. Kettle, Dr. Malte Hildebrandt for supporting me in PSI. I appreciate Dr. Yasuhiro Nishimura, Dr. Shuei Yamada, Dr. Yasuko Hisamatsu, Dr. Kenji Ozone, Prof. Akihiro Maki, Prof. Tom Haruyama, Mr. Katsuyu Kasami, Ms. Bai Xue, Mr. Daisuke Kaneko and Ms. Miki Nishimura for giving me valuable advices and pleasant research time. I thank Dr. Giovanni Signorelli, Dr. Angela Papa, Mr. Emanuele Ripiccini, Dr. Paolo W. Cattaneo for meaningful discussions.

I would also like to express my gratitude to my family for their support and warm encouragements.

Bibliography

[1] Adriana Cordero-Did, G. Tavares-Velasco, and J.J. Toscano "Implication of a very light pseudoscalar boson on lepton flavor violation", Phys. Rev. **D72**, 117701 (2005).

[2] David L. Anderson, Christopher D. Carone, and Marc Sher "Probing the light pseudoscalar window", Phys. Rev. D **67**, 115013 (2003).

[3] Steven Weinberg "Approximate Symmetries and Pseudo-Goldstone Bosons", Phys. Rev. Lett. **29**, 1698 (1972).

[4] S. Weinberg, Phys. Rev. Lett. **40**, 223 (1978); F. Wilczek, Phys. Rev. Lett. **40**, 279 (1987).

[5] F. Wilczek, Phys. Rev. Lett. **49**, 1549 (1982).

[6] Y. Chikashige, R.N. Mohapatra, and R.D. Peccei, Phys. Lett. **B98**, 265 (1981); G.B. Gelmini and M. Roncadelli, Phys. Lett. **B99**, 411 (1981).

[7] R.D. Peccei and H.R. Quinn, Phys. Rev. Lett. **38**, 1440 (1977); Phys. Rev. **D 16**, 1791 (1977).

[8] D.L. Anderson, C.D. Carone, and M. Sher, Phys. Rev. **D67**, 115013 (2003).

[9] F. Larios, G. Tavares-Velasco, and C.P. Yuan, Phys. Rev. **D64**, 05004 (2001); **66**, 075006 (2002).

[10] B. Dobrescu, G. Landsberg, and K. Matchev, "Higgs Boson Decays to CP-odd Scalar at the Tevatron and Beyond", Phys. Rev. D 63, 075003 (2001).

[11] Sarah Andreas, Oleg Lebedev, Saul Ramos-Sanchez, Andreas Ringwald, "Constraints on a very light CP-odd Higgs of the NMSSM and other axion-like particles", JHEP 1008:003,2010

[12] T. P. Cheng and M. Sher, "Mass-matrix ansatz and flavor nonconservation in models with multiple Higgs doublets" Phys. Rev. D **35**, 3484 (1987).

[13] L. Resnick, M. K. Sundaresan, and P. J. S. Watson, "Is There a Light Scalar Boson?" Phys. Rev. D **8**, 172 (1973).

[14] R. R. Crittenden, W. D. Walker, J. Ballam, "Radiative decay modes of the muon", Phys. Rev. **121**, 1823–1832 (1961).

[15] W. H. Bertl *et al.* [SINDRUM Collaboration], "Search for the decay $\mu^+ \to e^+e^+e^-$ ", Nucl. Phys. **B260**, 1 (1985).

[16] S. J. Freedman, B. K. Fujikawa, J. Napolitano, J. E. Nelson, R. D. McKeown, K. T. Lesko, J. B. Donahue, G. T. Garvey *et al.*, "Limits on neutrino oscillations from anti-electron-neutrino appearance," Phys. Rev. **D47**, 811–829 (1993)

[17] J. Adam *et al.* (MEG Collaboration) "New Limit on the Lepton-Flavor-Violating Decay $\mu^+ \to e^+\gamma$ ", Phys. Rev. Lett. **107**, 171801 (2011)

[18] U. Bellgardt *et al.* [SINDRUM Collaboration], "Search for the decay $\mu^+ \to e^+e^+e^-$ ", Nucl. Phys. **B299**, 1 (1988).

[19] R. D. Bolton *et al.*, "Search for Rare Muon Decays with the Crystal Box Detector", Phys. Rev. **D38**, 2077–2101 (1988). D. Grosnick and S.C.Wright *et al*, "Search for the Rare Decay $\mu^+ \to e^+\gamma\gamma$ ", Phys. Rev. Lett. **57**, 3241 (1986).

[20] D. A. Bryman, E. T. H. Clifford, "EXOTIC MUON DECAY $\mu \to e + x$", Phys. Rev. Lett. **57**, 2787 (1986).

[21] A. Jodidio *et al.*, "Search for right-handed currents in muon decay," Phys. Rev. **D34**, 1967 (1986).

[22] R. Eichler *et al.* [SINDRUM Collaboration], "Limits for short-lived neutral particles emitted in μ^+ or π^+ decay", Phys. Lett. **B175**, 101 (1986).

[23] W. Wagner *et al.*, "PSI status 2008 - Developments at the 590 MeV proton accelerator facility", Nucl. Instr. Meth. A **600**, 5–7 (2009).

[24] The 590 MeV Ring Cyclotron of PSI, http://abe.web.psi.ch/accelerators/ringcyc.php.

[25] A. E. Pifer, T. Bowen, and K. R. Kendall, "A high stopping density μ^+ beam", Nucl. Instr. Meth. **135**, 39–46 (1976); H. W. Reist *et al.*, "Development of a low-momentum "surface" muon beam for LAMPF", Nucl. Instr. Meth. **153**, 61–64 (1978).

[26] W. Ootani *et al.*, "Development of a Thin-wall Superconducting Magnet for the Positron Spectrometer in the MEG Experiment", IEEE Trans. Appl. Superconduct. **14**, 568–571 (2005).

[27] A. Yamamoto *et al.*, "Development towards Ultra-thin Superconducting Solenoid Magnets for High Energy Particle Detectors", Nucl. Phys. B (Proc. Suppl.) **78**, 565–570 (1999); A. Yamamoto *et al.*, "A Thin Superconducting Solenoid Magnet for Particle Astrophysics", IEEE Trans. Appl. Superconduct. **12**, 438–442 (2002).

[28] H. Nishiguchi, "An Innovative Positron Spectrometer to Search for the Lepton Flavour Violating Muon Decay with a Sensitivity of 10^{-13}", Ph.D. Thesis, the University of Tokyo (2008), http://meg.web.psi.ch/docs/theses/nishiguchi_phd.pdf/.

[29] Saint-Gobain Ceramics & Plastics, http://www.detectors.saint-gobain.com/.

[30] Hamamatsu Photonics, http://www.hamamatsu.com/.

[31] S. Dussoni, "Search for Lepton Flavour Violation: The MEG experiment", Ph.D. Thesis, Università degli Studi di Genova (2006).

[32] R. Valle, "Development of the Timing Counter", Ph.D. Thesis, Università degli Studi di Genova (2006), http://meg.web.psi.ch/docs/theses/valle_phd.pdf/.

[33] K. Nakamura *et al.* (Particle Data Group), "Review of Particle Physics", J. Phys. G **37**, 075021 (2010). http://pdg.lbl.gov/.

[34] D. Lide ed., "CRC Handbook of Chemistry & Physics 2004–2005", Crc Pr. I Llc. (2004).

[35] A. C. H. Hallett, "ARGON, HELIUM AND THE RARE GASES", Vol **I**, Chap IX, Interscience Publishers, Inc., New York - London (1961).

[36] C. W. Fabjan and F. Gianotti, "Calorimetry for particle physics", Rev. Mod. Phys. **75**, 1243–1286 (2003).

[37] J. Jortner, L. Mever, S. A. Rice, and E. G. Wilson, "Localized Excitations in Condensed Ne, Ar, Kr, and Xe", J. Chem. Phys. **42**, 4250–4253; N. Schwenter, E.-E. Koch, and J. Jortner, "Electronic Excitations in Condensed Rare Gases", Springer-Verlag, Berlin (1985).

[38] L. M. Barkov, A. A. Grebenuk, N. M. Ryskulov, P. Yu. Stepanov, and S. G. Zverev, "Measurement of the refractive index of liquid xenon for intrinsic scintillation light", Nucl. Instr. Meth. A, **379**, 482–483 (1996).

[39] V. N. Solovov *et al.*, "Measurement of the refractive index and attenuation length of liquid xenon for its scintillation light", Nucl. Instr. Meth. A, **516**, 462–474 (2004).

[40] G. M. Seidel, R. E. Lanou, and W. Yao, "Rayleigh scattering in rare-gas liquids", Nucl. Instr. Meth. A, **489**, 189–194 (2002).

[41] T. Doke *et al.*, "Absolute Scintillation Yields in Liquid Argon and Xenon for Various Particles", Jpn. J. Appl. Phys. **41**, 1538–1545 (2002).

[42] A. Hitachi *et al.*, "Effect of ionization density on the time dependence of luminescence from liquid argon and xenon", Phys. Rev. B **27**, 5279–5285 (1983).

[43] A. Braem *et al.*, "Observation of the UV scintillation light from high energy electron showers in liquid xenon", Nucl. Instr. Meth. A, **320**, 228–237 (1992).

[44] V. Y. Chapel, M. I. Lopes, R. Ferreira Marques, and A. J. P. L. Policarpo, "Purification of liquid xenon and impurity monitoring for a PET detector", Nucl. Instr. Meth. A, **349**, 500–505 (1994).

[45] S. Mihara *et al.*, "Development of a liquid-xenon photon detector – towards the search for a muon rare decay mode at Paul Scherrer Institut", Cryogenics **44**, 223–228 (2004).

[46] K. Ozone, "Liquid Xenon Scintillation Detector for the New $\mu \to e\gamma$ Search Experiment", Ph.D. Thesis, the University of Tokyo (2005), http://meg.web.psi.ch/docs/theses/ozoned.pdf/.

[47] R. Sawada, "A Liquid Xenon Scintillation Detector to Search for the Lepton Flavour Violating Muon Decay with a Sensitivity of 10^{-13}", Ph.D. Thesis, the University of Tokyo (2008), http://meg.web.psi.ch/docs/theses/sawada_phd.pdf/.

[48] S. Kubota, M. Hishida, and J. Raun, "Evidence for a triplet state of the self-trapped exciton states in liquid argon, krypton and xenon", J. Phys. C **11**, 2645–2651 (1978); S. Kubota *et al.*, "Dynamical behavior of free electrons in the recombination process in liquid argon, krypton, and xenon", Phys. Rev. B **20**, 3486–3496 (1979).

[49] T. Doke, "Fundamental properties of liquid argon, krypton and xenon as radiation media", Port. Phys. **12**, 9–48 (1981)

[50] Photon Cross Sections Data Base, http://physics.nist.gov/PhysRefData/.

[51] T. Haruyama *et al.*, "Development of a high-power coaxial pulse tube refrigerator for a liquid xenon calorimeter", Advances in Cryogenic Engineering **49**, 1459–1466 (2004).

[52] T. Iwamoto *et al.*, "Development of a large volume zero boil-off liquid xenon storage system for muon rare decay experiment (MEG)", Cryogenics **49**, 254–258 (2009).

[53] Y. Yoshino *et al.*, "Absorption cross section measurement of water vapor in the wavelength region 120 to 188nm", Chem. Phys. **211** 387–391 (1996).

[54] S. Himi *et al.*, "Liquid and Solid Argon, and Nitrogen-doped liquid and solid Argon Scintillators", Nucl. Inst. Meth. **203**, 253 (1982).

[55] S. Mihara *et al.*, "Development of a liquid-xenon photon detector - towards the search for a muon rare decay mode at Paul Scherrer Institut", Cryogenics **44**, 223–228 (2004).

[56] S. Mihara *et al.*, "Development of a method for liquid xenon purification using a cryogenic centrifugal pump", Cryogenics **46**, 688–693 (2006).

[57] Samios, N. P., "Panofsky Ratio", Phys. Rev. Lett. **4**, 470–472 (1960).

[58] J. Spuller *et al.* "A remeasurement of the Panofsky ratio", Phys. Lett. B **67**, 479–482 (1977).

[59] S. Ritt, "The DRS chip: cheap waveform digitizing in the GHz range", Nucl. Instr. Meth. A, **518**, 470–471 (2004); S. Ritt, "Design and Performance of the 5 GHz Waveform Digitizing Chip DRS3", Nucl. Sci. Symp. Conf. Rec. IEEE **4**, 2485–2488 (2007); S. Ritt *et al.*, "Application of the DRS chip for fast waveform digitizing", Nucl. Instr. Meth. A **623**, 486–488 (2010).

[60] L. Galli, "A real time glance at the Lepton Flavor Decay muon to positron and gamma in the MEG experiment", Ph.D. Thesis, University of Pisa (2010). http://meg.web.psi.ch/docs/theses/GalliThesis.pdf/.

[61] GEANT, Detector Description and Simulation Tool version 3.21, http://wwwasd.web.cern.ch/wwwasd/geant/.

[62] Garfield, Simulation of gaseous detectors, http://garfield.web.cern.ch/garfield/.

[63] ROME, Root based Object oriented Midas Extension, https://midas.psi.ch/rome/.

[64] ROOT, An Object-Oriented Data Analysis Framework, http://root.cern.ch/.

[65] R. E. Kalman, "A New Approach to Linear Filtering and Prediction Problems", Transactions of the ASME – Journal of Basic Engineering, **D82**, 35–45 (1960).

[66] M.Morháč *et al.*, "Identification of peaks in multidimensional coincidence γ-ray spectra" Nucl. Instr. Meth. A, **443**, 108–125 (2000).

[67] Y. Uchiyama, "Analysis of the First MEG Physics Data to Search for the Decay $\mu^+ \to e^+\gamma$ ", Ph.D. Thesis, the University of Tokyo (2009), http://meg.web.psi.ch/docs/theses/uchiyama_phd.pdf

[68] Feldman, Gary J. and Cousins, Robert D. "Unified approach to the classical statistical analysis of small signals", Phys. Rev. D **57**, 3873–3889 (1998)

[69] W.Rolke, A. Lopez, J. Conrad and Fred James "Limits and Confidence Intervals in presence of nuisance parameters" Nucl. Instrum. Meth. **A551**, 493-503 (2005)